Analysis and Solutions of Power Harmonics in Medium Voltage Distribution Networks

School of Engineering

A thesis submitted for the degree of

Doctor of Philosophy

Thamer A. H. Alghamdi

September 2022

Contents

Abstract

The transition toward more sustainable energy systems is driven mainly by greenhouse gas emissions reduction schemes and the growing demand for energy worldwide. Consequently, more Distributed Energy Resources (DER) based power sources and their enabling technologies such as Medium Voltage Direct Current (MVDC) systems are being integrated into the existing distribution networks to help meet such challenges. However, due to the presence of the Power Electronics (PE) based power converters interfacing these systems with the main power network, concerns related to power harmonics in today's distribution networks must be addressed. To investigate the severity of power harmonics in the distribution networks with the presence of the MVDC converters, a detailed model of an MVDC converter including the switching behaviour of the semiconductor devices with a suitable control system and an interleaved Pulse-width Modulation (PWM) scheme was developed in this study. The key finding is that the proposed harmonic mitigation technique, the interleaved SPWM technique, has significantly reduced the Total Harmonic Distortion (THD) to 2% at the rated system capacity with no significant even-order harmonic components. The real data obtained from the power network of Albaha was also modelled and simulated in the frequency domain using the established harmonic models of the power system components to conduct the harmonic propagations study of the MVDC converter into the AC network. The MVDC converter harmonic performance in the Albaha power system revealed that the THDs at different voltage levels comply with the standard limits.

Moreover, applications of Artificial Intelligence (AI), especially the optimization algorithms for power harmonic solutions have received considerable attention over recent years. Thus, in this research, the recently developed Manta Ray Foraging Optimization (MRFO) algorithm has been implemented for the optimal parameters design of a high-pass Passive Power Filter (PPF). An analytical harmonic analysis approach based on the Monte Carlo Simulation (MCS) was also proposed for PPF harmonic performance evaluation including uncertainties at the power network level. For the superiority validation of the MRFO algorithm, different optimizers that have quite similar hunting and modelling strategies have been adopted. The

MRFO algorithm has shown better solution-finding capability but relatively higher computational effort. By including uncertainties at the power network level, the harmonic performance of the optimally designed PPF proposed by the MRFO algorithm was investigated using a proposed MCS-based method, which has shown the significance of the PPF in terms of voltage distortions, system performance parameters, and the network's hosting capacity for more renewable systems. The results imply that the optimally designed PPF can effectively attenuate the high-order harmonics and improved the system performance parameters over different operating conditions to continually comply with the standard limits. The proposed MCS method showed that the optimally designed PPF reduced the voltage and current distortions by roughly 54% and 30%, respectively, and improved the network hosting capacity by 10% for the worst-case scenario.

Furthermore, DER-based power sources are predicted to cause significant harmonic distortions in today's power networks due to the utilisation of power conversion systems, which are widely recognized as harmonic sources. Identifying the actual contribution of an offending harmonic source can be a challenging task, especially with multiple harmonic sources connected, changes in the system's characteristic impedance, and the intermittent nature of renewable resources. Hence, a method based on an Artificial Neural Network (ANN) system including the location-specific data was proposed in this thesis to estimate the actual harmonic distortions of a harmonic source. The proposed method would help model the admittance of the harmonic source under the estimation, capture its harmonic performance over different operating conditions, and provide accurate harmonic distortions estimations. For this purpose, a simple power system was modelled and simulated, and the harmonic performance of a solar Photovoltaics (PV) system was used to train the ANN system and improve its prediction performance. Additionally, the expert ANN-based harmonic distortion estimator was validated in the IEEE 34-bus test feeder with different established harmonic sources, and it has estimated the individual harmonic components with a maximum error of less than 10% and a maximum median of 5.4%.

Declaration

This work has not previously been accepted in substance for any degree and is not concurrently submitted in candidature for any degree.

Signed.....Thamer A. H. Alghamdi..... Date.....September 2022....

This thesis is being submitted for the degree of PhD.

Signed.....Thamer A. H. Alghamdi..... Date.....September 2022....

This thesis is the result of my own independent work/investigation, except where otherwise stated. Other sources are acknowledged by explicit references.

Signed.....Thamer A. H. Alghamdi..... Date.....September 2022....

I hereby give consent for my thesis, if accepted, to be available for photocopying and for inter- library loan, and for the title and summary to be made available to outside organisations.

Signed.....Thamer A. H. Alghamdi..... Date.....September 2022....

The word account is 40,000.

Acknowledgement

ٱلْحَمْدُ لِلَّهِ رَبِّ ٱلْعَٰلَمِينَ

I would like to express my heartfelt gratitude to my supervisors, Dr Fatih Anayi and Dr Michael Packianather, for the guidance, support, and informative meetings throughout my PhD research work.

Thanks also go to the Saudi government and Albaha University for sponsoring my PhD without which this journey would have never begun. I would also thank Dr Gamal Hazza for his support during my trips to collect the data on the Albaha power network.

Thanks to my colleagues in the research centre, the IT team, and the research office at Cardiff University for the support and assistance along my PhD journey, especially during the COVID-19 pandemic. Thanks to the School of Engineering, Cardiff University, for funding the Open Access publications out of this research work.

Finally, I am grateful to my loving family for their endless patience, support, and encouragement all the while.

Publications List

Journal Papers:

1. **T. A. H. Alghamdi**, F. J. Anayi, and M. Packianather, "Modelling and Control Development of a Cascaded NPC-based MVDC Converter for Harmonic Analysis Studies in Power Distribution Networks," *Energies*, vol. 15, no. 13, p. 4867, 2022.

2. **T. A. H. Alghamdi**, F. Anayi and M. Packianather, "Optimal Design of Passive Power Filters using the MRFO Algorithm and a Practical Harmonic Analysis Approach including Uncertainties in Distribution Networks," *Energies*, vol. 15, no. 7, p. 2566, 2022.

3. **T. A. H. Alghamdi**, O. T. E. Abdusalam, F. J. Anayi, and M. Packianather, "An Artificial Neural Network based Harmonic Distortions Estimator for Grid-Connected Power Converter-based Applications," *Ain Shams Engineering Journal, 2022*.

Papers Presented in Conferences:

1. **T. A. H. Alghamdi** and F. J. Anayi, "Modelling and Control Development of an MVDC Converter Implemented for Albaha Power Network," *5th International Conference on Power and Energy Engineering (ICPEE)*, pp. 66-72, Dec. 2021.

2. **T. A. H. Alghamdi** and F. J. Anayi, "Analysis of Harmonic Propagations in Albaha Power Network due to the Implementation of an MVDC Converter," *IEEE PES Innovative Smart Grid Technologies - Asia (ISGT Asia)*, pp. 1-5, Dec. 2021.

List of Figures

List of Tables

Abbreviations

AC	Alternating Current
ACO	Ant Colony Optimization
AI	Artificial Intelligence
ANN	Artificial Neural Networks
BGH	Background Harmonics
CHB	Cascaded H-Bridge
CIHD	Current Individual Harmonic Distortion
CSA	Chameleon Swarm Algorithm
DC	Direct Current
DER	Distributed Energy Resources
DG	Distributed Generation
DHPF	Decoupled Harmonic Power Flow
dq	Direct-Quadrature
EMC	Electromagnetic Compatibility
ESN	Echo State Network
EV	Electric Vehicles
FCC	Flying Capacitor Clamped
FFT	Fast Fourier Transform
GA	Genetic Algorithm
GEO	Golden Eagle Optimizer
HC	Hosting Capacity
HVDC	High Voltage Direct Current
IEEE	Institute of Electrical and Electronics Engineers
IPSA	Interactive Power System Analysis
LHZ	Left-Hand Zero
MCS	Monte Carlo Simulation
MLP	Multi-Layer Perceptron
MRFO	Manta Rays Foraging Optimization
MSE	Mean Squared Error
MVDC	Medium Voltage Direct Current

NARX	Nonlinear Auto-Regressive eXogenous
NPC	Neutral Point Clamped
p.u.	per unit
PCC	Point of Common Coupling
PF	Power Factor
PE	Power Electronics
PFC	Power Factor Correction
pf	penalty factor
PI	Proportional Integral
PLL	Phase-Locked Loop
PoC	Point of Connection
PPF	Passive Power Filter
PSO	Particle Swarm Optimization
PV	Photovoltaics
PWM	Pulse-width Modulation
RES	Renewable Energy Sources
RFO	Red Fox Optimizer
RMS	Root Mean Square
RNN	Recurrent Neural Network
SA	Simulated Annealing
SCL	Short Circuit Level
SERA	Saudi Electricity Regulatory Authority
SFC	Static Frequency Converter
SPWM	Sinusoidal Pulse-Width Modulation
STATCOM	Static Synchronous Compensator
TCR	Thyristor Controlled Reactors
TDD	Total Demand Distortion
THD	Total Harmonic Distortion
VIHD	Voltage Individual Harmonic Distortion
VSC	Voltage Source Converter
VTHD	Voltage THD
WT	Wind Turbines

Chapter 1. Introduction

1. 1. Renewable Generation and Electricity Demand Growth

1. 1. 1. Background

Over the last two decades, the widely appreciated impacts of greenhouse gas emissions on climate change have stressed the importance of decarbonization of energy production schemes. The global Carbon Dioxide (CO_2) emissions were required to be 45% below 2010 levels by 2030 and reach net-zero by 2050. Additionally, global energy-related CO_2 emissions were targeted to be cut by 40% below the 2010 levels by 2030 and reach net zero by 2060 [1]. For instance, in a meeting held in Kyoto, several European countries pledged to cut down their emissions to at least 5% by 2012, and then the target was increased to 20% by 2020 [2]. To help achieve these targets, several regulating measures in the power sector such as increasing the amount of Renewable Energy Sources (RES) based power generation were stressed by governments. International attempts have been made to lessen these emissions; therefore, policies are being set by authorities and organising groups for the adoption of more environmentally friendly technologies based on RES to meet these future global challenges. By 2020, the United Kingdom (UK), for example, aimed to achieve the following renewable energy targets [3]:

- More than 30% of electricity production is from renewables, including a considerable amount of small-scale electricity power generation systems that are mainly connected to the power distribution networks,
- 10% transport electrification from renewables, and
- 12% heating systems from renewables.

In the UK, the total renewable-based electricity generation share is about 39% of its total power generation of 76 GW by 2022 [4]. However, there has been a continuous increase in the utilisation of clean and renewable resources for energy generation and a significant reduction in the consumption of fossil fuels. Moreover, the increase in large-scale integration of electrified transport and decarbonised domestic heating systems are projected to increase the power generation demand.

By considering all these factors and the continuous population growth, a further increase in electricity demand is anticipated in the future [3].

The global climate change issue and the increased power demand have also driven many countries around the world to adopt such effective measures. Likewise, in Saudi Arabia, the greenhouse gas emitted by different sectors has increased by almost 200% from 1990 to 2017. Although coal has become obsolete in today's power generating stations in Saudi Arabia, a high amount of fossil fuels (65% natural gas, 35% oil) is being employed to meet local energy consumption. The shares of renewable energy systems were almost negligible until the "Saudi 2030 Vision" with the climate commitment has come into the picture in 2017. Policies were introduced to reduce fossil fuel subsidies, accelerate large-scale integrations of renewable systems, and support the diversification of the non-oil-based economy [5]. However, international challenges such as the pandemic of COVID-19 seemed to slow down the progression of such ambitious targets not only in Saudi Arabia but all over the world.

Saudi Arabia has started an ambitious campaign for sustainable energy that emphasises education and research opportunities, international investment and collaboration, and localization of the technology. Additionally, with the high potential for RES in the region, the Saudi authority has recently committed to increasing the share of renewables to 50% of its total power generation of 80 GW by 2030. This is because of the dynamically growing economy and population growth that spurred the high local electrical power demand. The use of renewables will include electric power generation, water desalination systems, agriculture supporting systems, and transport electrification. This ambitious approach will not only place Saudi Arabia as the world's largest renewable energy leader but also be an expert in the technology's development globally [6].

Technically, significant transformations in today's electric power systems seem to be required to maintain a reliable, secure, and affordable energy supply with all these measures and targets. The emerging concept of "smart power grids" has been developed as an optimal solution to address future challenges and ensure the effective deployment of existing infrastructure.

1. 1. 2. Development of Smart Power Grids

Principally, a smart power grid is an intelligent version of an electric power network developed to deliver electricity efficiently, sustainably, economically, and securely. There are several definitions of a smart grid proposed in the literature. The International Energy Agency (IEA) defined the smart grid as an electricity network that adopts digital and sophisticated technologies to supervise and control the electricity transport between prosumers (producers who can also be consumers). The detailed definition proposed by the European Smart Grids Technology Platform is as follows [7].

"*To summarise the definition of a smart grid the principal smart grid functional characteristics are:*

- *Self-healing from power disturbance events*
- *Enabling active participation by consumers in demand response*
- *Operating resiliently against physical and cyber attacks*
- *Providing power quality for the 21st century needs*
- *Accommodating all generation and storage options*
- *Enabling new products, services, and markets*
- *Optimising assets and operating efficiently*

A smart grid uses digital technology to improve the reliability, resiliency, flexibility, and efficiency (both economic and energy) of the electric delivery system. The strategy to achieve this vision hinges upon activities that directly address the technical, business, and institutional challenges to realising a smarter grid. These overall explanations of the smartening of electrical systems can be carried out in a city, on a national or regional scale, and can also be brought to the level of mini- or micro-grids. All electricity systems can be improved or optimised, but it is a key to determine what drivers are motivating investments and then to choose investments that can yield the most value for stakeholders."

The possible challenges to be addressed over the next years to accomplish a smart grid in the UK should be highlighted. The development of power distribution networks is the key transformation to meet the decarbonization targets through the integration of large-scale RES-based technologies to form smart grids [3].

Similarly, the Saudi Electricity Regulatory Authority (SERA) has worked on enabling measures to establish conceptual smart grids. Several technical studies funded by the SERA have been conducted to identify the smart grids and smart meter's contributions, functional requirements, and potential implementation challenges. The principal objective of such studies is to set a clear-milestones roadmap to facilitate smart grids in Saudi Arabia. The studies concluded that the implementation of the smart grid and smart meters would have high paybacks due to the direct profits of the power transmission and distribution system operators' initiatives. Smart grids can also activate the load shifting during peak times and this can result in an efficient operation of the electricity systems. These benefits can finally result in increased power generation hosting capacities, reduced use of fossil fuels, compact greenhouse gas emissions, and enhanced opportunities to export surplus electric power [8]. On the other hand, the future modernised electrical networks are anticipated to trigger some challenges such as power quality and harmonics issues due to the high utilisation of the Power Electronics (PE)-based power conversion systems [9]–[11].

1. 2. Overview of Power Harmonics

The term "Power Quality" firstly appeared in 1968 in a study specifying the requirement for electronic equipment for the U.S. Navy. Several years later, the reliability of electric power supply, which refers to the continuity of power to customers, tended to be the major concern among most electricity suppliers. Increased power network complexity, growing demand, power security, and environmental sustainability have triggered the next step in the development of the power system toward smart grids. This also means more complex power distribution networks due to the increased implementation of DER-based Distributed Generation (DG) systems, storage systems, enabling technologies like MVDC systems, and the latest information and communication technologies in the existing power systems. PE-based power conversion systems, which are being widely used to interface these clean technologies to the power grid at different voltage levels, are believed to be the main source of power quality issues in future networks, and thus the topic has drawn the attention of many researchers and engineers in the field of electric power systems [12], [13].

Power conversion systems that are based on semiconductor devices operating in switching mode can efficiently modify the voltage and current waveforms from one form to another depending on the loads' requirements. Rectification (AC-DC), inversion (DC-AC), DC regulating (DC-DC) as well as AC magnitude and/or frequency regulating (AC-AC) are the typical function of PEs power conversion systems [14]. Although recent Silicon Carbide and Gallium Nitride based devices are elected as promising technology for higher efficiency with higher switching frequencies, they are yet limited to relatively low power applications [15]. Power harmonics that are inherent problem associated with power conversion systems were thought to be limited to lower voltage levels. However, with the increased penetrations of the DER-based technologies and several large nonlinear loads introduced to distribution power networks over the last years [10], [11], the power harmonics related challenges and solutions have, therefore, attracted many in academia and industry.

Generally, the voltage and current in a power system are represented as sinusoidal waveforms of the power frequency of 50 or 60 Hz differing from one country to another. When a linear load such as resistive, inductive, capacitive, or a combination of all is supplied with a sinusoidal voltage, a proportional sinusoidal current (phase-shifted or in-phase depending on the type of the load) of the same supply frequency will be drawn. However, due to the development of power networks, the situation has become more complicated. With the presence of power converters, the current becomes distorted and no longer proportional to the supply voltage. The distorted current can be further analysed by signal analysis solutions such as the Fourier series and decomposed into the corresponding harmonic components, which can then be categorised as characteristic and non-characteristic harmonics. These harmonic components can also involve sub-harmonics and supra-harmonics depending on the range of frequency at which they occur [13].

1. 2. 1. Power Harmonic Components Analysis

The power harmonics in a power system are commonly characterised and quantified by their harmonic components. When the power harmonics are assumed periodic, the Fourier series solution can be used to represent a periodic non-sinusoidal signal

composed of multiple signals of different frequencies into their equivalents over the range of frequency of interest [14]. The Fourier series is expressed as follows.

$$f(t) = a_o + \sum_{n=1}^{\infty} [a_n \cos(n2\pi ft) + b_n \sin(n2\pi ft)] \tag{1.1}$$

where a_o is the DC component of zero frequency, a_n and b_n are the Fourier series coefficients, and f is the fundamental/power frequency. The coefficients can then be computed as:

$$a_0 = \frac{1}{T}\int_{-T/2}^{T/2} f(t)\, dt \tag{1.2}$$

$$a_n = \frac{2}{T}\int_{-T/2}^{T/2} f(t)\cos(n2\pi ft)\ dt \tag{1.3}$$

$$b_n = \frac{2}{T}\int_{-T/2}^{T/2} f(t)\sin(n2\pi ft)\ \ dt \tag{1.4}$$

Where T is the periodic time of the signal under analysis. Depending on the characteristics of the waveform to be analysed, some simplifications over the Fourier expression can be made to reduce the computational effort. For instance, when there is no DC component and the signal is symmetrical around the vertical y-axis, only a_n will be computed.

1. 2. 2. Power Harmonics Sequences

In a three-phase power system, like for the fundamental frequency component, the concept of the phasor rotating sequences for harmonic components is applied. Typically, there are three components: zero, positive, and negative sequences. The zero-sequence phasors have equal phase-shifted magnitudes and do not rotate. Positive-sequence phasors have equal magnitudes, uniformly 120-degree phase-shifted, and counter-clockwise rotation. The negative sequence is like the positive sequence but with clockwise rotation [13]. To clarify this phenomenon, with the

fundamental three-phase AC voltage, the harmonic components sequences are worked out as illustrated in Table 1-1. The conventional rotation of the fundamental AC phasors can be counterclockwise with phase A taken as a reference.

Table 1-1 Sequence of power harmonics.

Harmonic Order	Phase Angle			Rotation	Sequence
	A	B	C		
1st	0°	120°	240°	ABC	Positive
3rd	3×0° (0°)	3×120° (1×360° = 0°)	3×240° (720° =2×360°= 0°)	No rotation	Zero
5th	5×0° (0°)	5×120° (600°=1×360°+240° (240°)	5×240° (1200°=3×360°+120°) (120°)	CBA	Negative
7th	7×0° (0°)	7×120° (840°=2×360°+120°) (120°)	7×240 (1680°=4×360°+240°) (240°)	ABC	Positive
9th	9×0° (0°)	9×120° (3×360°=0°)	9×240 (6×360°=0°)	No rotation	Zero

The non-rotating triplen harmonic components such as the 3rd and 9th are of zero sequences since they are zero-degree shifted to each other. Harmonic orders such as 5th and 11th which are 120 degrees shifted to each other and rotate in opposite directions to that of the fundamental phasors, are of negative sequence. In contrast, harmonic orders such as 7th and 13th are of positive sequence as their phasors are also120-degree shifted to each other and have the same rotating sequence of the fundamentals. Apart from the fundamental frequency, the 2nd, 3rd, and 4th harmonic orders will have a pattern of negative, zero, and positive sequences, and this pattern continuously repeats for the rest of the harmonic orders. The harmonic order sequences can be significant in power harmonic analysis studies since they can develop serious impacts on power system components such as motor operation, neutral lines overloading, power transformers saturations, and other general effects as will be briefly discussed later in this chapter.

1. 2. 3. General Harmonic Indices

- **Total Harmonic Distortion (THD)**

The THD is the most utilised index for quantifying electric power harmonics [13], [14]. It is based on the harmonic components obtained from the Fourier series

solution and can be applied to distorted voltage and current traces. The voltage and current total harmonic distortion can be computed as:

$$Voltage\ THD = \frac{\sqrt{\sum_{h=2}^{\infty} V_h^2}}{V_1} \tag{1.5}$$

$$Current\ THD = \frac{\sqrt{\sum_{h=2}^{\infty} I_h^2}}{I_1} \tag{1.6}$$

where h is the harmonic order, V_h and I_h are the Root Mean Square (RMS) voltage and current, respectively, of the harmonic signal at h^{th} order, and V_1 and I_1 are the RMS voltage and current of the fundamental frequency component, respectively. However, when the traces are purely sinusoidal, the RMS quantities can be replaced by peak values in both equations with no impact on the solutions.

- **Total Demand Distortion (TDD)**

Another common index used to quantify the accurate harmonic distortion for current signals is the Total Demand Distortion (TDD). The main difference between THD and TDD is that the TDD is calculated based on the maximum rated current of the nonlinear load/harmonic source. This is a very useful index for applications in weak power systems with a relatively low Short Circuit Level (SCL) and can help overcome the confusion that the THD can cause when used in such a case [16]. The TDD can be expressed as:

$$Current\ TDD = \frac{\sqrt{\sum_{h=2}^{\infty} I_h^2}}{I_{max}} \tag{1.7}$$

where I_{max} is the maximum demand current of the nonlinear load/harmonic source at the fundamental frequency.

1. 2. 4. Power Harmonic Effects

Power harmonics can adversely impact most power system components [12], [13]. The most serious influences of power harmonics are summarised as follows.

- Power system's efficiency reduction,

- Ageing of the installed equipment due to the degradation of the insulation system,
- Power transformers and motor overheating and vibrations,
- High core magnetization losses in transformers and motors,
- Transformers and neutral conductors overloading in distribution systems,
- Malfunctioning and damage of metering equipment,
- Power Factor Correction (PFC) capacitors overloading and fuse damage,
- Maloperation of protective relays and circuit breakers,
- Impact on vulnerable electronics-based equipment and loads, and
- Interferences and distortions effects on communication systems.

1. 2. 5. Harmonic Analysis Methods

Harmonic analysis studies are performed to evaluate the harmonic performance of a power system. Several powerful computer-program packages adopting either frequency or time domain methods are employed to compute harmonic flow with the presence of nonlinear loads. These methods aim to detect resonant points, calculate harmonic distortions of voltage and current, evaluate harmonic power losses, investigate compliance with standard limits, design effective PPF, help plan for future renewables and PFC capacitor banks installations, etc.

- **Time Domain Solution**

The time domain solution, which has been commonly adopted for key studies such as transient stability, transmission lines, and switching transients, has involved the representation of the dynamic behaviour of the interconnected components of a power system by means of differential equations [13]. The resulting equation system is generally non-linear, which can then be solved using numerical integration. The most widely used time domain methods are the state variables and Norton equivalents-based nodal analysis. The states variables approach used extensively in electronic circuits was first employed for AC-DC power systems [17], while the nodal method is more efficient and commonly used in the electromagnetic transient studies of power systems [18].

The harmonic solution derived from the time domain programmes such as an Electromagnetic Transient Program includes solving a system for the steady-state and then utilising the Fast Fourier Transform (FFT). This involves a considerable computation time even for comparatively small systems and some techniques have been introduced to accelerate the steady-state solution process [19]. Another issue related to the time domain solutions for performing harmonic studies is the components modelling complexity with distributed or frequency-dependent variables. To overcome these difficulties, frequency domain solutions were proposed [17].

- **Frequency Domain Solution**

The frequency domain method provides a steady-state solution for the consequential impact of certain individual frequency (or harmonic) injections throughout a power system, without considering the harmonic interactions between the power network and the nonlinear components such as the control system [13]. The most well-known method of the frequency domain solution is the Decoupled Harmonic Power Flow (DHPF). Generally, this approach uses a single harmonic source and single-phase analysis solutions to evaluate the harmonic flow under the assumptions of a balanced and symmetrical power system. This approach is widely adopted for the fundamental frequency load-flow studies, but it is performed separately for each harmonic order, and it is commercially used to verify the harmonic distortions compliance, and performance of power filters [17]. In this approach, the time-invariant harmonic currents generated by the harmonic sources are either determined by the manufacturer or obtained from a model accurately developed for a specific operating condition. Therefore, the nonlinearity is overcome by a constant harmonic current source and a harmonic flow can then be performed. When there are no other comparable harmonic sources in the power network, the impact of a given harmonic source is usually evaluated with the use of the equivalent harmonic impedances [20].

The approach of a current source model for a harmonic source is still widely implemented for determining the harmonic penetrations through the power networks and harmonic filters design [17], [21]. The frequency domain method can

also be applied to an asymmetrical power system. The asymmetry that can be observed in practical systems justifies the necessity for multiphase harmonic flow analysis solutions. The basic power system component of a multiphase model is the overhead conductors and/or cables, which need to be accurately represented by an appropriate model at any frequency, involving mutual effects, neutral conductors, skin effects, etc [13]. This model is then combined with the other harmonic models of the network components to perform the complete harmonic analysis study for each phase.

The current source modelling technique is also applicable to assess the distortions resulting from multiple harmonic sources when the interactions between them are negligible. The superposition principle is then used to derive the aggregated harmonic distortions throughout the power network. Lastly, either deterministic or probabilistic studies can be conducted with the knowledge of the magnitude and phase of various harmonic sources' components to accurately evaluate the overall distortion [22], [23].

- **Iterative Solutions**

The adoption of PE-based enabling technologies, such as the High Voltage Direct Current (HVDC) system and Flexible Alternating Current Transmission Systems (FACTS) devices in a high-voltage power system, has increased the system's SCL. This implies that the principle of superposition would not be applicable when evaluating the multiple harmonic sources impacts. This is because of the high dependency between the different harmonic sources and the state of the power system, and thus accurate harmonic performance can only be achieved by iterative solutions of the nonlinear equations that model the steady-state of the complete system [24]. The system steady-state is significantly, but not entirely, described by the harmonic voltage components all over the network. This sort of analysis is commonly referred to as the harmonic domain solution, and it differs from the frequency domain methods by modelling the nonlinear interactions between harmonic sources and the power system components. With an accurate derivation of the nonlinear equations describing the system's steady-state, the harmonic domain solutions also have the advantages of including power converters, control

circuits, PWM-based switching instants, the saturation of the transformer core, etc. [25].

Several methods were proposed to acquire accurate nonlinear equations for describing the system's steady-state. The nonlinear devices should be linearized for a given boundary condition and represented by separate linear equations, then they are combined with a set of linear equations of the power system's components under the study. The system is then solved for the same operating condition using, for example, the FFT for the sampled waveforms [26], or the harmonic phasor analysis [27].

In this work, the frequency domain solution, which is widely used for evaluating harmonic distortions, compliance with standard limits, and Passive Power Filter (PPF) design when the interactions between nonlinear devices and the power network are assumed negligible, is adopted. The frequency domain approach requires an accurate realisation of the system under the study in terms of the system components and harmonic sources specifications. Nowadays, power simulation packages with powerful tools for harmonic modelling can help perform accurate harmonic analysis studies with less effort and time burdens. The following numerical example aims to introduce a powerful simulation environment for harmonic analysis studies, the Interactive Power System Analysis (IPSA). This software will be used later to assist evaluate the harmonic propagations of the MVDC converter into a real data-based power network and validate the harmonic performance of an optimally designed PPF.

1. 2. 6. Numerical Example of a Simple Power Network for Harmonic Analysis

1. 2. 6. 1. System Description and Modelling for Harmonic Analysis

The simple power system is shown in Figure 1-1, consisting of a harmonic source connected to the secondary side of a power transformer through an overhead line, which is represented by its nominal-π model that introduces a capacitive element at both ends for which the parasitic resistance of the capacitive elements is assumed negligible. This example aims to illustrate the harmonic propagations into the

simple power system using a MATLAB coded analytical DHPF solution and IPSA power system simulator.

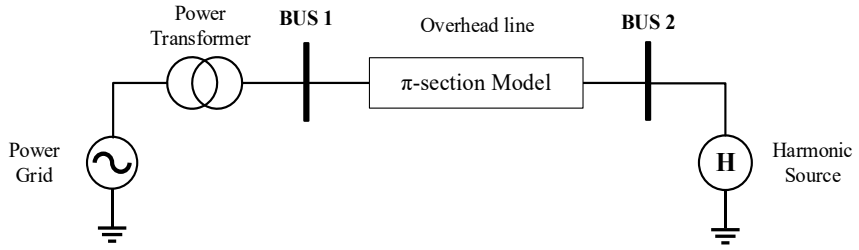

Figure 1-1 Single line diagram of the example system.

In this simple example, the system is assumed to be symmetric and balanced. Therefore, the positive and negative sequence equivalents are identical, and only one circuit is required for the harmonic equivalent model as displayed in Figure 1-2. The per unit (p.u.) system parameters shown in Table 1-2 are calculated based on the 100 MVA and the base impedance at the low voltage level of 10.89 Ω. It must be noted that the resistive part of each component is neglected to investigate the worst-case scenario of harmonic resonances and interactions between the harmonic source and the power system.

Related assumptions made in this demonstrative example:

1- The three-phase system is balanced and symmetrical.
2- The system components' reactance parts are dominant.
3- The inductance of each component increases linearly with frequency.
4- The effects of the control system of the harmonic source are negligible.

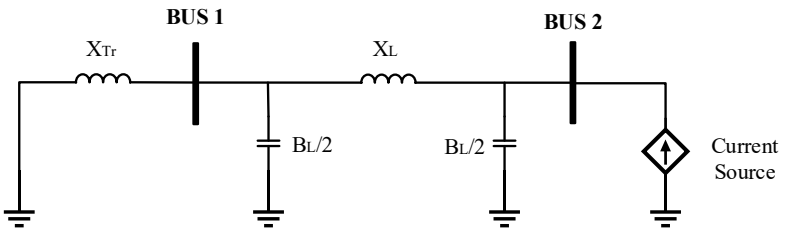

Figure 1-2 Harmonic impedance diagram of the example system.

Table 1-2 Power network parameters.

Power System Parameter	Value (p.u.)
Power Grid impedance	0
Transformer reactance (X_{Tr})	0.20
Line reactance (X_L)	0.10
Line susceptance (B_L)	0.02

The power grid that is considered an infinite power source of a pure sinusoidal output with zero impedance at the fundamental frequency, is represented as a short circuit for harmonic frequencies. The 10-MVA, 132/33 kV (Δ/Y), power transformer is represented between the power source and BUS 1 by its fundamental frequency reactance (X_{Tr}) for harmonic frequencies (h) as follows:

$$Z_{Tr} = jhX_{Tr} \qquad for \quad h > 1 \tag{1.8}$$

For the overhead lines, a simplified nominal-π model is used. The harmonic model is calculated using its fundamental frequency reactance (X_L) and susceptance (B_L) as follows:

$$Z_{X_L} = jhX_L \qquad for \quad h > 1 \tag{1.9}$$

$$Y_{B_L} = jh\,\frac{B_L}{2} \qquad for \quad h > 1 \tag{1.10}$$

The harmonic source, which can be a PE-based power converter, is represented by a harmonic current source connected to BUS 2. In this simple system, the harmonic source is assumed to produce only positive and negative sequences of characteristic harmonics up to 50th as listed in Table 1-3. Typical harmonic magnitudes are adopted to simplify the calculations for the harmonic solution. For instance, the 5th harmonic order is of one-fifth amplitude with respect to the fundamental component, which is 1 p.u. This is assumed for all harmonic current components (I_h). The phase angle of each harmonic current is assumed aligned with the fundamental current since there is only one harmonic source presented in this simple system.

Table 1-3 Harmonic Source Content.

Harmonic Order	Magnitude (p.u.)	Harmonic Order	Magnitude (p.u.)
5	0.200	29	0.034
7	0.143	31	0.032
11	0.091	35	0.029
13	0.077	37	0.027
17	0.059	41	0.024
19	0.053	43	0.023
23	0.043	47	0.021
25	0.040	49	0.020

1. 2. 6. 2. Analytical Solution (using MATLAB script):

The MATLAB coded solution was implemented for the given system components models and harmonic currents data to perform harmonic analysis in the frequency domain. In this approach, the bus admittance matrix is built first as follows.

$$Y_h = \begin{bmatrix} Y_{11} & -Y_{12} \\ -Y_{21} & Y_{22} \end{bmatrix} = \begin{bmatrix} \frac{1}{Z_{Tr}} + \frac{1}{Z_{X_L}} + \frac{Y_{B_L}}{2} & -\frac{1}{Z_{X_L}} \\ -\frac{1}{Z_{X_L}} & \frac{1}{Z_{X_L}} + \frac{Y_{B_L}}{2} \end{bmatrix} \quad (1.11)$$

Where Y_{11}, Y_{22} are the admittances corresponding to BUS 1 and BUS 2 respectively, and Y_{12} is the admittance between BUS 1 and BUS 2. The impedance matrix is then calculated as follows.

$$Z_h = \begin{bmatrix} -Z_{h_{11}} & Z_{h_{12}} \\ Z_{h_{21}} & -Z_{h_{22}} \end{bmatrix} = Y_h^{-1} \quad (1.12)$$

The harmonic impedance scan was performed for a 0.5 frequency step, and Figure 1-3 identifies the possible parallel and/or series resonances that can contribute to harmonic magnifying or attenuating behaviour in the power system. It can be observed that the system has two parallel resonance points around the 15th and 48th harmonic orders.

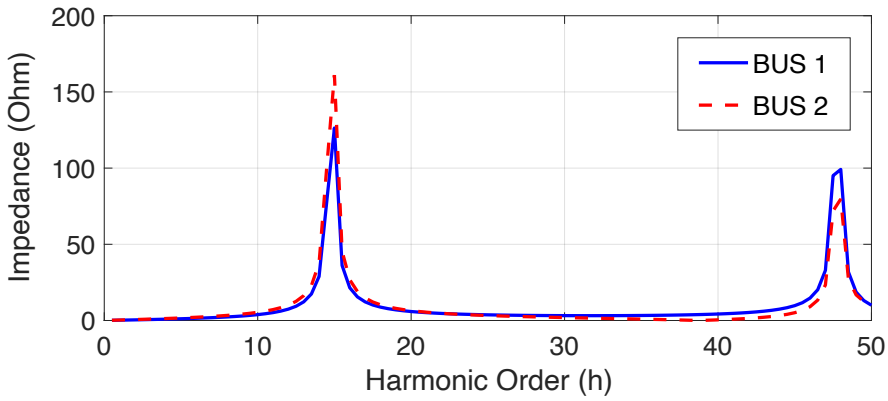

Figure 1-3 System harmonic impedance seen from the two buses.

Consequently, with the harmonic source connected to BUS 2, the harmonic voltage components at Bus 1 are obtained using the transfer impedance $Z_{h_{21}}$ between Bus 2 and BUS 1, while the harmonic voltage at Bus 2 is found utilising the driving point impedance $Z_{h_{22}}$ as follows:

$$V_{h_{BUS\,2}} = Z_{h_{22}}\, I_h \qquad for \quad h = 2, 3, \ldots 50 \tag{1.13}$$

$$V_{h_{BUS\,1}} = Z_{h_{21}}\, I_h \qquad for \quad h = 2, 3, \ldots 50 \tag{1.14}$$

It can be noticed from Figure 1-4 that BUS 1 and BUS 2 voltage spectra have higher harmonic contents around the 15th and the 48th harmonic orders due to the parallel resonances developed by the line shunt capacitances.

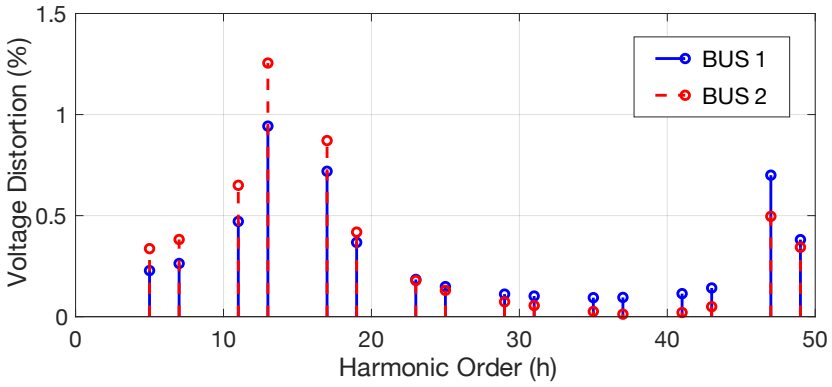

Figure 1-4 System harmonic voltage obtained from the analytical solution.

The presence of the line capacitive element has triggered the corresponding resonances with the system inductances. At BUS 1, for instance, the transfer impedance plot with respect to frequency indicates possible amplification of harmonic components as shown in Figure 1-5. The harmonic orders around which the system impedance resonance occurs will be further amplified by the peaks of the transfer impedance compared to those away from resonance points.

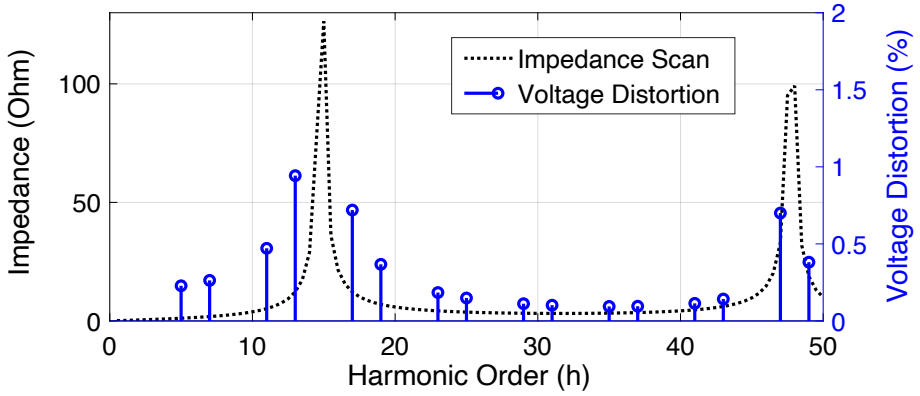

Figure 1-5 Amplification of the system harmonic voltage.

1. 2. 6. 3. Simulated Analysis using IPSA

The IPSA power systems simulator can perform frequency domain harmonic analysis studies. It can conduct positive and negative impedance scans, harmonic penetrations, and compute corresponding voltage traces. The simple two-bus system depicted in Figure 1-2 with parameters shown in Table 1-2 is modelled using IPSA, and the harmonic source is represented by a harmonic source that enables users to assign the magnitude and angle of each harmonic current component shown in Table 1-3. The p.u. calculations are based on the same base values of the analytical solution.

The resulting voltage traces of BUS 1 and BUS 2 are plotted using IPSA and depicted in Figure 1-6(a) and Figure 1-6(b), respectively. The corresponding harmonic contents of these voltage traces, which are identical to what the analytical solution found, are shown in Figure 1-7.

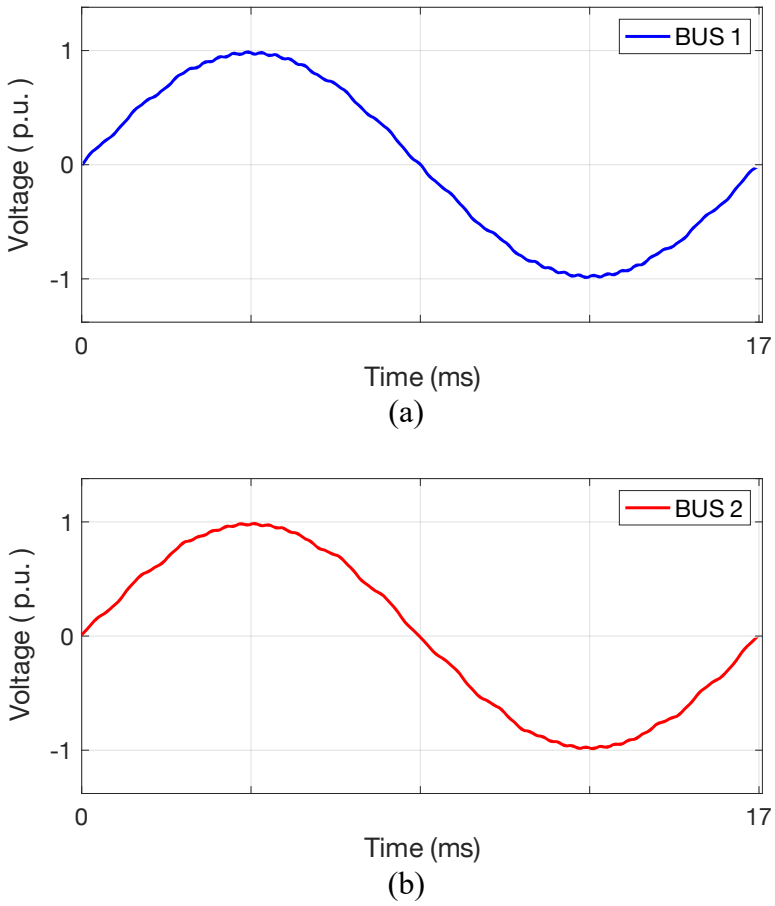

Figure 1-6 Voltage traces obtained from IPSA solution (a) at BUS1, (b) at BUS2.

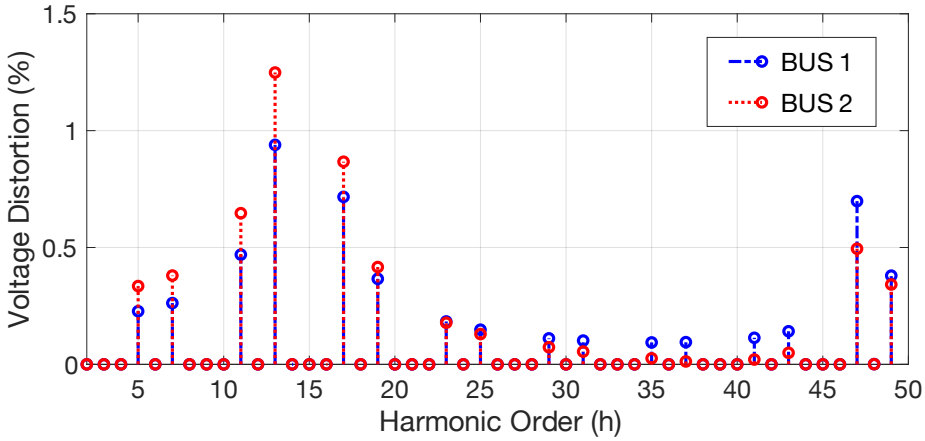

Figure 1-7 System harmonic voltage obtained from IPSA solution.

This simple example of harmonic flow analysis provides insight into the interactions between the harmonic currents of a harmonic source and system

components modelled for harmonic propagations and resonances investigations. The comparison between analytical and simulated solutions helps determine the suitability of the power system simulation software for such studies. However, IPSA offers different harmonic models of the power system components for the user to define, and thus a realistic and reliable harmonic flow analysis of large and complicated power systems with different topologies and more specifications can be achieved with high accuracy and less computational effort.

1. 3. Research Motivation

The international upward trend of decarbonization of the energy sector associated with the global growing energy consumption has motivated governments to set ambitious targets and effective policies. Consequently, more RES-based systems and their enabling technologies such as the MVDC systems are being integrated into today's power networks. The technical challenges, related to such high penetrations of renewables and high-power demand, necessitate the development of the existing power network to increase its hosting capacity and address smart grids requirements. However, due to the intermittent nature of the RES and the wide use of high-power PE-based power converters in the existing power systems, power quality and harmonics issues have received a great deal of attention. Power harmonics can have serious impacts on the power system components in different aspects, and thus many concerns regarding the power harmonic challenges and solutions can arise in future power networks. Therefore, this research work primarily aims to investigate the severity of power harmonics in medium voltage AC distribution networks and approach their challenges and solutions using advanced AI-based solutions including the newly proposed optimization algorithms and ANN systems.

- **MVDC Converter Modelling for Harmonic Analysis Studies**

The introduction of the MVDC links to the power distribution networks will help increase the networks' hosting capacity for more DER-based power sources and meet future growing energy consumption without triggering stability and thermal issues. The development of a detailed MVDC converter model and control system with an interleaved Sinusoidal Pulse-width Modulation (SPWM) scheme is

required to mitigate the significant harmonic components and thus enable accurate harmonic analysis studies. When such an application is to be modelled to validate its concept of operation, the simple Proportional-Integral (PI) controller stands out as the most favourable option to be adopted. However, the tuning of the PI controller's parameters remains a challenging task with the variety of classical control design approaches. Therefore, the performance of the Loop-shaping technique should be explored for the control design of the MVDC converter. Besides. the performance of the control system and the effectiveness of the harmonic reduction method should be analysed.

- **MVDC Converter Harmonic Analysis in Distribution Networks**

The severity of the power harmonics injected by an MVDC converter into the power distribution networks must be investigated. Different harmonic models of the power system components have been proposed and reported in the literature. However, when accurate power harmonic analysis studies are required to be performed in the distribution networks, concerns can arise about the selection of the most accurate harmonic model of a system component. Therefore, the harmonic models of key power system components should be analysed from the distribution network point of view, and recommendations for realistic power harmonic flow analysis studies must be provided. A real data-based power network is required to be modelled for conducting an accurate propagations analysis of the harmonics generated by the MVDC converter, and the voltage distortions against the defined standard limits must be investigated for any potential risks to sensitive loads.

- **Passive Power Filter Design and Harmonic Performance Analysis**

The parameter design of PPF has been widely acknowledged as an optimization problem, and novel nature-inspired optimization algorithms are being developed and proposed for a wide range of applications. The recently developed Manta Ray Foraging Optimization (MRFO) algorithm has shown considerable computational progress, a powerful ability to solve non-linear optimization problems, easy

implementation, and relatively fewer parameters that require to be adjusted for several applications. However, the performance of the MRFO algorithm has not been investigated for the PPF parameter design problems applications. Additionally, the superiority of the MRFO algorithm can be validated against recently proposed algorithms that have general similarities in inspiration and hunting behaviour modelling. Moreover, the evaluation of an optimally designed PPF harmonic performance in power distribution networks subjected to uncertainties and inevitable variations has not been addressed. The Monte Carlo Simulation (MCS) approach, which is a computer-based simulation technique that uses probabilistic theory and statistical solutions, has been widely adopted to tackle such uncertainties.

- **Harmonic Distortions Estimation using Artificial Neural Networks**

Renewable resources-based power sources are predicted to cause significant harmonic distortions in today's power networks due to the increased utilisation of power conversion systems, which are widely recognized as harmonic sources. Power harmonics, which are one of the crucial power quality problems, would lead to undesirable effects on the power system such as increased power losses, overheating and vibration of power transformers and motors, degradation of power factor, and maloperation of protection systems. These harmonics-related financial and technical consequences have stressed the necessity for effective measures to maintain harmonic distortions at lower possible levels to ensure compliance with the standard limits. However, identifying the actual contribution of an offending harmonic source can be a challenging task, especially with multiple harmonic sources connected, changes in the system's characteristic impedance, and the intermittent nature of renewable resources. Therefore, an improved harmonic distortion estimating method based on an ANN system taking the location-specific data into consideration should be developed to model the admittance of the harmonic source under the estimation, capture its harmonic performance over different operating conditions, and provide accurate harmonic distortions estimations.

1. 4. Research Objectives and Contributions

The main objective of this research work is to investigate the severity of power harmonics in the distribution networks with the presence of MVDC converters and approach harmonic solutions considering the potential application of optimization algorithms and ANN systems. Details of the research objectives and contributions are as follows.

Objective 1:

Developing an accurate model of the MVDC converter for harmonic analysis studies in medium voltage AC distribution networks.

Contribution 1:

- A comparative study of the MVDC system and power converter topologies to nominate the best candidate for MVDC system applications was undertaken.
- A detailed model of the MVDC converter including PE devices with switching behaviour was developed for harmonic analysis studies.
- A suitable control scheme with the controller parameters tuned using the robust and simple Loop-shaping technique was developed and its performance was investigated.
- An interleaved SPWM scheme to reduce the overall system's harmonic emissions was proposed and its effectiveness was discussed.
- The harmonic performance of the developed model will be compared to that of the established models to validate its superiority.

Objective 2:

Developing a harmonic model of a real data-based medium voltage power distribution network to investigate the MVDC converter's harmonic propagations and penetration through the AC network.

Contribution 2:

- A critical review of the reported harmonic models of the power system components was conducted to determine the most reliable models for accurate power harmonic analysis studies.
- Real data of the case study power system was collected, and the power system was modelled for the harmonic analysis study.

- Thorough harmonic propagations, penetrations, and resonances of the real power system using the frequency domain approach were analysed.
- Total and individual harmonic distortions were evaluated against harmonic standard limits to identify any potential risk on nearby sensitive loads.

Objective 3:

Investigating the feasibility of the recently developed Manta Ray Foraging Optimization (MRFO) algorithm for the PPF applications and investigating its performance against newly proposed algorithms. Also, a method for evaluating statistically the harmonic performance of such an optimally designed PPF with uncertainties at the network level is to be developed.

Contribution 3:

- A critical review of the optimization algorithms employed for PPF applications was undertaken.
- The problem formulation, objective function, and constraints were set for the PPF parameters design problem.
- A comprehensive comparison between the MRFO and the most recently proposed optimization algorithms was achieved for superiority validation.
- An analytical approach based on the MCS was developed to extensively evaluate the performance of an optimally designed PPF in a power system considering the variations and uncertainties at the network level.

Objective 4:

Exploring the feasibility of the ANN for estimating the true harmonic distortions of a grid-connected power converter application with multiple harmonic sources connected, changes in the system's characteristic impedance, and the intermittent nature of renewable resources.

Contribution 4:

- A critical survey of the ANNs utilised for power harmonic distortions estimation was conducted.
- An improved harmonic distortions estimator was proposed and developed based on voltage, current, and location-specific signals.

- A simple power system including several renewable systems and events at the power network level was simulated to investigate the variations in the harmonic performance of a solar PV power inverter.
- A multilayer perceptron ANN was trained using the simulated system results and the optimal number of neurons in a hidden layer was investigated for a relatively small prediction error.
- The proposed estimator was validated in the IEEE 34-bus test feeder with established harmonic sources measured from a test field.

1. 5. Research Limitations

Generally, the developed systems in this work require high accuracy and thus require a larger number of samples and computational time (i.e., simulation time). Since most of the work in this thesis was validated using simulation platforms, technical and convergence issues for several methodologies are anticipated. Depending on the nature and requirements of a study, different methodologies for approaching power harmonic solutions in today's power systems can be integrated and this would lead to more computational complexity. Furthermore, experimental validation of this work in real power systems would require intensive consideration of auxiliary filtering and protection systems. However, approaches and principles implemented in this thesis remain valid irrespective of the power levels.

In **Chapter 2**, different classic and advanced control configurations and topologies including Phase-Looked Loop (PLL) systems can be adopted, and realistic assumptions about the delay of control and communication systems can cause some variations. Additionally, power transformer windings are not usually symmetrical and loading conditions of power distribution networks are not always balanced. These different factors would cause some variations in the harmonic performance of the real Medium Voltage Direct Current (MVDC) converter.

In **Chapter 3**, the decision on available harmonic models of the key power system components in the frequency domain can lead to uncertainty for large power systems. The parameters required for these established harmonic models seem to depend on assumptions and field measurements, which would also lead to difficult implementation and misestimation of harmonic resonances and indices.

Although typical values for coefficients of the optimization algorithms adopted in this work were used, better performance can be achieved by searching for optimal settings for these parameters. Moreover, for the stochastic harmonic performance of Passive Power Filters (PPF) using Monte Carlo Simulation (MCS), normal and/or uniform distribution functions may not accurately represent some real-life events. Prior knowledge of the loading condition and configuration, PPF topology, and harmonic emissions of a harmonic source is required to describe uncertainties in **Chapter 4**.

In **Chapter 5**, the proposed harmonic distortion estimator requires a larger training data set and computational effort for accurate performance. Signal synchronization is one of the key challenges of system implementation, especially in the training and testing stages. The offline prediction stage requires an appropriate delay to compensate for the mismatch between input and output signals. Inherent fault tolerance of such an ANN-based system, which was deliberately excluded in this work, would unfavourably affect harmonic distortion estimation.

1. 6. Thesis Outlines

The rest of this thesis is structured as follows.

Chapter 2 presents the development of the harmonic model of the MVDC converter. An overview of the different configurations of the MVDC systems and a concise comparative analysis of the multilevel power converter topologies for such applications are provided. The topology, control system, and interleaved SPWM scheme of the MVDC system are discussed. The MVDC system performance at the fundamental and harmonic frequencies for different operating conditions is presented.

Chapter 3 is dedicated to the harmonic modelling of the real data-based power network. It also presents the MVDC system's steady-state performance in the Albaha power network with different cases including the development projects in the region. A comparison between the established harmonic models of the power system components is conducted, and the Albaha power network model for the harmonic analysis study is presented.

The MVDC converter harmonic propagations into the Albaha power network at different voltage levels are analysed and evaluated against the standard limits. Potential harmonic issues and impact on nearby electronics loads are highlighted.

In **Chapter 4**, the parameters of a PPF are optimally designed using the recently developed MRFO algorithm, and an analytical harmonic analysis method is proposed. A thorough literature review of the optimal design approaches and optimization algorithms implemented in this area is undertaken. The formulation of the optimization problem and decision on the objective function and constraints are discussed. The superiority validation of the MRFO algorithm among the most recently proposed optimization algorithms is presented. The harmonic performance of the optimally designed PPF using the proposed MCS-based approach including uncertainties is discussed.

An improved power harmonic distortions estimator using the ANN system is introduced in **Chapter 5**. A review of previous work and an overview of the ANN-based system are presented. A simple power system simulated with several renewable systems and power events at the network levels on which the training of the ANN-based is discussed. The process of training and prediction stages of the proposed system is detailed. The validation of the estimator performance in the IEEE 34-bus test feeder with established harmonic sources measured from a test field is discussed.

Finally, the conclusions drawn from this research work and potential directions for future work are provided in **Chapter 6**.

Chapter 2. MVDC Converter Modelling for Harmonic Analysis Studies

This chapter aims to develop an accurate model of the Medium Voltage Direct Current (MVDC) converter for harmonic analysis studies in medium voltage AC distribution networks. A comparative study of the MVDC system and power converter topologies to nominate the best candidate for MVDC system applications is undertaken. Next, a detailed model of the MVDC converter including Power Electronics (PE) devices with switching behaviour is developed for accurate harmonic analysis studies. This also includes a suitable control scheme development and an interleaved Sinusoidal Pulse Width Modulation (SPWM) scheme to improve the overall system's harmonic emissions. The harmonic performance of the developed model is compared to that of the established models to validate its superiority.

2. 1. Introduction to MVDC Technologies

Modern power systems are increasingly adopting power conversion systems for renewable energy generation and enabling technologies such as High Voltage Direct Current (HVDC) and Flexible Alternating Current Transmission Systems (FACTS) devices and other applications. Due to the rising use of power electronics-based technologies, it is expected that power distribution networks would also be contaminated with considerable harmonic distortions [11]. Power distribution networks are typically operated in a radial configuration with normally open points connecting adjacent networks and providing alternative power supply routes for planned or unplanned power outages. The radial configuration provides a distinctive benefit due to its inherent operation and protection simplicity. However, the increasing penetration of renewables and growing electricity consumption have led to key challenges in the existing power networks, which cannot be addressed via conventional network reconfiguration methods [28]. Conventional network reinforcement offering an additional network capacity is an unfavourable option due to its cost and implementation difficulty. Therefore, innovative solutions to the existing networks have been proposed to overcome such disadvantages. The method of interconnecting (or meshing) the existing radial networks, which helps

relieve the stress on heavily loaded networks, is practically adopted in today's distribution networks due to its technical benefits such as reliability of supply improvement, load balancing between distribution networks, voltage profile enhancement, and power losses reduction. Nevertheless, the increase in fault current levels, which would necessitate more complicated and costly protection schemes, is the main drawback of this approach [29].

An alternative flexible connecting method over the radial and mesh configurations is the DC link, which is achieved by utilising PE-based power converters. Instead of regular circuit breakers, the MVDC system can provide the following features to the AC distribution networks [28], [29]:

- Connectivity between AC networks regardless of the synchronisation conditions of line voltage magnitude, phase angle, phase sequence, and operating frequency,
- Flexible and dynamic controllability of the active power flow between the interconnected networks, and therefore increasing the hosting capacity for more renewable resources-based technologies,
- Independent control of the reactive power at each AC terminal, and thus dynamically regulating the AC voltage. The MVDC system can additionally perform the Static Synchronous Compensator (STATCOM) functionality,
- Active fault isolation for the AC networks and the controlled fault current contributions depending on the current control loop of the MVDC converters,
- Power quality improvement such as voltage imbalance, sags and swells, flickers, and low-order harmonics mitigation, and
- Ancillary services such as reactive power compensation, black-start, and post-fault supply restoration through healthy AC networks.

The advantages associated with such a technology would lead to increased utilization of the MVDC system in today's power networks. However, power harmonics have recently attracted attention because of the growing use of PE-based power conversion systems [11]. Harmonics are known to cause excessive heating and power losses in power system components, as well as harming consumer electronics, industrial drives, and communication systems. Furthermore, they have

the potential to drastically reduce a power network's capacity for high DER penetrations. Harmonic distortions can also impact the capacity of power transformers and underground cables [30]. As a result, an accurate harmonic model of the MVDC converter is required to investigate its harmonic emissions severity, propagations, effects, and solutions in AC networks. This work aims to develop an accurate model of the MVDC converter for accurate harmonic analysis studies including a harmonic emissions reduction solution at the power converter level.

2. 2. Previous Studies on MVDC Technologies

In the literature, there is a lack of published work related to MVDC converter modelling and control development. However, the MVDC systems are appointed as a promising technology for today's distribution networks to accommodate the high penetrations of DG systems with increasing power demand [31]–[39]. These technologies with a suitable control system can also help reduce power losses, improve power supply, and compensate for load unbalancing. The study conducted in [40] investigated the impact of renewable resources on the distribution network and showed that the controllability of MVDC systems can increase the hosting capacity for distributed generators and the loading capability of the network while maintaining the voltage of the nodes within the standard limits. In [32], an optimization method was developed based on a comparative study of the conventional reinforcement measures and the use of the MVDC system to enable more renewable-based technologies in the distribution networks, while an assessment of the MVDC system including different topologies, degrees of freedom, and performance against conventional network reinforcing measures was reported in [33].

An application of the MVDC technology to boost the penetrations of solar photovoltaic and energy storage systems in a distribution network was presented in [34]. Furthermore, a method based on nonlinear optimization was developed in [32] to determine the possible operating region of an MVDC system for different load and generation conditions within the AC networks. The authors in [41] implemented an algorithm to evaluate the potential increase in hosting capacity due to the use of an MVDC system for renewables in two interconnected distribution

networks. In [42], the impact of the active power flow control on AC network voltage profiles was investigated. The study focused on the control effectiveness of a multi-terminal MVDC system to minimise voltage deviation among multiple AC networks. However, the impact of both active and reactive power control on voltage profiles and distributed generation penetrations was assessed in [34].

The power system reinforcement offered by the utilisation of an MVDC system connecting two adjacent distribution networks was discussed in [29]. It considered the existing distribution network to be replaced by a DC circuit with power conversion units installed at each substation. This approach would improve the power transfer capacity, hosting capacity for more renewable systems, and overall efficiency of each AC network.

The influence of various control systems on the MVDC systems operation was also discussed in a few publications. A control scheme for an MVDC system was proposed for supply restoration capability in power distribution networks in [35], [43]. Two switchable control schemes were introduced for the normal operating conditions and post-fault restoration, and a smooth transition method between the control modes based on the design of the Phase-Locked Loop (PLL) circuit was proposed. Furthermore, a control system for a balanced DC voltage operation of a scaled-down MVDC system was proposed in [39].

There is a limited number of publications dealing with the harmonic modelling of an MVDC converter and its harmonic propagations into the distribution networks. A modelling method for an MVDC system for harmonic analysis studies was presented in [44], where the switching device detailed model is substituted by a current source controlled by a switching function that simulates the PWM instants to reduce the computational complexity. This method shows an excellent harmonic performance in comparison with the average model of power converters but is not as accurate as a detailed switching behaviour-based model and thus it would result in less accurate harmonic analysis studies in the AC power network. In [45], the harmonic performance of an MVCD system was analysed within the DC circuit that incorporates power cables. However, the harmonic propagations of the MVDC converter into the AC network have not been investigated. Also, the AC output current traces of the MVDC converter were shown to have relatively high

distortions, which indicates the absence of the interleaved PWM algorithm that must be incorporated in the case of cascaded topologies.

Therefore, the main aim of this part of the thesis is to develop an accurate harmonic model of the back-to-back MVDC system with a detailed representation of the switching devices to investigate its harmonic performance in the power distribution networks. A cascaded power converter topology will be developed, and the impact of the interleaved SPWM on the harmonic performance of the MVDC converter will be investigated. The active power and reactive power control mode and DC voltage and reactive power control mode will be implemented using the simple and effective PI controllers tuned using the Loop-shaping method. The harmonic performance of the developed model will be compared to that of the established models to validate its superiority.

2. 3. Different Structures of MVDC Systems

There are a variety of MVDC systems configurations for distribution networks depending on the arrangements and operating requirements of the power converters adopted, and can be classified into, but not limited to, Back-to-Back, Multi-terminal, and Unified Power Flow Controlling (UPFC) systems. These topologies are well established for high-voltage transmission systems, and custom power devices for power quality applications at low voltage.

2. 3. 1. Back-to-Back MVDC System Topology

The back-to-back configuration is shown in Figure 2-1, consisting of two power conversion units connecting two AC networks via a DC link to develop an asynchronous AC-AC connection [35], [46]. These power conversion units can be two-level, three-level, multilevel, or cascaded Voltage Source Converter (VSC) based power converters. The coupling transformers are used to interface each power conversion system, provide grounding for the system to suppress fault current, match grid voltages to the power converter AC voltages, and help smooth the fundamental current. However, some recent studies have proposed transformerless topologies aiming to reduce the size and cost of the system [36].

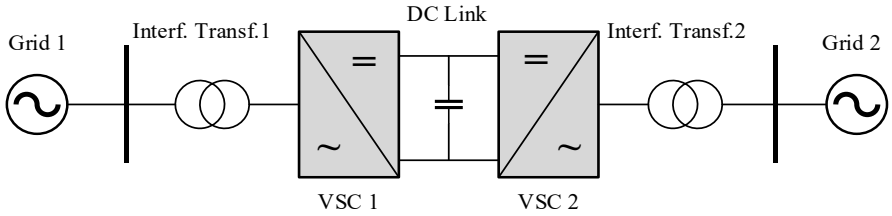

Figure 2-1 Back-to-back MVDC system topology.

2. 3. 2. Multi-terminal MVDC System Topology

The multi-terminal configuration depicted in Figure 2-2 is an extended version of the back-to-back topology and enables the connection of more than two AC networks through a common DC link [47]. Although this topology can provide similar features to the conventional back-to-back systems and ensure improved security and reliability of supply, it requires more sophisticated control, higher cost, and larger size systems.

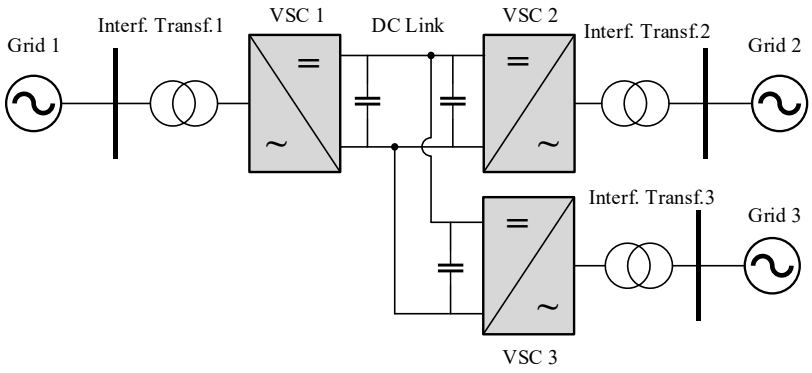

Figure 2-2 Multi-terminal MVDC system topology.

2. 3. 3. Unified Power Flow Control (UPFC) System Topology

The UPFC system displayed in Figure 2-3 comprises shunt and series-connected power conversion units linked via a common DC circuit [46], [48]. The series-connected power converter controls the voltage magnitude and phase angle at its connection point, in that way the power flow is controlled between interconnected networks. On the other hand, the main role of the shunt power converter is to deliver

the power required by the series converter through the DC link and provide independent control over the reactive power at its AC connection point.

The main benefit of the UPFC system is the high potential power flow that can be achieved by a relatively smaller rated power conversion system imposing voltage magnitude and phase angle differences. However, this feature is dependent on the network's configurations, operation constraints, normal operating conditions, and the location of the UPFC system. Inherent drawbacks of the UPFC are the requirements for a complicated control scheme and protection system to undermine the disturbances and fault levels across the AC networks, and that the UPFC system should be connected between power systems that are already synchronised.

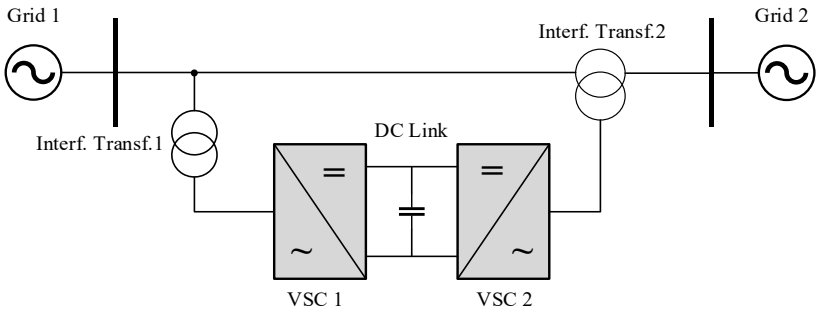

Figure 2-3 UPFC system topology.

2. 4. Multilevel Power Converter Topologies

A PE-based device that can operate as either a power inverter (DC to AC) or a power rectifier (AC to DC) is called a power converter. The two-level power converter with the topology shown in Figure 2-4 has been the most commercially available and widely used for low voltage applications. The main evident difference between the two-level and multilevel power converters as their names imply is the output voltage; the two-level AC output phase voltage alternates between $+\frac{V_{dc}}{2}$ and $-\frac{V_{dc}}{2}$, while the multilevel output has more than two voltage levels, which results in more sinusoidal waveform and thus lower harmonic distortions.

For multilevel converters, the DC-link is split over more than one capacitor, unlike the two-level converter that consists of only a single DC-link capacitor. The use of multiple series DC-link capacitors enables the aggregation of multiple voltages with

the power semiconductor devices for commutation and thus forming high voltage at its output, and simultaneously allows each switching device to withstand a reduced voltage level appearing across each DC-link capacitor, which determines the power semiconductor switches rating.

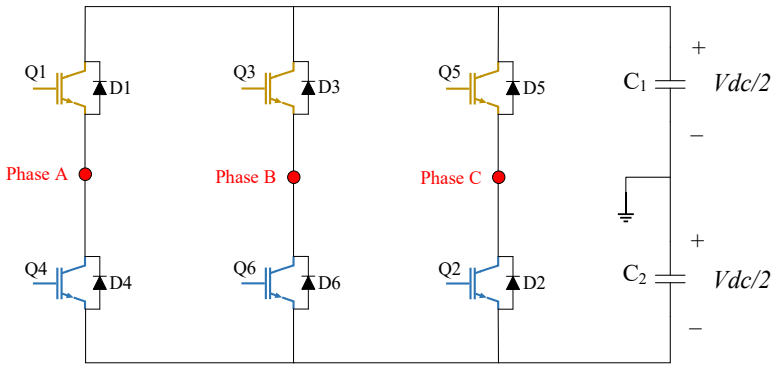

Figure 2-4 Three-phase two-level VSC converter.

The advances in PE switching devices for handling high-power capabilities have made power converters feasible for high-power applications. For high-voltage systems, it is problematic to directly connect a power semiconductor switching unit to a high voltage DC-link because the stray inductance and capacitance present within these switching devices can result in an undesirable voltage overshoot and device damage. Instead, a series connection of multiple switches with lower voltage ratings is beneficial to improve the conversion system reliability [49], [50].

Generally, the benefits of utilising multilevel converters over conventional two-level power converters can be summarised as:

- The output voltage and current of a multilevel converter have reduced distortions in comparison to a two-level converter,
- Because multilevel converters have several output voltages levels, the dv/dt stress is decreased, which in turn lessens the Electromagnetic Compatibility (EMC) problems,
- The switches of multilevel converters can be operated using PWM of the fundamental frequency or higher switching frequencies. However, high switching frequency causes higher switching losses, which decrease the overall efficiency of the conversion system, and

- The multilevel converter makes better utilisation of the DC-link voltage when compared to the two-level converter. This is mainly due to the PWM technique such as the 3rd order harmonic injection for three-level VSC converters. Additionally, for H-Bridge converters, floating capacitors can boost the maximum fundamental voltage [51].

Several research works have been dedicated to multilevel converters in terms of topologies, control, and operation with different proposed modulation schemes. Cascaded H-Bridge (CHB), Neutral Point Clamped (NPC), and Flying Capacitor Clamped (FCC) converters have been appointed as the most promising multilevel topologies for future power systems. A brief overview of the three common multilevel converter topologies is presented next and the best candidate based on the literature survey will be nominated for the MVDC system applications in the power distribution networks.

2. 4. 1. Cascaded H-Bridge (CHB) Multilevel Converter

The Cascaded H-Bridge (CHB) multilevel converter was originally proposed in 1975 [52]. The concept of such a converter is to connect multiple DC-sourced full-bridge units in series to produce a staircase voltage waveform at the AC output. The single-phase structure of the CHB converter is demonstrated in Figure 2-5. The AC output of each H-bridge converter depending on the switches' states can be $+V_{dc}$, $-V_{dc}$, and 0, and by establishing different conduction times between each unit, a staircase voltage waveform of $(N+1)$ levels at the AC output (V_{out}) can be formed with a peak of $(N \times V_{dc})$, where N is the number of H-bridge units used. This is made feasible by the series connection of multiple DC-link capacitors (or DC sources) to the overall AC output terminals with a suitable control scheme over the power switching devices of each unit.

Advantages:

- The levels of the AC output voltage are more than the number of H-bridge units used,
- With a high number of H-bridge units, an AC output with very low harmonic distortions can be achieved even with a lower switching frequency, and

- System modification simplicity due to the series H-bridges modularity.

Disadvantages:

- The main constraint of the CHB converter is that independent DC-link capacitors (or sources) are essential for each H-bridge unit that consequently restricting its application,
- Due to harmonic distortion reductions requirements, a high number of H-bridges is used for a high number of AC output levels, which means more DC-link capacitors and thus a bulky and costly system, and
- The complexity of the control system to operate the CHB converter for maintaining equal voltages across the DC-link capacitors when controlling output active and reactive power components.

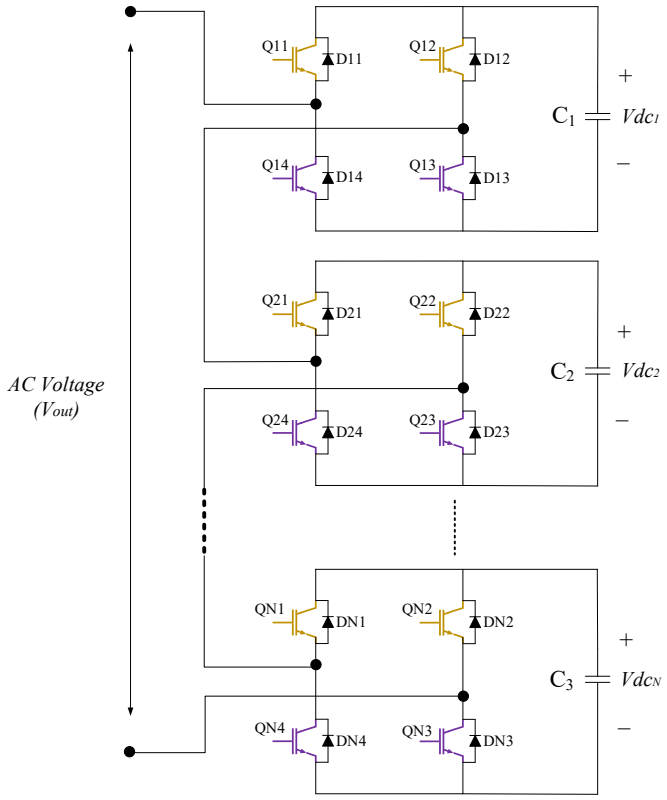

Figure 2-5 Single-phase CHB VSC converter.

2. 4. 2. Neutral Point-Clamped (NPC) Multilevel Converter

The Neutral Point-Clamped (NPC) or diode clamped multilevel converter was first introduced in 1981 with diodes blocking the DC sources to establish a neutral point defining a third voltage level [53]. The three-phase topology of a three-level NPC converter is depicted in Figure 2-6. In this structure, the A, B, and C-phase share a common DC link, which comprises two capacitors connected in series. These capacitors divide the voltage of the DC link via the middle point into three levels ($+\frac{V_{dc}}{2}$, $-\frac{V_{dc}}{2}$ and *0*) that appear at each AC output phase voltage of the converter by a suitable control over the power switching devices. For a single leg, there are two complementary switching devices (Q_{11}, Q_{14}), which are the main switches, and (Q_{21}, Q_{24}), which are the auxiliary switches clamping the output terminal to the neutral point (*N*) through the two clamping diodes.

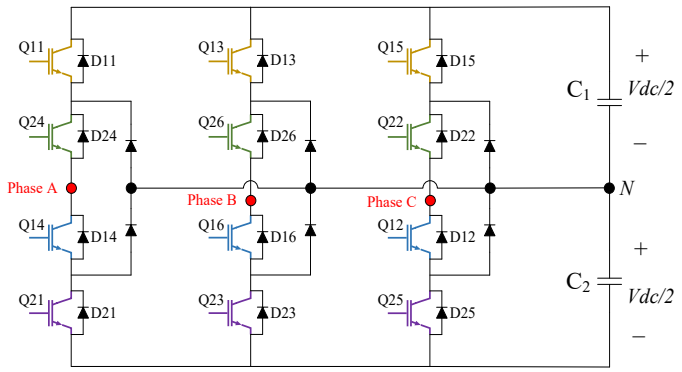

Figure 2-6 Three-phase three-level NPC VSC converter.

Advantages:

- A common DC link is shared by the three-phase terminals, and minimising the number of DC-link capacitors required, system size and cost,
- Since the DC link voltage is divided through the midpoint, lower voltage rating switches can be utilised, and voltage stress issues can be minimised,
- Lower output harmonic distortions and high efficiency with a lower switching frequency, and
- The pre-charging of the DC-link capacitors as a group is possible, thus improving system dynamics.

Disadvantages:

- Increase in the number of diodes required for clamping, and
- Voltages across the DC-link capacitors must be balanced for all operating conditions, thus requiring an effective control system.

2. 4. 3. Flying Capacitor-Clamped (FCC) Multilevel Converter

The Flying Capacitor Clamped (FCC) converter has a similar topology as that of the NPC converter but with clamping capacitors replacing the clamping diodes, proposed in the 1990s [54]. The role of clamping capacitors is to clamp the voltage of the switch to the voltage that appears across the DC link. Consequently, each AC output level in the staircase waveform reflects the voltage across each DC-link capacitor. The three-phase three-level FCC converter is displayed in Figure 2-7. Like the NPC converter, the FCC topology has a common DC link split by the two capacitors connected in series. Each AC output voltage with an appropriate switching of the power semiconductor components has three voltage levels: $+\frac{V_{dc}}{2}$, $-\frac{V_{dc}}{2}$ and *0*. The functionality of the clamping capacitor is to clamp the switching device to a reduced DC voltage appearing across a DC-link capacitor, which is the role of clamping diodes used in NPC converters.

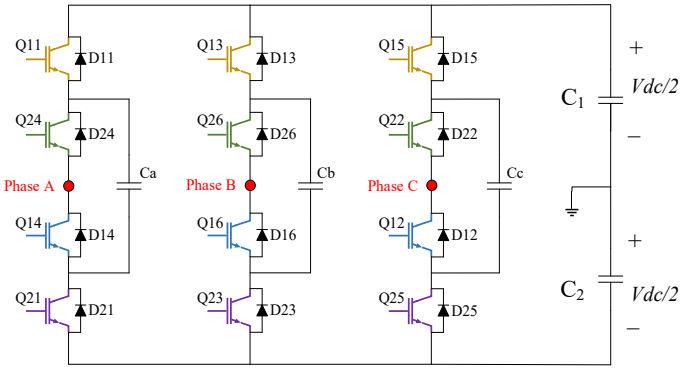

Figure 2-7 Three-phase three-level FCC VSC converter.

Advantages:

- The voltage across capacitors can be balanced by the redundant switching states available, and

- Short duration outages ride through capability due to the increased number of capacitors.

Disadvantages:

- The high cost and bulky size of the system due to many capacitors in comparison to the NPC topology, and
- Requirement of a separate pre-charge circuit and complicated control system for voltage balancing of clamping and DC link capacitors.

The different multilevel converter topologies can also reduce the size and cost of the output filters and improve power conversion efficiency. The three-level NPC and FCC converters, for instance, require half the output inductor for a given switching frequency used in two-level converters and thus reduce the output ripples. Additionally, the switching devices in the three-level converters have half the voltage rating of that used for two-level converters, and therefore reduce the voltage stress across the power converter components and switch losses and improve the system reliability [55].

Comparative studies of switches losses comprising switching and conduction losses and DC-link capacitor losses of most common topologies were conducted in [56], [57]. They concluded that the conventional two-level converter results in significantly higher losses than the CHB and NPC converters even with lower switching frequencies due to the high-voltage rating of switching devices used. For the three-level topologies, switch losses are almost equal for the CHB and NPC converters, assuming equivalent modulation techniques. In terms of DC-link capacitor losses, the CHB and FCC converters have significantly more capacitor losses than conventional two-level and three-level NPC converters, which proved to be equal. However, increased switch losses of two-level converters cannot compensate for their lower DC-link capacitor losses unlike the NPC converter, which proved to be the most efficient and promising topology for high-voltage and high-power applications. In conclusion, as it can be seen from the comparisons made in the literature and detailed discussion presented earlier, the NPC converter topology with the relatively minimised cost and size, lower associated switch and DC-link capacitor losses, and control design simplicity, stands out as the optimal choice for high-voltage and high-power applications such as the MVDC systems.

2. 5. Modelling and Control Development of an MVDC Converter

2. 5. 1. Topology and Specifications

To estimate the harmonic performance of the proposed MVDC converter with the topology shown in Figure 2-8 with parameters provided in [44], [45], [58] and listed in Table 2-1, the first stage is to model the power converters with a detailed representation of the power switching devices. The MVDC converter is based on several three-phase three-level NPC VSCs connected in an especial structure to form a return-grounded bipolar configuration with each DC side connected in series. At both substations, each six power converters are connected to the AC network through a three-phase transformer of 17 MVA having high-voltage star-connected windings and six low-voltage delta-connected windings of 2.1 kV each. Two transformers are used to connect the twelve power conversion units to form the overall topology, while the total DC link of 54 kV is formed by the series connection of each converter DC link of 4.5 kV. The mid-point at each substation is connected to the ground through a grounding resistor, and a DC reactor is commonly used along the DC line to filter out the DC ripples.

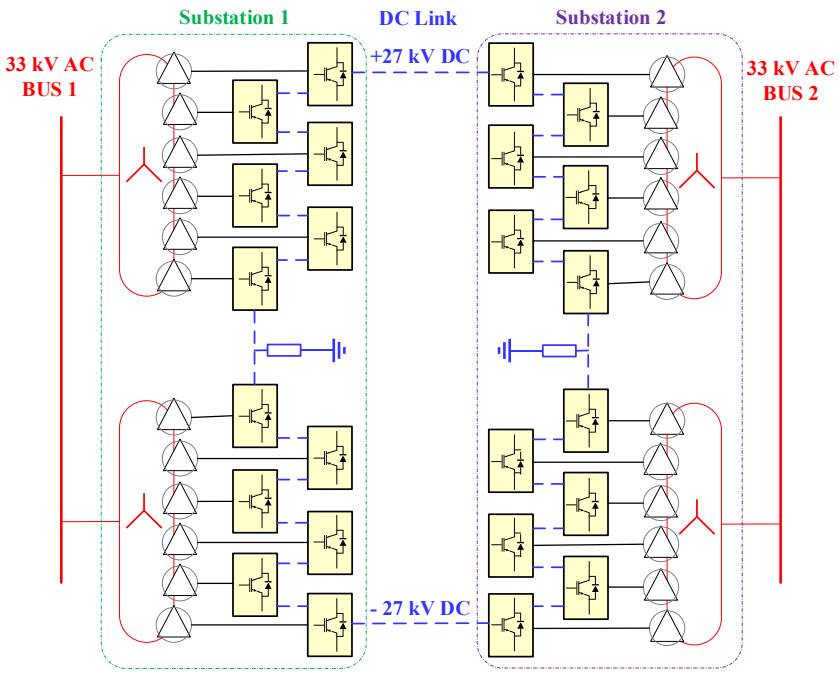

Figure 2-8 Proposed MVDC system topology.

Table 2-1 Specification of the MVDC system.

Parameter	Value
Link Capacity	30 MW
AC Voltage	33 kV - 60Hz
DC Voltage	± 27 kV
Transformer Rating (each)	17 MVA
Transformer Reactance (each)	0.2 p.u.
Switching Frequency (f_{sw})	900 Hz
DC Reactor	6 mH
Grounding Resistor	10 Ω

2. 5. 2. MVDC Converter Control System

The power-flow control scheme, which is widely used to operate a VSC-based conventional back-to-back power conversion system, is adopted for the MVDC system. It has the capability to control the active power between the AC networks, independent control over reactive power at each AC end under normal operating conditions, and fault isolation between the interconnected networks. In this control mode, cascaded or dual closed control loops based on the dq-synchronous rotating frame are used to operate the MVDC converter. The advantages introduced by the current control in the dq-frame are the decoupling between the active and reactive power control and the inherent suppression feature of fault currents [35].

2. 5. 2. 1. Phase-Locked Loop Circuit

The PLL is the key component for the synchronisation of a grid-connected power converter with the grid voltage [59], [60]. The PLL control scheme shown in Figure 2-9 is based on Park's transformation theory, where the q-component of the grid voltage is controlled to zero and a PI controller is used to estimate the corresponding angular frequency (ω), and the phase angle (θ) can then be obtained by an integrator. The PLL developed in Simscape/Simulink is used, which has a similar topology with automatic gain control for the PI controller.

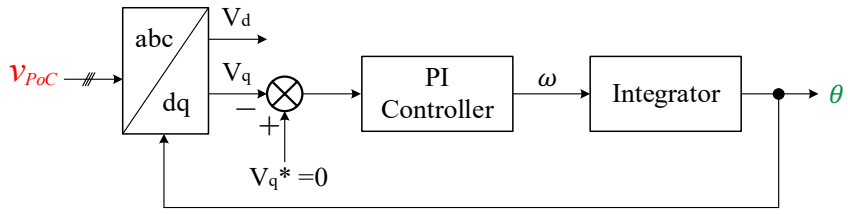

Figure 2-9 Schematic of a simple PLL controller.

2. 5. 2. 2. Inner Control Loop

In [61], to design the inner current control loop, the three-phase three-level NPC converter can be simply modelled by a voltage source behind an impedance representing its equivalent AC filter inductance introduced by the power transformer in this case as shown in Figure 2-10.

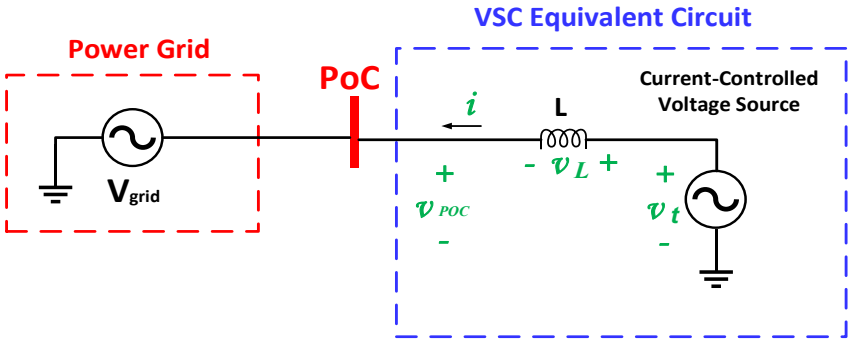

Figure 2-10 Simplified model of a grid-connected VSC converter.

By applying Kirchhoff's voltage law, the following equation in the abc-frame can be obtained.

$$v_L = L\frac{di}{dt} = v_t - v_{POC} \tag{2.1}$$

Applying Park's transformation with the cross-coupling due to the inductance behaviour considered yields:

$$v_{L_d} = L\frac{di_d}{dt} = +L\omega\, i_q + v_{t_d} - v_{POC_d} \tag{2.2}$$

$$v_{L_q} = L\frac{di_q}{dt} = -L\omega\, i_d + v_{t_q} - v_{POC_q} \tag{2.3}$$

Transforming the time domain equations to the frequency domain by applying Laplace transform yields:

$$I_d\, L\, s = +L\omega\, I_q + V_{t_d} - V_{POC_d} \tag{2.4}$$

$$I_q\, L\, s = -L\omega\, I_d + V_{t_q} - V_{POC_q} \tag{2.5}$$

Based on the Laplace equations, the grid filter model representing a reduced-order model of the power converter can be developed as in Figure 2-11.

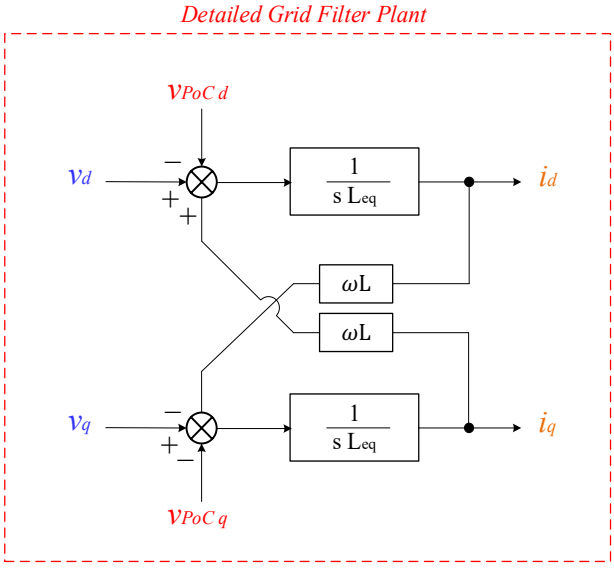

Figure 2-11 Equivalent model of a grid-connected VSC converter in the dq-frame.

Now, the control circuit regulating the output current of the VSC converter modelled in the dq-frame can be drawn as shown in Figure 2-12. It should be noticed that the grid voltage and cross-coupling components in the control circuit have opposite signs to that shown in the detailed grid filter plant. This is to compensate and cancel out their impact on the dynamic response of the system under the control.

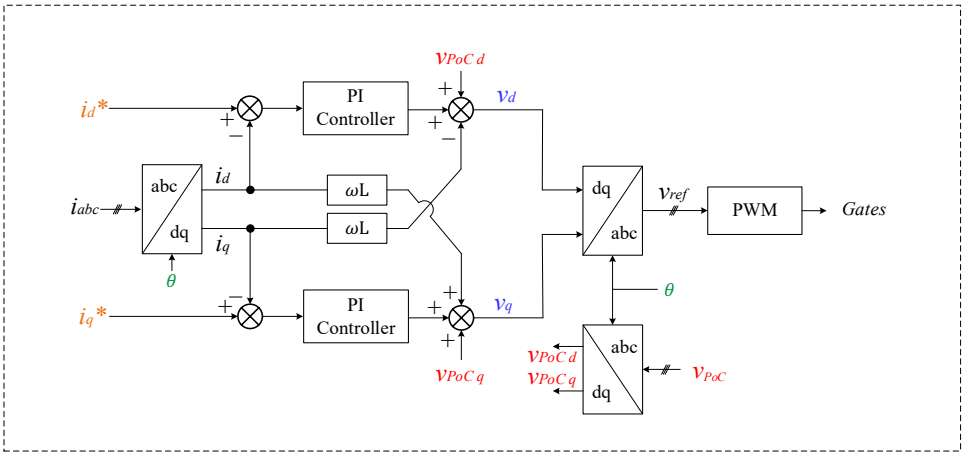

Figure 2-12 Current control model of a grid-connected VSC converter in the dq-frame.

The inner current control circuit receives the dq-current commands from the outer loop and provides the proper reference signals for the PWM circuit. The difference between the reference and measured dq-current components are processed through a PI controller, and the reference signals (v_{ref}) are obtained after the inverse Park's transformation. The compensations of the feedforward voltage and cross-coupling current due to the dq transformation are commonly employed to improve the transients of the conversion system [61], [62]. The PWM then generates the train pulses for the switching devices such as Insulated Gate Bipolar Transistors (IGBTs).

2. 5. 2. 3. Outer Control Loop

The implementation of the outer control loop shown in Figure 2-13 is straightforward. It is used to provide the reference dq-current components through PI controllers for the inner loop shown in Figure 2-12. The structure of the inner loop control is common for each power converter in each substation, while the outer loop differs for each converter based on where it is placed. For the MVDC system, converters at Substation 1 are operated in P-Q control mode, while the V_{dc}-Q control scheme is used for those at Substation 2. As the names imply, the P-Q controls the active and reactive power to the predefined set points, while the V_{dc}-Q maintains the DC link constant for a stable active power flow and controls the reactive power at its AC end. Dynamic current limiters are usually incorporated to

detect and protect the system from overcurrent during abnormal operating conditions [35], [61].

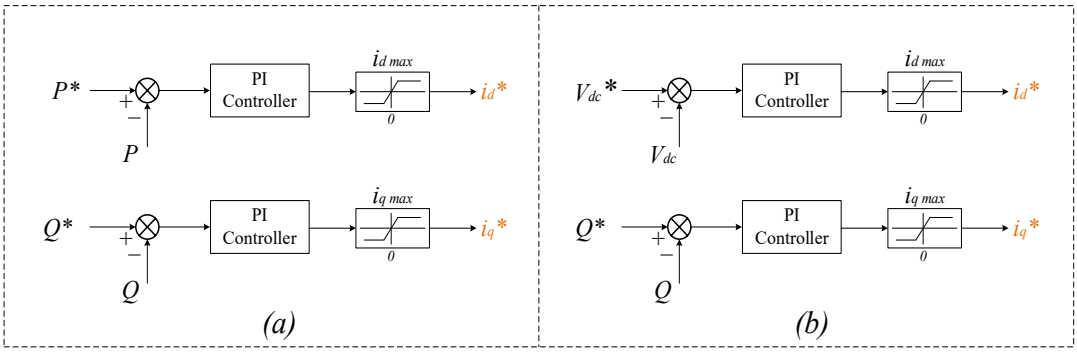

Figure 2-13 Outer control loop model of a grid-connected VSC converter in the dq-frame, (a) P-Q control mode, (b) V_{dc}-Q control mode.

2. 5. 3. PI Controller Parameters Design

There are several available methods for the control loop design. The methods of robust control design including high-order control systems cannot be simply realised in real power conversion systems [61]. Nevertheless, the easily implemented Loop-shaping method yields satisfactory control performance [62], and thus it is used for the MVDC converter inner current loop to tune the PI controllers' parameters, whereas outer loop PI controllers are tuned in this work by trial-and-error approach to achieving the desired performance. When the power network is assumed to be balanced, and the steady-state operation is of concern, the voltage disturbances and cross-coupling components can be overlooked due to their significance in transients only. Besides, the DC link voltage can be assumed constant with no disturbances since its response time is much slower than the inner current loop [61]. Additionally, when the system operates at the unity power factor, the d- and q-component models are identical to represent the overall system response, and hence the converter model can be further simplified as shown in Figure 2-14.

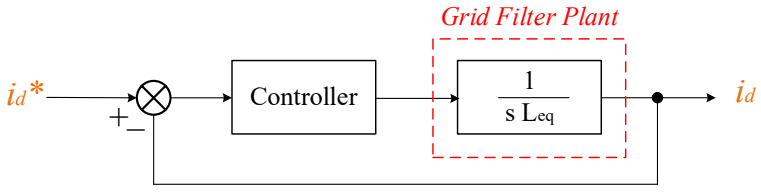

Figure 2-14 Overall structure of the simplified current control loop.

For the given performance requirements, the process starts with the open-loop Bode plot of the plant model of the system under the control, then an integrator is placed with a Left-Hand Zero (LHZ) to achieve the required open-loop phase margin. Finally, a factor is imposed to modify the crossover frequency to meet the required performance criteria. To accomplish a fast response current control loop, the PI controller design objective is to adjust the current control bandwidth between 1/20 and 1/10 times the switching frequency (f_{sw}), while sufficient close-loop stability can be assured by regulating the phase margin normally higher than 45 degrees at the crossover frequency with a slope of -20 dB/dec [61], [62].

For the MVDC system, the transformer leakage reactance is assumed symmetric for each winding connecting each power conversion unit, and it is adopted in the grid filter plant for the control design. At 2.1 kV and 2.9 MVA, the low voltage equivalent inductor (L_{eq}) is approximately 2.15 mH. Figure 2-15 to Figure 2-18 illustrate the process of the Loop-shaping technique, and Figure 2-19 shows the resulting open-loop Bode plot of each stage of the current control design.

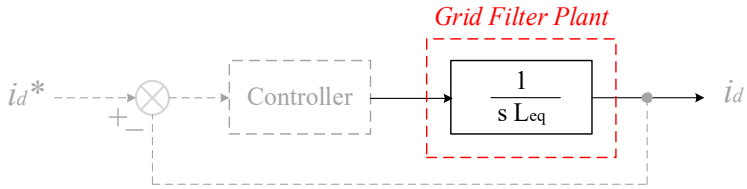

Figure 2-15 Stage-1 for the Loop-shape design of the current control loop.

Firstly, an integrator ($\frac{K_g}{s}$) is applied to control the plant instead of a PI-type controller. From the Bode plot, the system shown in Figure 2-16 is constantly unstable with a continuous zero phase margin irrespective of the controller gain (K_g), which can only change the crossover frequency. Therefore, with the integral controller only, the phase margin cannot be modified, and an LHZ requires to be added as shown in Figure 2-17.

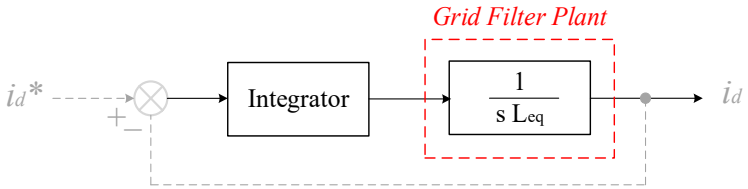

Figure 2-16 Stage-2 for the Loop-shape design of the current control loop.

System stability can be achieved by adding the LHZ of a low frequency in the controller transfer function that modifies the system phase margin. In the case of low switching frequency, the crossover frequency is planned at 90 Hz, (i.e., $\frac{1}{10} \times f_{sw}$), for the inner control loop, and therefore the LHZ frequency (f_z) is selected as 45 degrees, which is adequately below the planned crossover frequency.

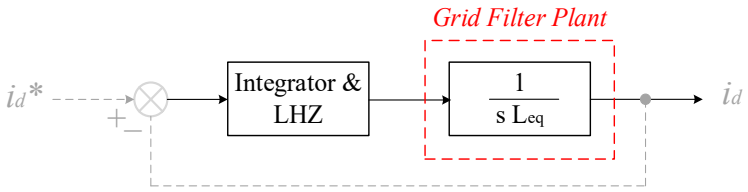

Figure 2-17 Stage-3 for the Loop-shape design of the current control loop.

From the Bode plot, the system now has a phase margin of 63.4 degrees that ensures the system stability, but the crossover frequency needs to be adjusted. The integral controller gain (K_g), which influences only the control loop magnitude, now acts to modify the crossover frequency to 90 Hz. The gain computation depends on how much increment the system requires to cross the 0 dB at 90 degrees. As a result, the gain is computed as $10^{56.7/20}$ for 56.7 dB as illustrated in the Bode plot. The final model of the controller is given as:

$$Integrator\ \&\ LHZ\ = \frac{K_g}{s}\left(\frac{s}{w_z}+1\right) = \frac{K_g}{s}\left(\frac{s}{2\,\pi\,f_z}+1\right) \qquad (2.6)$$

The standard PI controller shown in Figure 2-18 is preferred for its easy implementation and modelling. Moreover, a discrete form of it can be easily implemented in a simulation program like Simulink/MATLAB. The proportional

gain (K_p=1.132) and integral gain (K_i=320) are simply calculated from the controller model developed from the Loop-shaping technique as:

$$PI\ controller = \frac{K_g}{s}\left(\frac{s}{2\,\pi\,f_z}+1\right) = \frac{K_g}{2\,\pi\,f_z}+\frac{K_g}{s} = K_p+\frac{K_i}{s} \qquad (2.7)$$

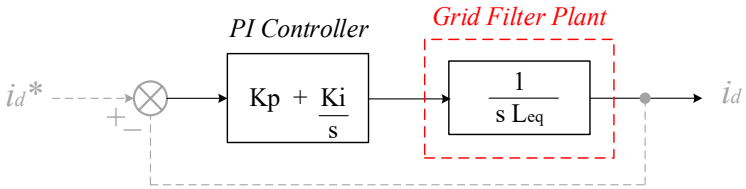

Figure 2-18 Stage-4 for the Loop-shape design of the current control loop.

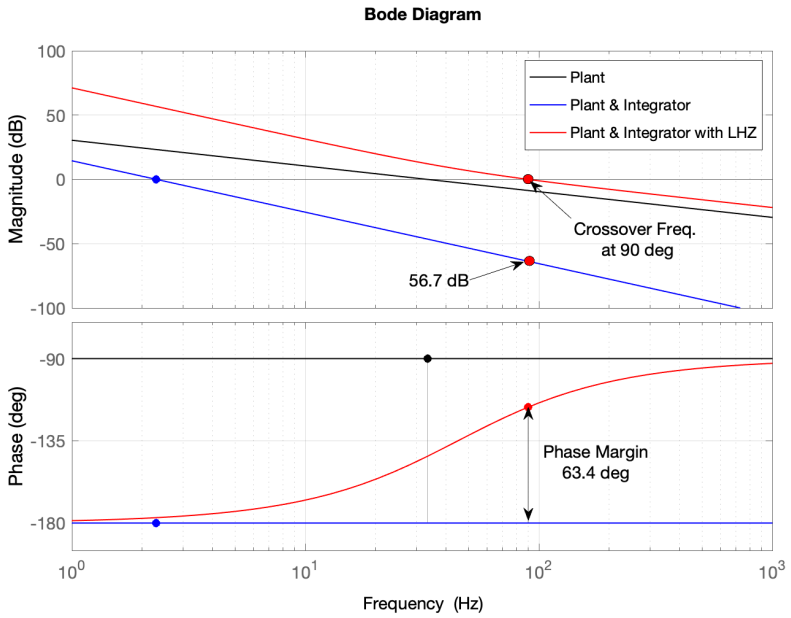

Figure 2-19 Bode plots of the current loop control design stages in terms of amplitude and phase characteristics.

2. 6. Pulse Width Modulation Techniques

Among the different modulation techniques, the SPWM approach, which is based on a reference modulation signal compared with a high-frequency carrier signal, has a superior performance during normal and faulty operation conditions with different power flow profiles and less complicated control for balancing the DC-

link capacitor voltage in comparison with Space Vector Modulation technique [63]. For the three-level NPC converter topology, the controlled sinusoidal reference signal of the fundamental frequency is compared with two triangular signals determining the switching frequency at which the switching devices operate as depicted for a single leg in Figure 2-20. To generate switching pulses for the three-phase converters, a 120-degree phase shift must be introduced between the three reference modulation signals while employing the same high frequency for the carrier [49].

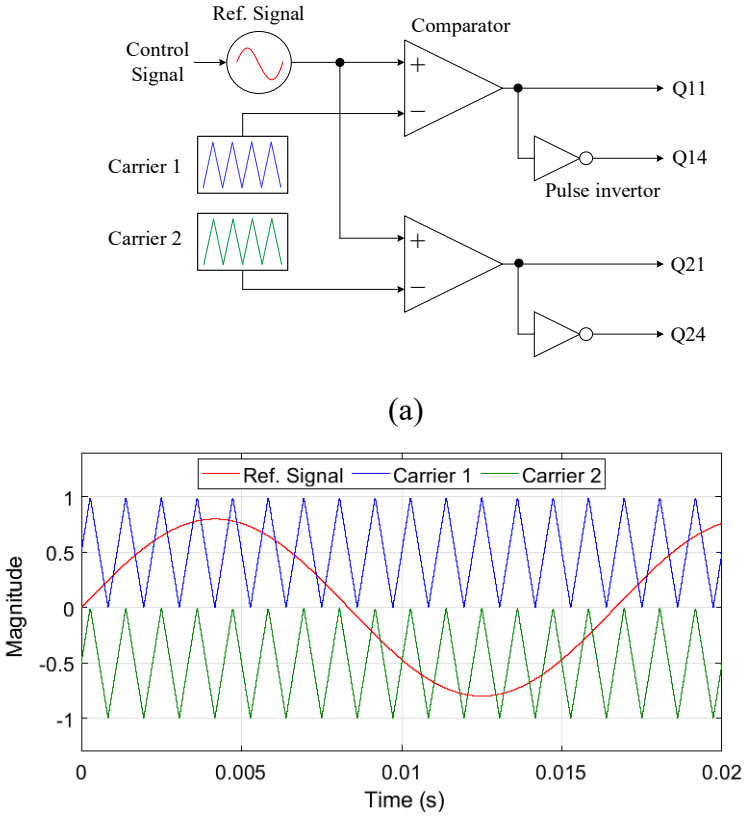

Figure 2-20 SPWM technique for an NPC converter (one leg is shown for illustration), (a) the technique circuit, (b) plot of the input signals.

The reference sinusoidal signal frequency decides the converter output frequency, while the carrier signals frequency defines the switching frequency, which should be carefully selected for a given fundamental frequency to avoid asymmetry between the positive and negative half cycles of the output voltage waveform as demonstrated in Figure 2-21. The frequency modulation index (m_f), which is the

ratio of the switching frequency to the fundamental frequency, should be an odd integer and divisible by three [14]. Figure 2-22 shows the resultant voltage spectra of different illustrative pulse numbers. It is observed that when the pulse number is a multiple of an odd integer and divisible by 3 as in the case of $m_f = 39$, the triplen or zero-sequence harmonic orders are absent. However, when the pulse number is only an odd integer but not divisible by 3 ($m_f = 37$), the triplen harmonics (33rd, 39th, 45th, 69th, etc.) appear reflecting an asymmetrical output voltage waveform between the half cycles, which affect the operation of power systems components such as heating the electric motors and transformers and result in high current flowing through neutral conductors [13], [64]. Therefore, the lower switching frequency of 900 Hz resulting in 15 pulses that is an odd integer and divisible by 3 is chosen for the MVDC converter at the fundamental frequency of 60 Hz.

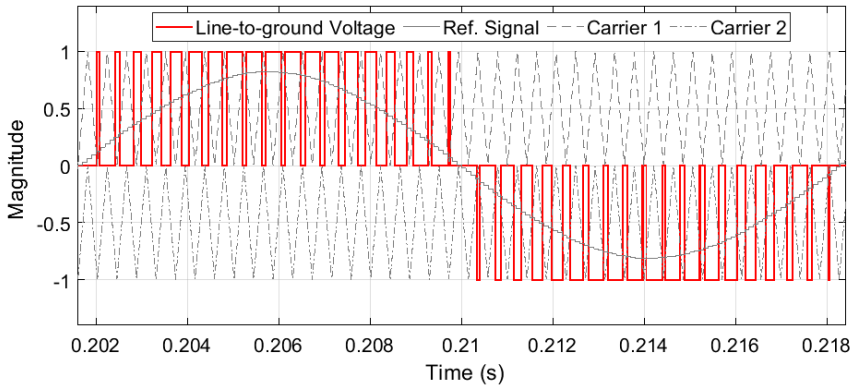

Figure 2-21 SPWM for a three-level NPC converter with a pulse number of 39.

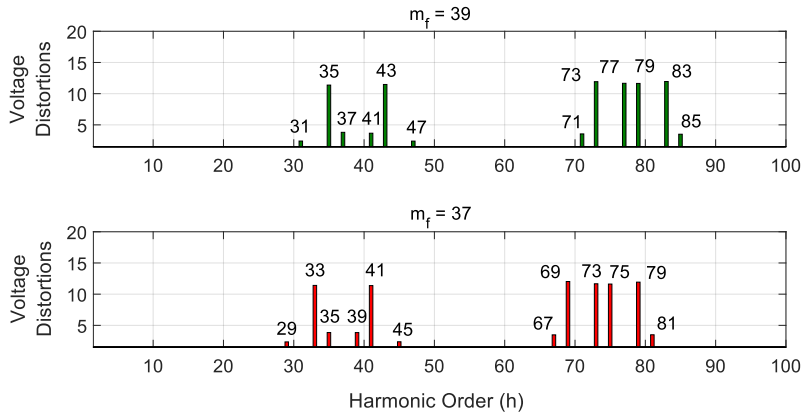

Figure 2-22 Voltage spectra (in percentage) of a three-level NPC converter operated with SPWM for two frequency-modulation indices.

2. 6. 1. Interleaved SPWM Technique

The most commercially available grid-connected converters are usually designed with an LCL passive filter [59], [61]. For high-power applications, a lower switching frequency is employed to reduce switch losses and therefore disproportionately larger passive filter components are required for harmonic currents reduction. Besides the evident burden of the filter size and cost, large filter components have further disadvantages on the power system. Firstly, utilising a large inductor influences the system's dynamic response that can be critical for fault ride-through capability with the presence of grid disturbances such as voltage dips and swells. A large capacitance implies high currents drawn from the network, and this requires a more complicated control system to compensate for the power factor at the converter output [65]. The large capacitor additionally provides a low impedance path for harmonic currents developed from the grid background voltage harmonics that eventually raise the converter output THD. Moreover, the grid-side inductors adding extra cost and size are occasionally used in two-level converters to prevent the injection of high-frequency current components into the power grid. This additional inductor is undesirable when the converter is connected to a grid or operated autonomously and supplies a nonlinear load as it significantly increases the voltage distortions at the connection point. This is because of the harmonic impedance of the inductance that increases linearly with the frequency.

The interleaved topology first received attention in a wide range of DC/DC power conversion applications such as electric and hybrid Electric Vehicles (EV) [66]–[68], communication power suppliers [69], and solar PV systems [70], [71]. The main reason for adopting this topology is to improve the system's power density, dynamic performance, and efficiency. The interleaved topology has also been applied to power inverters [72]–[74] and rectifiers [75], [76]. Interleaved configurations are formed by connecting an N power converter in parallel and imposing an equal phase shift between their switching instants over the switching period. There are several benefits of the interleaved configuration over the conventional topology for grid-connected systems. By establishing the phase shift between the switching pulses of the parallel converters, the overall current distortions are N times lower, and its apparent switching frequency is N times larger

than that of a single power converter. Therefore, the switch losses of each power converter can be significantly reduced since a lower switching frequency is used, and the need for the large LCL passive filter to reduce the output harmonic currents is compromised by a smaller filtering inductance, which is usually provided by the interfacing power transformer leakage inductance. The decrease in switch losses reduces the cooling system size and improves the overall efficiency [59].

There are several publications discussing the benefits and optimal design of the filtering system of interleaved power converters. The authors in [57], [72] proposed an active power filter configured in interleaved topology to improve power capability and minimise the AC inductor size. It showed that the resulting switching harmonic current is reduced due to ripple cancellation by the interleaving effect. A design method based on the frequency domain analysis was developed in [73] to decrease the AC inductor's size through a proper selection of the phase shift between the interleaved converters. It demonstrated the effectiveness of the optimised interleaving angle on the AC harmonic currents for a given PWM strategy with various modulation indices.

Low power interleaved DC/DC converters were proposed in [77]. The principal objective was to reduce the filters inductors so that they can be incorporated into the printed circuit board by manufacturers. In [78], an optimization of the number of DC/DC interleaved converters was performed to reduce the overall converter losses involving inductor, capacitor, and switching devices losses. Moreover, the influence of the number of interleaved DC/DC converters on the filter inductors and capacitors size was discussed in [79]. However, unlike the published work with a fixed switching frequency, an optimization-based design of a DC/DC power converter was conducted in [80] to reduce its overall size with different switching frequencies, the number of interleaving, and operating modes.

2. 6. 1. 1. Interleaved SPWM application in the MVDC Converter

The detailed model of the MVDC converter developed in this work has a special topology comprising multiple three-phase three-level VSC-based NPC converters connected in a cascaded configuration. Since a low switching frequency is adopted in the MVDC converter for switch losses reduction, an evenly interleaved SPWM

configuration is introduced for the converters within each substation to further minimise the distorted currents in the high-voltage winding and to reduce their impact on each power transformer. The low switching frequency will significantly contribute to lowering switching losses, which is undesirable for high power applications. Figure 2-23 depicts the interleaved SPWM for six MVDC converters, only the upper carriers are shown for illustration. The detailed mathematical models of the interleaved SPWM introduced for the MVDC converter model developed in this work are provided in [74].

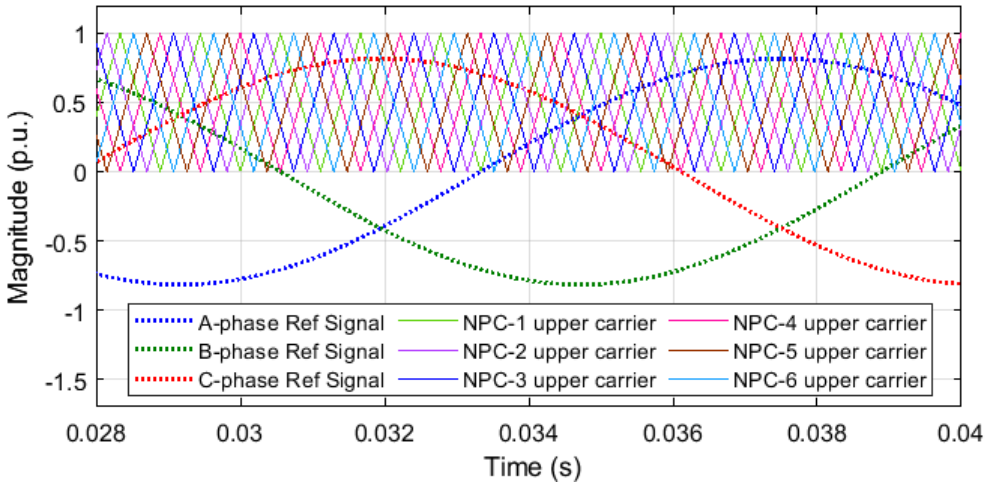

Figure 2-23 Interleaved SPWM generation for cascaded three-level NPC converter (only upper carriers of six NPC converters are shown for illustration).

2. 7. Performance Analysis of the MVDC System

2. 7. 1. Fundamental Frequency Performance

The performance of the MVDC system is analysed under different operating conditions employing infinite AC power sources at both ends. This system is modelled in the Simulink/MATLAB simulation environment using the parameters of the MVDC system shown in Table 2-1. The detailed model incorporating the switching behaviour of the switch devices is commonly adopted for investigating both transients and the steady-state performance of the system. The performance of the control scheme for the power flow control is also examined through this model by assuming that Substation 1 is operated in P-Q control mode, while Substation 2 is operated in V_{dc}-Q control mode.

The active power reference was set so that the MVDC system delivers 15 MW (1.25 MW per converter) to BUS 2 at 0.15 seconds and 30 MW (2.5 MW per converter) to BUS 1 at 0.3 seconds. However, the reactive power is set independently for each AC side. Substation 1 supplies 12 MVAr (1 MVAr per converter) between 0.2 and 0.45 seconds and absorbs the same amount of reactive power afterwards. Substation 2 provides 12 MVAr (1 MVAr per converter) after 0.18 seconds, while the DC link voltage is maintained constant at 4.5 kV per converter resulting in 54 kV across the total DC link.

Figure 2-24 shows the system voltage and current traces and the instantaneous active and reactive power at both 33 kV buses. The control system accurately and rapidly tracks the reference set points at the steady-state condition with no significant overshoots during transients. The dq-frame control scheme offering decoupled control over the active and reactive power is also simulated. The results imply that the MVDC system has the capability to provide instant and retentive power flow with dynamic and flexible control over the active and reactive power flow at normal operating conditions. However, the high step change (including a reverse power flow) in the active power reference (at 0.3 seconds) results in a noticeable variation in the reactive power measurement at both AC ends. This is because of the inherent coupling effect between the active and reactive power in power systems affecting the DC link profile.

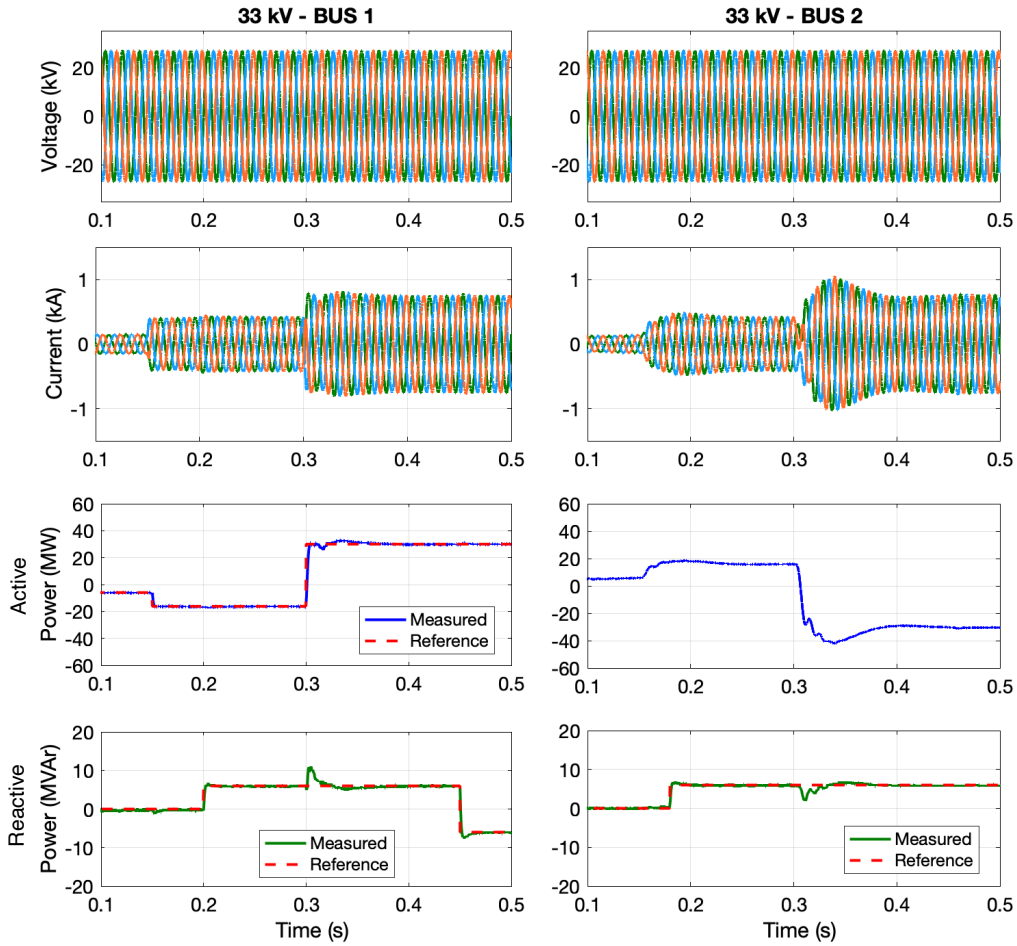

Figure 2-24 The power-flow control response of the MVDC system subjected to step changes in active and reactive power setpoints: voltage, current, active power, and reactive power, (BUS-1 on left, BUS-2 on right).

The MVDC system DC voltage is depicted in Figure 2-25. It remained constant over the steady-state duration with some transitory variations following the step changes in the reference active power that causes an instantaneous imbalance of power transferred throughout the DC link. These variations are undesirable and can be attenuated by adopting larger DC-link capacitors. However, this can also be improved by slowing down the DC voltage control loop response instead of enlarging the DC link capacitors. The DC voltage variation caused by a step change of 15 MW at 0.15 seconds is much smaller than that caused by the larger step change of 30 MW at 0.3 seconds. Yet, when the active power step changes are reduced or gradually changed, which is the case in real power systems operations, the variation in the DC voltage can then be reduced.

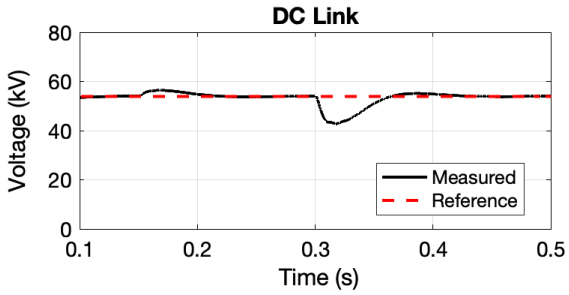

Figure 2-25 DC link voltage variations due to the different active and reactive power setpoints.

2. 7. 2. Harmonic Performance

The detailed model of the MVDC converter including the switching behaviour of switching devices helps accurately investigate the harmonic performance of such a system. To eliminate the impact of the DC voltage control system and the variations due to the large power being exchanged, a constant DC voltage source was used for maintaining the total DC link voltage at the rated setpoint of 54 kV. The output AC voltage of each NPC-VSC system at Substation 1 is depicted in Figure 2-26, only six power converters' output voltage traces are shown for illustration. The converter voltages are applied directly to the secondary windings. The converters produce voltage pulses that are phase-shifted by 1/6 of the switching period. Thus, the transformer secondary currents will contain PWM switching ripple which circulates mostly between transformer secondary windings. Due to phase shifts in the secondary current, the current at the primary terminals will have relatively low distortions because of the switching ripple/cross current cancellation.

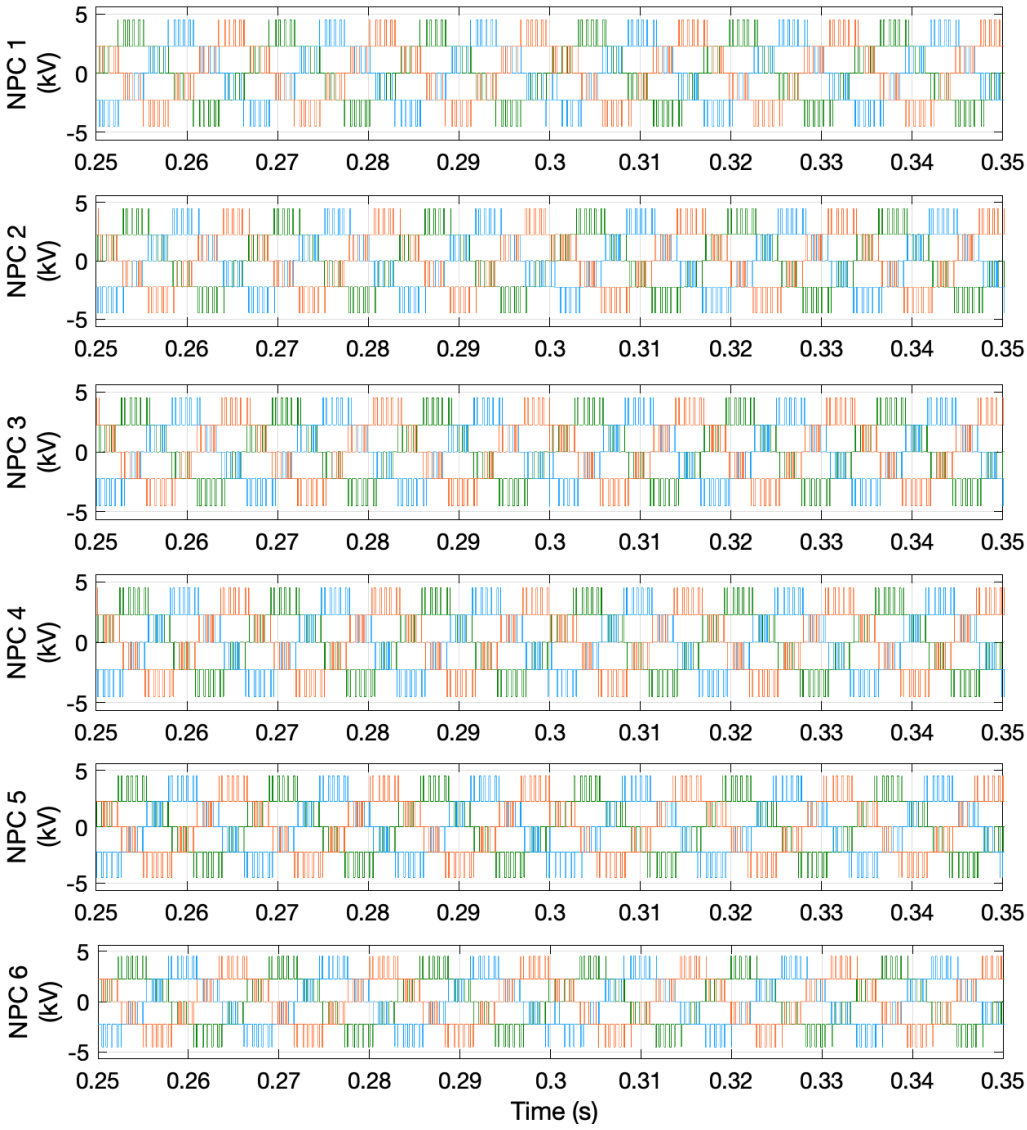

Figure 2-26 Output voltage of the NPC converters (six NPCs' outputs are shown for illustration).

The LV winding current waveforms are illustrated in Figure 2-27. The three-phase NPC converters operate at a unity power factor and inject a total of 15 MW till 0.3 seconds and then supply a 30 MW afterwards to the 33 kV power grid. From the winding current waveforms, it can be observed that the current ripples in different windings could be different due to interleaved SPWM method excluding the asymmetry of the coupling/impedances between LV windings.

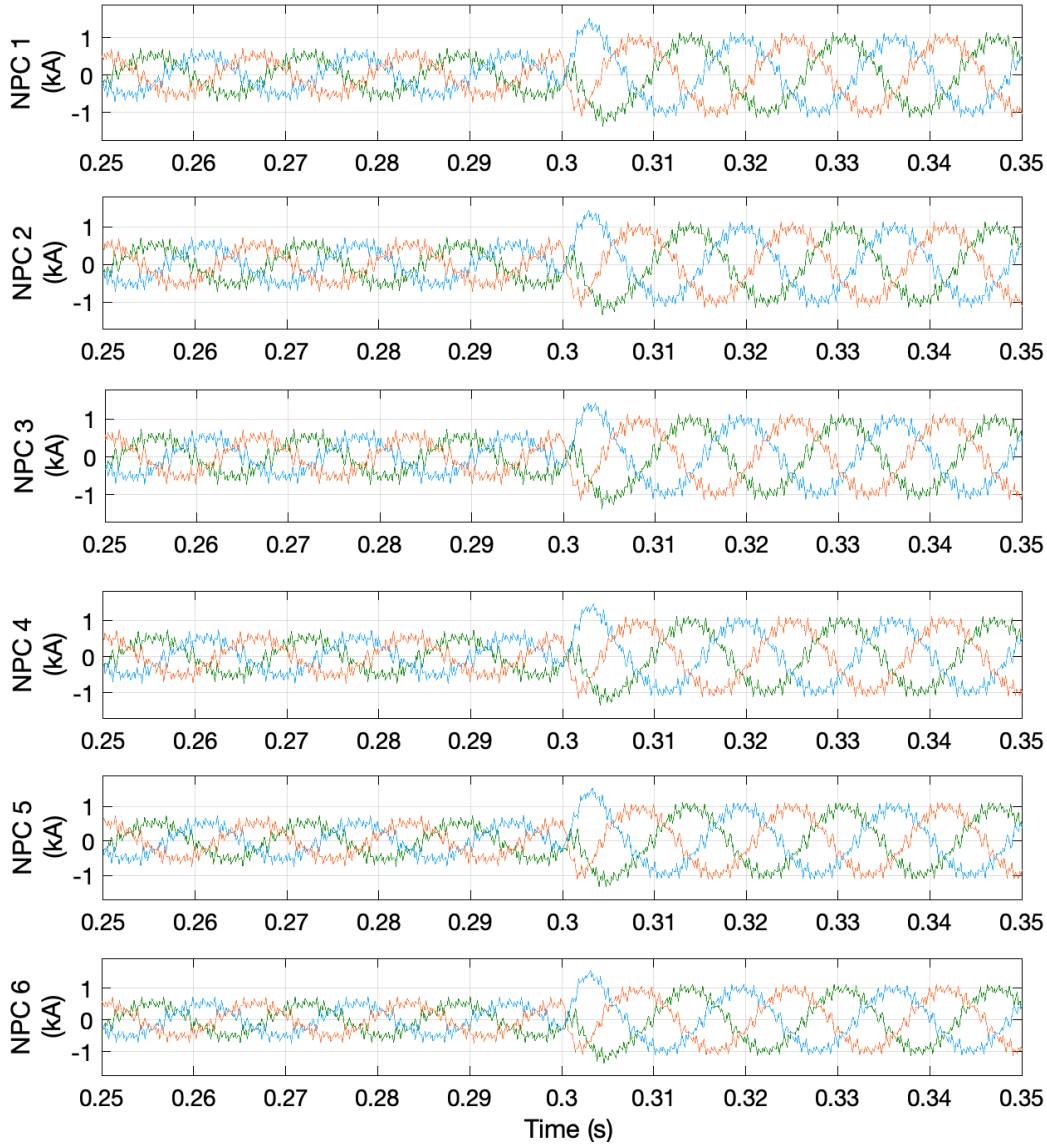

Figure 2-27 The output current of the NPC converters for the two operating conditions (six NPCs' outputs are shown for illustration).

The FFT solution is adopted for specifying the LV current harmonic content, and the spectra for the two different operating conditions are superimposed in Figure 2-28. It can be noticed that the major distortions in the LV winding currents occur in the first switching frequency band around 900Hz (15th harmonic order), which is attributed to the low pulse number of the PWM. The regular sampled PWM has resulted in negligible non-characteristic harmonic components. The LV winding current THD is about 30% and 17% for half and full rated operating power of the MVDC system, respectively.

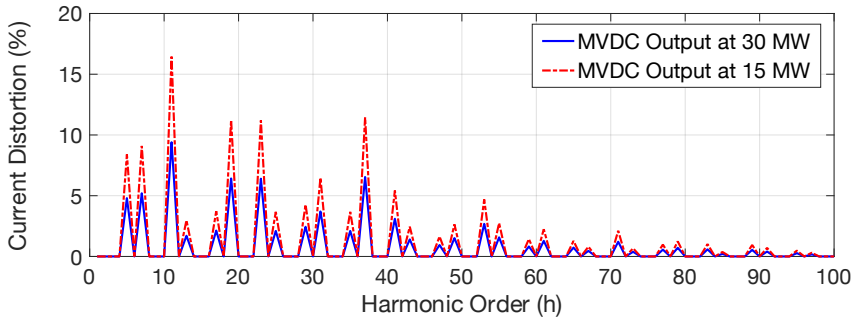

Figure 2-28 Output current spectra of an NPC converter for the two operating conditions.

The MVDC converter output current is composed of fundamental current and harmonic components resulting from the switching behaviour of the NPC-VSC power converters. The trace of the total output current is shown in Figure 2-29, and the current spectra for the two different operating conditions are depicted in Figure 2-30. It is observed that the output current is dominated only by low order harmonic components. However, the switching frequency harmonics have been significantly compensated by the mutual cancellation of the cross-currents flowing in LV windings (due to the interleaved SPWM). The introduction of the interleaved SPWM scheme has consequently reduced the high-order harmonic components of the total output current.

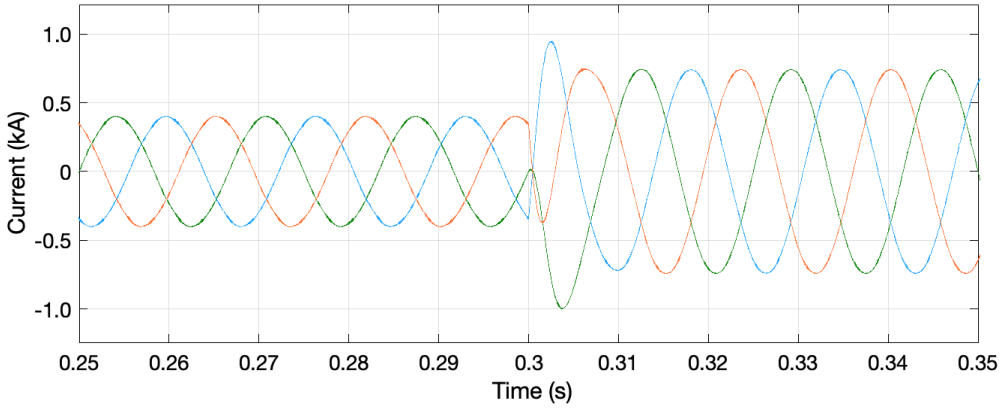

Figure 2-29 The total output current of the MVDC system for the two operating conditions.

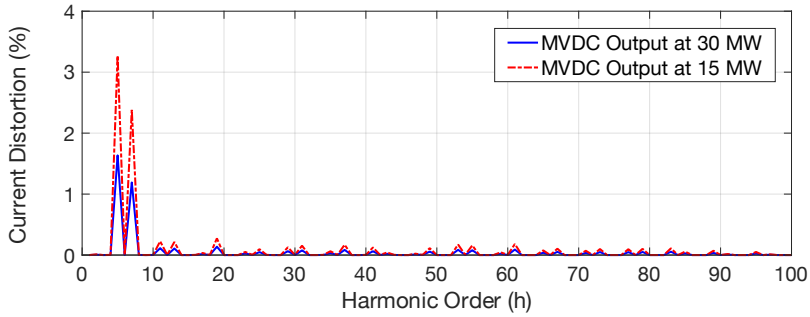

Figure 2-30 Total output current spectra of the MVDC system for the two operating conditions.

The harmonic performance is analysed using the FFT solution. About 17% THD at low-voltage windings current and about 2% THD at high-voltage windings current can be experienced at full-load operation. Although the MVDC system is rated at 30 MW, the transmitted power can vary based on time-varying power demand. Therefore, the harmonic performance is affected by the MVDC converter operating points. For instance, 4% THD can develop when 15 MW of power is exchanged between the AC grids. It is observable that the 5th and 7th harmonic orders are dominant among the low-order harmonic components. These low-order harmonics can be amplified when PFC capacitor banks develop a lower resonant frequency. However, the high-order harmonics, even with lower magnitudes, can interact with power system impedance, and thus can result in high-order voltage distortions. Therefore, a broad harmonic performance analysis of the MVDC system's harmonics in a power network must be investigated against the standard limits.

To validate the proposed MVDC converter model and highlight the effect of the interleaved SPWM technique proposed, the harmonic emission of the MVDC converter modelled in this work is compared with that of the detailed MVDC converter model developed in [44]. Figure 2-31 shows the output current spectra of the developed and established MVDC converter models. It can be observed that the output current of the MVDC converter model with the interleaved SPWM has a maximum THD of 2% in comparison with the established model that has up to 4% THD at rated power. For the established model, the switching frequency sideband harmonic components (i.e., 15th, 30th, 45th) are dominant, while the developed

model with the effect of the interleaved SPWM has a significantly eliminated even-order harmonic components, which can adversely affect the operation of power transformers and motors operation [64].

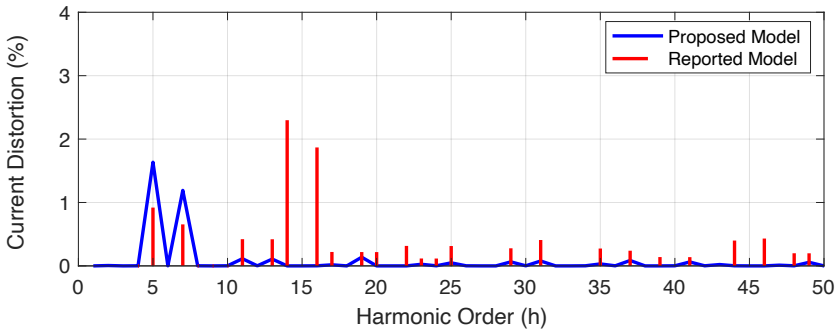

Figure 2-31 Comparison between developed and established MVDC converters' total output current spectra.

2. 8. Summary

In this chapter, the different configurations of MVDC systems were reviewed, and different multilevel power converter topologies were compared to nominate the best candidate for such high-power technologies. A detailed model of the MVDC system based on the three-phase three-level NPC power converters with a suitable power flow control scheme was developed, and the Loop-shaping technique was implemented to achieve the desired control loop performance. The control performance was investigated for different operating set points, the interleaved SPWM technique for such a low switching frequency-based system was developed to reduce the harmonic emissions at the converter level, and the harmonic performance for different operating conditions was analysed. It was observed that the output current of the MVDC converter model developed with the interleaved SPWM has a maximum THD of 2% in comparison with the established model, and the interleaved SPWM has significantly eliminated the even-order harmonic components, which can affect the operation of power transformers and motors.

Chapter 3. MVDC Converter Harmonic Analysis in Distribution Networks

The main goal of this chapter is to develop a harmonic model of a real data-based medium voltage power distribution network to investigate the Medium Voltage Direct Current (MVDC) converter's harmonic propagations and penetration through the AC network. A critical review of the reported harmonic models of the power system components is conducted to determine the most reliable models for accurate power harmonic analysis studies. Harmonic propagations, penetrations, and resonances of a real power system using the frequency domain approach are then analysed.

3. 1. Review of Harmonic Modelling Approaches of the Key Power System Components

For the frequency domain power harmonic solution, the different available modelling techniques of power system components would significantly influence the harmonic performance of a power system under the study. Therefore, a review of the reported harmonic models of the power system components in the literature is introduced, and a comprehensive comparative study is conducted to highlight the effects of different models on harmonic flow analysis studies.

3. 1. 1. Overhead Lines

The overhead lines and underground cable impedances are crucial for the power network harmonic flow analysis. The detailed harmonic modelling of overhead lines is well presented in the literature, and the characteristics of overhead lines beyond the power frequency with the length, frequency dependency and imbalance effects should be considered [13], [17]. Conventionally, an overhead line encompasses a series impedance (resistance and reactance) and a shunt element (susceptance), which are distributed over the entire circuit length and influenced by the operating frequency. These electrical quantities can be developed from the circuit geometry and the conductor specifications for each harmonic frequency. The circuit's length has a significant impact on these components at higher frequencies,

hence long-line impacts must be involved when evaluating harmonic distortions [13]. This necessitates the use of several lumped or equivalent-π models derived from wave propagation calculations based on the line length.

In most harmonic analysis studies, the frequency dependency effect of the parameters of the line, which is calculated at power frequency and represented by a nominal-π or equivalent-π model, tended to be overlooked due to the lack of accurate information and computing power [81]. To decrease computing power requirements in cases where zero-sequence components and damping at resonant points are not vital for harmonic penetrations, a simplification could be made by ignoring frequency dependency and simply assembling the impedance and admittance matrices over the range of frequencies of interest [17]. Later studies, such as in [82], recognised the significance of comprising the frequency dependency in the models by means of hyperbolic functions to improve the representation of long-line effects in transmission lines. Nowadays, computing power is seldom an issue and can capture both the frequency dependency and the distributed nature of the electric quantities for the most accurate harmonic analysis. The frequency dependency in the distribution networks could be compromised by the relatively high R/X ratio of the overhead lines compared to transmission lines and the highly resistive aggregated loads seen in the medium voltage level, which provide a significant damping effect at resonant points if they occur [13]. Therefore, a simple harmonic model of short overhead lines can be approximated by a nominal-π model as shown in Figure 3-1, where the parasitic resistance of the capacitive elements is assumed negligible.

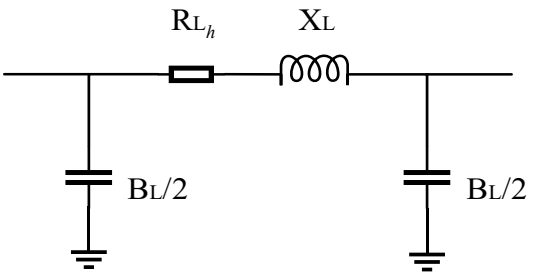

Figure 3-1 Overhead line representation.

When the skin effect that will introduce additional marginal damping at resonances is considered, the resistance part can now be associated with a factor ($\sqrt{h}$) to account for the frequency dependency effect [13], [17], [21], and the model can be developed as:

$$Z_{L_h} = \sqrt{h}\, R_{L_h} + jhX_L \tag{3.1}$$

$$Y_{L_h} = jh\frac{B_L}{2} \tag{3.2}$$

Where X_L , R_{L_h} and B_L are the line reactance, resistance and susceptance calculated at the power frequency. The nominal-π model based on lumped parameter approximation is acceptable for short line sections. However, for a long overhead line of more than 80 km, a distributed parameters-based (equivalent-π) or cascaded nominal-π model is required as voltage and currents are influenced by standing wave effects [13], [83].

Cables, in comparison to overhead lines, are more likely to trigger resonances over lower frequencies where the damping effect tends to be the lowest. This is because cables normally have a smaller series impedance and relatively larger shunt capacitance components, unlike the overhead lines. Therefore, cables can be modelled using the same approach as the overhead lines, but some influencing factors require careful consideration for accurate harmonic analysis studies [84]. The cable design parameters provided by manufacturers are important to derive the most accurate model for harmonic studies. However, generic data and assumptions about parameters when cables are in operation can significantly impact the accuracy of damping effects [85]. Differences between manufacturer data and physical values often occur due to cable laying and bonding configurations that play a crucial role in the harmonic performance of a power system. Additionally, simplifications made over skin and proximity effects at the fundamental frequency for improving the computational efficiency of a simulation package can influence the model accuracy and lead to imprecisions in terms of damping at harmonic resonances. Factors affecting the harmonic model of cables are summarised as follows [82], [84], [85]:

- Cable length plays a major role in defining the resonant frequencies, peak value, and the number of resonant points for both the positive- and zero-sequence harmonic components. Long lines imply a shift in the locations of the harmonic resonances to lower frequencies. Moreover, the number of sections and type of models depending upon the line length (up to 2 km) will have a major impact on the positive-sequence components.
- Conductor cross-section affects the frequencies at which resonant points appear in the positive-sequence and has a negligible influence on the zero-sequence resonance peaks.
- Insulation material and thickness influence resonances in the positive-sequence components regarding the frequency and peak, while in the zero-sequence the peak only is altered.
- Cable arrangement considerably influences the frequency, peak, and number of resonant points in the positive-sequence components.
- Bonding configuration noticeably affects the positive-sequence harmonic components. However, it has a marginal impact on the zero-sequence components.

3. 1. 2. Power Transformers

A power transformer that is a key component in power systems, introducing an inductive behaviour over a wide frequency range and can consequently interact with capacitive elements of overhead lines or PFC capacitors causing parallel and/or series resonances. Hence, an accurately representative model of this commonly used equipment is paramount for a precise estimation of resonant points and realistic harmonic performance analysis. The harmonic model of a power transformer can be derived from the fundamental frequency basic transformer model with some aspects that require special attention for accurate harmonic studies [13], [86]. The common physical representation of a three-phase power transformer is shown in Figure 3-2, and the equivalent single-phase circuit is depicted in Figure 3-3.

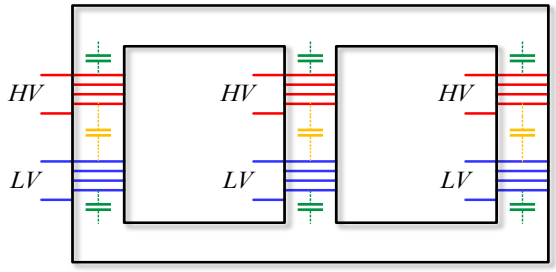

Figure 3-2 Physical representation of a three-phase power transformer.

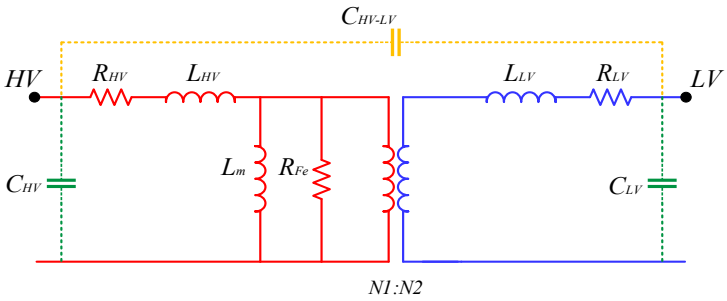

Figure 3-3 Equivalent circuit of a single-phase power transformer.

The stray capacitances in the transformer depending upon its configuration, type, and size can only have an observable influence on harmonic studies of very high frequencies (above 4 kHz) and thus can be excluded from the model. Additionally, when the transformer is assumed to operate under normal operating conditions that means the core continuously operates in the linear region, the magnetising branch (L_m and R_{Fe}) can be overlooked. Nevertheless, when transformer saturation is the main concern, the magnetising branch can be replaced by a harmonic current source defined by the flux analysis to capture such effects for harmonic studies [82].

Technical specifications of the transformer windings configurations and the tap-changer can affect the system's harmonic solution [17]. The leakage reactance is influenced by the tap changer and can shift resonant points, while the resistive component can provide beneficial damping at harmonic resonant points across the transformer. It is thus important to include the tap changer effect in a transformer equivalent model for harmonic analysis studies. Winding connections of power transformers can alter specifically the zero-sequence harmonic currents flow. Generally, when the system is balanced and symmetrical, triplen harmonic currents are trapped in windings connected in delta form and they flow to the transformer

neutrals grounded. These currents will consequently lead to protection relay operation and therefore accurate winding and neutral connections representation are recommended [82].

Based on these considerations, there have been several harmonic models of a power transformer taking into consideration the available or reasonably assumed data such as the rated power, leakage reactance and transformer resistance.

- **Model 1:**

The proposed model in [87] represents the power transformer with a lumped impedance (Z_h) composed of a resistance (R_{s_h}) connected in series with an assembly comprising a reactance (X_{Tr}) and resistance (R_{p_h}) in parallel as seen in Figure 3-4. R_{s_h} and R_{p_h} are calculated using the transformer reactance.

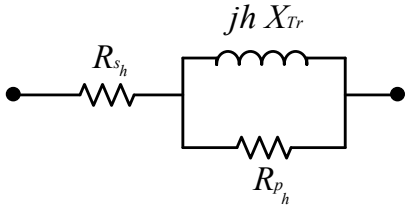

Figure 3-4 Power transformer harmonic model (Model 1).

The transformer leakage reactance at the fundamental frequency and the rated power of the transformer (S_r) in MVA are the required input data for this model. The leakage inductance (L_σ) in this model is assumed constant over the range of frequencies of interest, thus X_{Tr} rises linearly with frequency as follows.

$$X_{Tr} = 2\,\pi\, f_{fund.} L_\sigma \tag{3.3}$$

Where $f_{fund.}$ is the fundamental frequency. The resistances R_s and R_p are assumed constant over the frequencies of interest, and they are calculated based upon the rated power of the transformer as follows [87].

$$R_{s_h} = \frac{X_{Tr}}{\tan(\varphi)} \tag{3.4}$$

$$R_{p_h} = 10\, X_{Tr}\, \tan(\varphi) \tag{3.5}$$

$$\tan(\varphi) = e^{0.69+0.79\, lnS_r - 0.04(\ln S_r)^2} \tag{3.6}$$

Then the transformer equivalent impedance can be calculated as:

$$Z_h = R_{s_h} + (R_{p_h} // jhX_{Tr}\ ) \tag{3.7}$$

This can lead to:

$$Z_h = \left(R_{s_h} + \frac{h^2 X_{Tr}^2 R_{p_h}}{R_{p_h}^2 + h^2 X_{Tr}^2}\right) + j\left(\frac{h\, X_{Tr}\, R_{p_h}^2}{R_{p_h}^2 + h^2 X_{Tr}^2}\right) \tag{3.8}$$

Although the skin effect was not considered for the actual resistive part, the resultant expression shows that the resistive term is now frequency-dependent demonstrating the inclusion of the skin effect in this model.

- **Model 2**

In [88], it represents the power transformer by a series impedance (Z_h) as depicted in Figure 3-5.

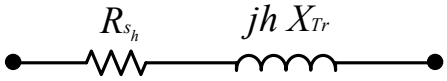

Figure 3-5 Power transformer harmonic model (Model 2-5).

The required data for this model is the transformer resistance (R_{1_h}) and the leakage reactance (X_{Tr}) at the fundamental frequency. Like Model 1, the leakage inductance (L_σ) is assumed constant over the range of frequencies of interest, and the X_{Tr} increases proportionally with frequency components as per Equation (3.3), and the resistive part is calculated as:

$$R_{s_h} = R_{1_h}(1 + A\, h^B) \tag{3.9}$$

In this model, the resistance frequency dependency is considered and the typical values for A and B are 0.1 and 1.5, respectively. The transformer equivalent impedance can then be calculated as:

$$Z_h = R_{s_h} + jhX_{Tr} \tag{3.10}$$

- **Model 3:**

As for Model 2, the proposed model in [89] represents the power transformer by a series impedance Z_h as shown in Figure 3-5 and requires the transformer resistance (R_{t_h}), leakage reactance (X_{Tr}) data at the fundamental frequency and power rating in MVA. The leakage inductance (L_σ) in this model is also assumed constant and the X_{Tr} consequently escalates linearly with frequency as per Equation (3.3).
The frequency dependency of the resistance accounting for skin effect is modelled with the typical coefficients presented in Table 3-1 under the condition that the summation of a_o, a_1, and a_2 must equal 1.

$$R_{s_h} = R_{t_h}\left(a_o + a_1 h^b + a_2 h^2\right) \tag{3.11}$$

Table 3-1 Coefficients of power transformer harmonic Model 3 [89]**.**

Transformer Size	a_o	a_1	a_2	b
< 100 MVA	0.85-0.90	0.05-0.08	0.05-0.08	0.9-1.4
≥ 100 MVA	0.75-0.80	0.10-0.13	0.10-0.13	0.9-1.4

- **Model 4:**

The power transformer model presented in [13] is represented also by a series impedance (Z_h) as demonstrated in Figure 3-5. The required data is the transformer fundamental frequency leakage reactance (X_{Tr}) and resistance (R_{s_h}), which is assumed to have the frequency dependency based on the typical characteristic discussed in [24]. Therefore, the harmonic model including the skin effect is computed as:

$$Z_h = \sqrt{h}\ R_{s_h} + jhX_{Tr} \tag{3.12}$$

- **Model 5:**

The power transformer model proposed for harmonic studies in [90] is also represented by a series impedance (Z_h) as depicted in Figure 3-5. In this model, the required data is also the transformer resistance (R_{Tr_h}) and leakage inductance (L_σ) at the fundamental frequency. The frequency-dependent effect of the transformer resistance and inductance is now included and can be calculated as:

$$R_{s_h} = R_{Tr_h}(1 + A_R(h-1)^{B_R}) \tag{3.13}$$

$$L_1 = L_\sigma \, A_L \, (h)^{B_L} \tag{3.14}$$

Where A_R, B_R, A_L, and B_L are the typical coefficients listed in Table 3-2. The harmonic impedance is then calculated as:

$$X_{Tr} = 2\,\pi\, f_{fund.}\, L_1 \tag{3.15}$$

$$Z_h = R_{s_h} + jhX_{Tr} \tag{3.16}$$

Table 3-2 Coefficients of power transformer harmonic Model 5 [90]**.**

Transformer Size	A_R	B_R	A_L	B_L
< 10 MVA	0.2	1.5	1	- 0.03
10 < MVA < 100	0.2	1.4	1	- 0.02
≥ 100 MVA	0.2	1.6	1	0

- **Simplified Model**

The simplified transformer model for harmonic studies presented in [91] is represented as a series impedance (Z_h) as depicted in Figure 3-5. The damping effect introduced by the skin effect is neglected to capture the worst-case scenario of harmonic amplification at resonant points, and the transformer harmonic impedance can be computed as:

$$Z_h = R_{s_h} + j\, h\, X_{Tr} \tag{3.17}$$

Where X_{Tr} and R_{s_h} are the transformer leakage reactance and resistance at the fundamental frequency.

For comparison between the different models, an illustrative power transformer with the assumed parameters shown in Table 3-3 and the typical coefficients of the models based on its size is used to plot the harmonic impedance (Z_h) over the range of harmonic frequencies up to 50th order as depicted in Figure 3-6. The comparative studies conducted for the different harmonic models of the power system components in this work were performed using MATLAB coded programs.

Table 3-3 Power transformer specifications for comparison between models.

Transformer Parameter	**Value**
Power rating	20 MVA (33/13.8 kV)
Leakage reactance (p.u.)	0.04
Resistance (p.u.)	0.0025
Fundamental frequency	60 Hz

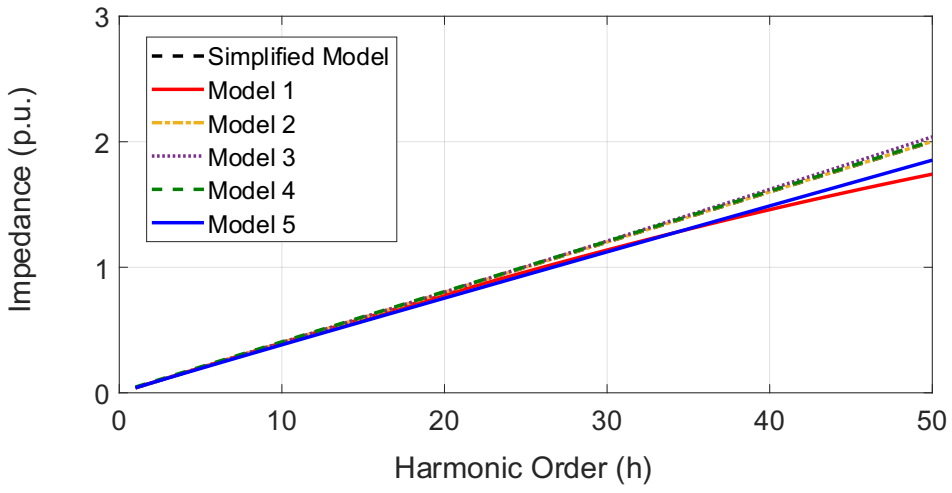

Figure 3-6 Power transformer impedance plots of different models.

The inductive behaviour of the power transformer that is anticipated to increase linearly with frequency dominates the harmonic model. The impedance plots

obtained from Model 2 to Model 4 and the simplified model are almost identical over the same range of frequencies, and this clarifies the simple implementation of the simplified model without the burden of calculating the corresponding coefficients. However, Model 1 and Model 5 are observed to have relatively smaller impedance over higher frequencies. This is due to the parallel resistance that slightly reduces the inductive component in Model 1, and the frequency dependency considered for the equivalent leakage reactance in Model 5.

3. 1. 3. Synchronous Generators

At the fundamental frequency, a synchronous generator is usually modelled as a voltage source behind an impedance as depicted in Figure 3-7(a). Apart from the fundamental frequency, when background voltage harmonics are negligible, the generator harmonic model is represented as shown in Figure 3-7(b).

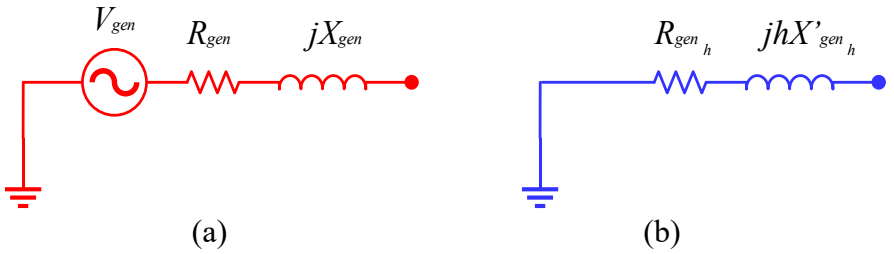

Figure 3-7 Power generator model at the fundamental (left) and harmonic frequencies (right).

For the frequency domain solutions, in the literature, there are several harmonic models proposed for power generators as follows.

- **Model 1:**

In [87], the generator model is represented by a series impedance (Z_{gen_h}) comprising a reactance and resistance with a frequency dependency factor of $\sqrt{h}$, and the model is computed as:

$$Z_{gen_h} = \sqrt{h}\, R_{gen_h} + \; j\, h\, X'_{gen_h} \tag{3.18}$$

Where R_{gen_h} is calculated from the generator power losses and X'_{gen_h} is the sub-transient reactance of the generator. Since the rotating magnetic flux due to harmonics within the stator rotates at a speed considerably higher than that for the rotor, the harmonic impedance of the generator matches its negative-sequence impedance. However, the equivalent harmonic impedance of the synchronous generator can be approximated using the sub-transient reactance [82].

- **Model 2:**

The model proposed in [88] represents the power generator in a similar manner but with an exponential factor for the skin effect. The model is also based on the sub-transient reactance (X'_{gen_h}) and the resistance (R_{1_h}) approximated from internal total losses that depends on the harmonic components as:

$$R_{gen_h} = h^a \, R_{1_h} \tag{3.19}$$

$$Z_{gen_h} = R_{gen_h} + \; j \, h \, X'_{gen_h} \tag{3.20}$$

Where a is the coefficient of the resistive part that takes a value between 0.5 and 1.5.

- **Simplified Model:**

This model neglects the skin effect and represents a power generator as a series impedance (Z_{gen_h}) comprising the sub-transient reactance (X'_{gen}) and resistance (R_{gen_h}) as presented in [91]:

$$Z_{gen_h} = R_{gen_h} + \; j \, h \, X'_{gen_h} \tag{3.21}$$

With the variety of harmonic models of a power generator, a concern can arise for accurate harmonic flow analysis and thus an investigation of the performance of these models is required. An illustrative power generator with parameters shown in Table 3-4 is utilised to plot the harmonic models over the range of harmonic orders up to 50th as shown in Figure 3-8.

Table 3-4 Power generator specifications for comparison between models.

Generator Parameter	Value
Power rating	50 MVA
Sub-transient reactance (p.u.)	0.2
Resistance (p.u.)	0.02
Fundamental frequency	60 Hz

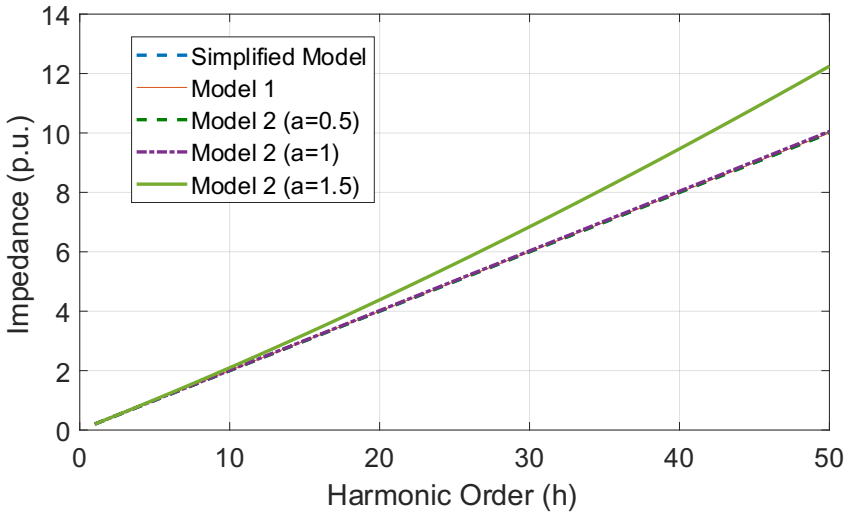

Figure 3-8 Power generator impedance plots of different models.

The simplified model with the skin effect neglected is observed to result in a similar performance to those obtained using Model 1, and Model 2 with coefficients of 0.5 and 1 respectively. However, a higher coefficient of 1.5 for Model 2 is observed to result in a significantly increased impedance over a high range of frequencies above 20^{th}, which can overestimate the high-frequency harmonic resonances and thus produce less accurate harmonic propagations analysis studies.

3. 1. 4. Loads

Loads can considerably affect the network harmonic characteristics in terms of resonance locations and damping effect, and thus it is very important to consider an accurate representation for accurate harmonic analysis studies [13]. Power loads are generally classified as either linear or nonlinear. Unlike nonlinear loads, static linear loads such as lighting and resistive heating draw a sinusoidal current from the power network. Rotating loads, however, such as motors are associated with nonlinearity and thus require accurate harmonic models. According to [87], [88], [91], static

liner loads are usually represented in a parallel connection form as shown in Figure 3-9.

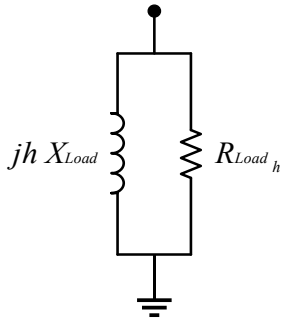

Figure 3-9 Power linear loads harmonic model.

Based on the active and reactive power components at the fundamental frequency, the harmonic impedance (Z_{Load_h}) of a static load is modelled by their equivalent resistance (R_{Load_h}) and reactance (X_{Load_h}) components as:

$$R_{Load_h} = \frac{V^2}{P_L} \tag{3.22}$$

$$X_{Load} = \frac{V^2}{Q_L} \tag{3.23}$$

$$Z_{Load_h} = R_{Load_h} \,//\, jhX_{Load} \tag{3.24}$$

Where V is the nominal node voltage in kV, and P_L (in MW) and Q_L (in MVAr) are, respectively, the active and reactive power drawn by the load at the fundamental frequency. Figure 3-10 demonstrates the influence of the different shares of active and reactive power components on the load harmonic impedance for an illustrative load with the parameters shown in Table 3-5. The higher the resistive content within the load the higher the damping effect the load can contribute to the distribution network. On the contrary, the highly inductive loads can result in higher impedance that may lead to a high-order harmonic amplification effect since they offer a less damping effect at potential resonant points. Therefore, accurate data on loads and their configurations are of high importance for a realistic harmonic analysis study.

Table 3-5 Power load specifications for effects investigation.

Load Parameter	Value
Operating voltage	33 kV
Maximum active power	5 MW
Maximum reactive power	5 MVAr
Fundamental frequency	60 Hz

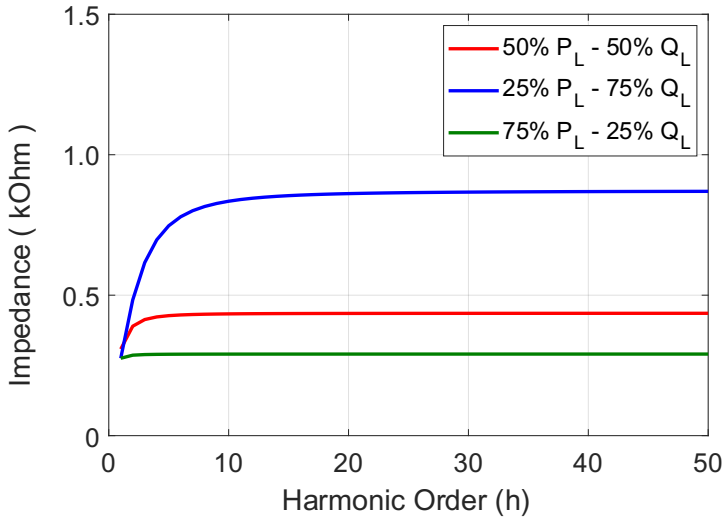

Figure 3-10 Power load impedance plots of different sharing of active and reactive power components.

The rotating loads, however, require further details to be modelled. The general structure of the rotating loads and their harmonic performance is usually a challenging task to obtain an accurate model for harmonic flow analysis in a power system. These loads are highly time-variant, and the active power absorbed is not precisely related to the damping behaviour [81]. Nevertheless, nonlinear loads incorporating PE such as variable speed drives and electric vehicles draw a non-sinusoidal current. These types of loads often introduce complexities for accurate harmonic modelling because of the harmonic currents they generate and their time-varying parameters, which cannot be represented by the equivalent linear harmonic modelling approaches [13]. Moreover, the type and topology of power converters and the interaction of the control system with the impedance of the AC network should be considered to accurately represent the nonlinear loads [24].

According to the comparative studies conducted, the different harmonic models reported in the literature for the key power system components depending on available data collected or provided by the manufacturer may result in slightly different harmonic performances, and the following recommendations can be drawn as follows.

- For long overhead lines (about 80 km and above), when harmonic resonances are of most importance and to avoid underestimation of the damping effect at these resonant frequencies, the skin effect, earth resistivity variations, and inter-circuit coupling effects should be considered using a cascaded lumped components (nominal-π model) or distributed parameters model, which can also lead to a shift in resonances, to capture the frequency dependency correlation of the resistance and thus provide a realistic harmonic performance.
- For power transformers, Model 2 to Model 5 with the fundamental frequency parameters and typical coefficients can produce a reasonable match to that of the simplified model, which appears to underestimate the damping effect at resonant points. However, recalculation of the models' coefficients can provide the best match to that of Model 1, which could sufficiently meet the measured frequency dependency of the transformer resistance to capture the damping effect, while the transformer reactance rises linearly with frequency. Additionally, when the objective is to investigate the harmonic resonances and propagations in a power network, the accuracy of the transformer model for buses that are electrically distant from the power transformer would have a marginal impact on the overall harmonic solution especially when cables are not present in the power system.
- For power generators, the simplified model with accurate data obtained either from the manufacturer or real measurement can offer a reasonable solution that matches that of Model 1 and Model 2 except for the higher exponential factor of 1.5. However, the influence of these models' parameters could be more evident at the resonant points and electrically close nodes to the power generators that provide some level of damping. Furthermore, when series reactance and resistance of other power system components such as

transformers, lines and loads are included, the effect of an accurate model of the power generator should be less significant on the overall harmonic flow analysis.

- For linear loads, it is highly recommended to acquire accurate information on the nature and configuration of these loads to provide a realistic representative harmonic model depending on the voltage level for which the harmonic flow analysis is performed. At transmission levels, the differences between the series and parallel load models can be insignificant. However, at medium- and low-voltage levels to which the power loads are connected, the connection configurations of loads can have a significant impact on the damping effect at the resonant frequencies, and thus results in a different impedance profile.

3. 2. Harmonic Modelling of Albaha Power Network

3. 2. 1. Background

The Saudi 2030 Vision target of sharing 50% of the total current 80 GW power generation by the RES has motivated electric power operators all over the country [92]. To reduce greenhouse gas emissions in the power sector, electric power networks should adapt for the future energy transition that promotes the electrification of several sectors via RES, which will primarily be connected to distribution networks. Consequently, distribution networks operators should meet the challenge of high penetrations of renewable-based DG systems such as solar PV and wind power, and the high energy demand is estimated to grow threefold by 2030. This requires extensive and expensive technical reinforcements for the power network to sustain the network operating within voltage, fault, and thermal constraints and to comply with the regulations and standard limits.

The high potential for solar power in the southern region of Saudi Arabia, which has motivated researchers to investigate its economic feasibility and technical challenges, can be utilised to support the government pledge of delivering such a magnificent share by 2030 [93], [94]. Furthermore, the Albaha local power demand is on the rise. This is mainly because of the continuous development of the residential areas, Albaha University hospital that is under construction, and the

expansion of the Albaha airport [95], [96]. This emphasises the challenges that power suppliers should meet.

On the other hand, Bisha city, which has one of the largest conventional power generating stations in Saudi Arabia, is currently the main power supplier for the Albaha power network. It has a significant potential for solar, hydropower, and wind resources that will be adopted to meet its local growing energy consumption and the Albaha city power demand through the existing and proposed interconnections [93], [94]. Technically, Bisha is predicted to generate more power than its local demand, and thus surpluses of power could be transported to fulfil the growing power demand of Albaha city. Therefore, with the restricted existing interconnections between Bisha and Albaha cities, voltage and thermal challenges will consequently be triggered in several locations in the power networks, and the MVDC system with its advantages over the conventional AC systems and controllability feature for the power flow is proposed to help mitigate these issues and enable high penetrations of renewables to contribute to the dedicated effort for meeting the "Saudi 2030 Vision" target.

3. 2. 2. Description of the Power Network

This research work starts with representing the Albaha power system for performing power system analysis of different cases including the ongoing development of the Albaha airport and the Albaha University hospital. There is no publicly available data or a piece of research providing holistic information on the Albaha power network due to the data sensitivity. For this study, the Albaha network data was collected during field trips to recognize the nature of the network and its components. The Albaha power system is represented as depicted in Figure 3-11. It consists of 23 buses of 132, 33, and 13.8 kV, 13 power transformers, 36 aggregated domestic loads connected to 33 kV and 13.8 kV, and the two existing interconnections with Network 1 and Network 2. The specifications and details of the Albaha power network are shown in Appendix 1.

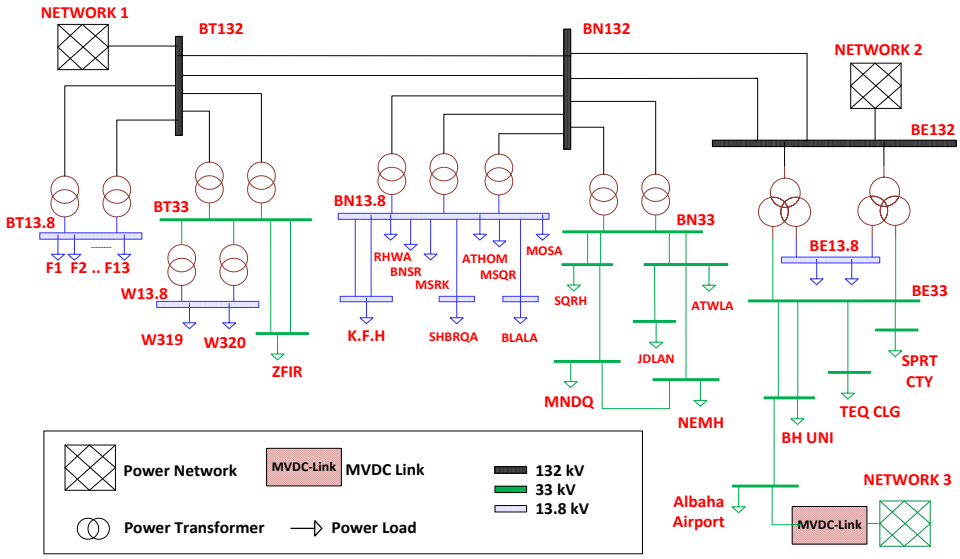

Figure 3-11 Albaha power network with the proposed MVDC system.

The total power demand of the Albaha network is about 220 MW, which is being delivered mainly from the two networks. Network 1, which represents a recent interconnection to compromise the closure of the local Albaha power generating station, has a power capacity of around 60 MVA, while Network 2 is considered the dominant source of power that provides about 180 MVA from the Bisha power station. Network 3 represents the proposed connection through the MVDC system to a site with a high potential for solar, wind, and hydropower resources that are under planning and located in the northwest region of Bisha City.

3. 2. 3. Load Flow Analysis

A load-flow or power-flow, which is a steady-state solution at the fundamental frequency, computes the voltage profile and branches power flow for specific generation and loading conditions for a power system. Considering normal operating conditions, this study calculates the voltage magnitude and angle of all buses in the network and then the real and reactive power flow through the whole power network can subsequently be determined. The power-flow solution adopted in the IPSA power system simulator is the fast Decoupled Power Flow method. The decoupling theory is associated with the inherent characteristic of a practical power

system and the capability of solving radial and weakly meshed power distribution networks.

By considering the Albaha network with the collected data, the load flow is performed for different case scenarios including the estimated demand required for the electrification of the Albaha airport and Albaha University hospital as shown in Table 3-6. Case 1 reflects the actual current state of the Albaha power system prior to the developments of the airport and hospital, while other cases correspond to the system with the estimated increase in power demands due to the projects and the MVDC power supply capability. This study was performed using IPSA and it aims to evaluate the voltage of buses against the standard limits and the system power losses. Network 2 is assumed as a reference (slack) bus, and the results of the load-flow study are summarised as follows.

Table 3-6 Different case studies for power flow analysis.

Scenarios	**Average load simulated**				**MVDC System** (supplying)	
	Albaha airport		Albaha University hospital			
	P (MW)	Q (MVAr)	P (MW)	Q (MVAr)	P (MW)	Q (MVAr)
Case 1	5	3	11	9	-	-
Case 2	8	5	15	11	-	-
Case 3	8	5	15	11	15	0
Case 4	8	5	15	11	30	0

3. 2. 3. 1. Voltage Profile

The voltage magnitudes (in p.u.) at different voltage levels are depicted in Figure 3-12 through Figure 3-14. At the 132 kV power transmission level, the voltages of buses for the different cases are within the acceptable level of ±5% as stated in [97]. This is because of the shunt capacitance (susceptance) of the transmission lines that compensate for the voltage drop across the lines' series impedances. The voltages of the 33 kV buses have different profiles for different cases due to the direct connection of the power loads. The remote buses from the development projects are within the voltage standard limit of ±5% for all cases. For Case 2, however, with the increased loads, the voltages are below the acceptable level. For instance, the 33 kV buses of the Albaha University hospital and Albaha airport are

approximately 6.5% below the rated voltage. This results from the high current flowing through the lines, which is associated with the extra power required, and consequently a large voltage drop developed across the line resistance affecting the receiving end voltage. For the medium voltage network with a relatively low X/R ratio, the significant overhead lines resistances develop a higher voltage drop and thus are responsible for the voltage degradation at the receiving end [98].

On the other hand, the large active power supplied through the MVDC system in Case 3 and Case 4 can significantly improve the voltage at the Albaha airport bus and bring up the voltages of the surrounding 33 kV buses of the distribution network to the acceptable limit. Therefore, Case 3 and Case 4 shown in Figure 3-13 indicate the significant contribution of the MVDC system to the voltage improvements at nearby buses. For 13.8 kV buses, the voltages are within the acceptable level of ±5% for the different cases, and a minor impact on the nearby BE-13.8 bus is observed.

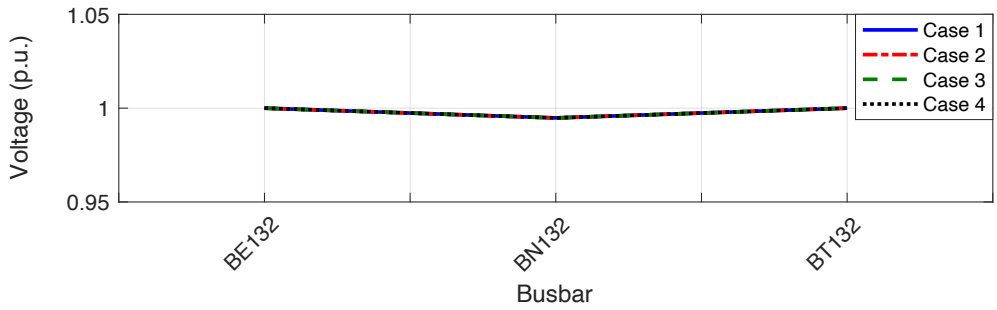

Figure 3-12 132 kV voltage profile with different sceneries.

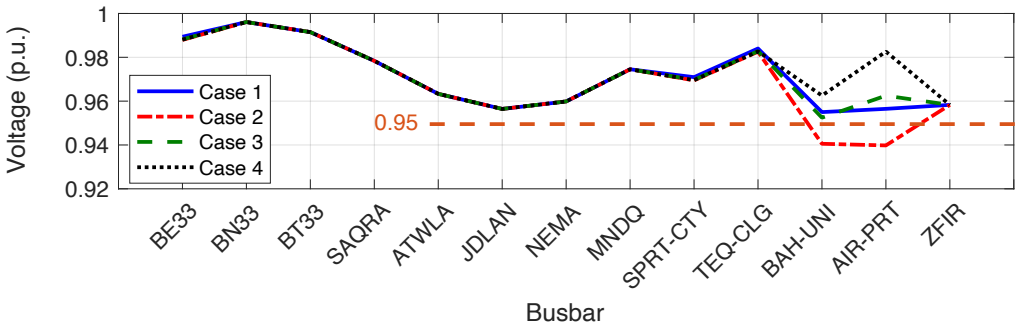

Figure 3-13 33 kV voltage profile with different sceneries.

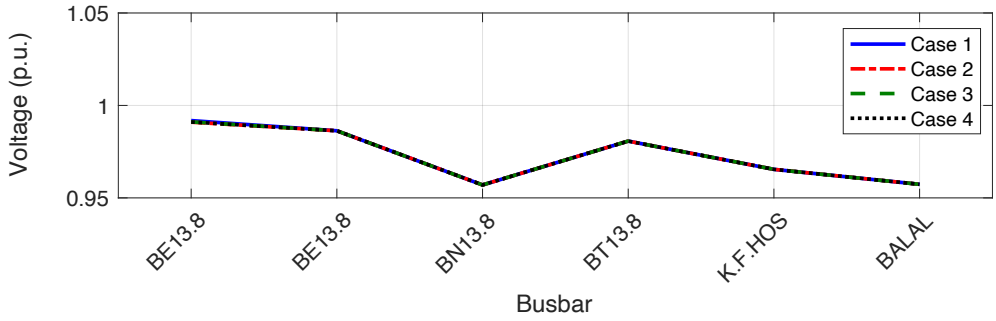

Figure 3-14 13.8 kV voltage profile with different sceneries.

3. 2. 3. 2. Power Supply and Power Losses

With the existing interconnections in the Albaha power system, Network 2 mainly contributes a significant amount of power supplied. However, the MVDC system can improve the reliability and security of the Albaha power supply by providing a flexible and controllable power exchange of up to 30 MW from Network 3. As shown in Figure 3-15, about 140 MW is supplied from Network 2 in Case 1 compared to roughly 160 MW in Case 2 when considering the development projects of the airport and hospital. For Case 3 and Case 4, the flexible MVDC system operating at a unity power factor can compensate for both the power required by the projects and the high power transferred through Network 2, which will also help minimise total power losses in the lines. Additionally, the MVDC system with its capability of independently controlling the reactive power at both AC ends can further reduce the reactive power losses and improve the system voltage profile and efficiency.

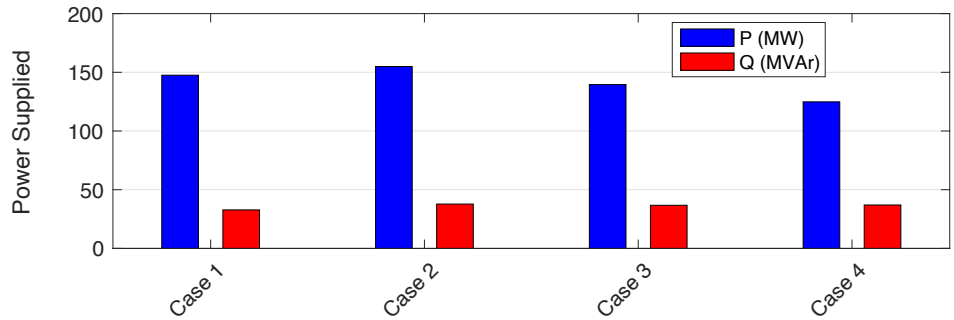

Figure 3-15 Power supplied by Network 2 for different sceneries.

An unavoidable consequence of transferring power from the upstream network to loads connected to the distribution network is the power losses related to the impedances of the overhead lines, which can lead to significant financial and environmental effects on the distribution network operator and end-users. Commonly, the considerable losses in a power system are in the distribution lines, while the high voltage transmission lines account for a marginal portion of the total losses. For the Albaha power system, the 33 kV network power losses for the different cases are shown in Figure 3-16.

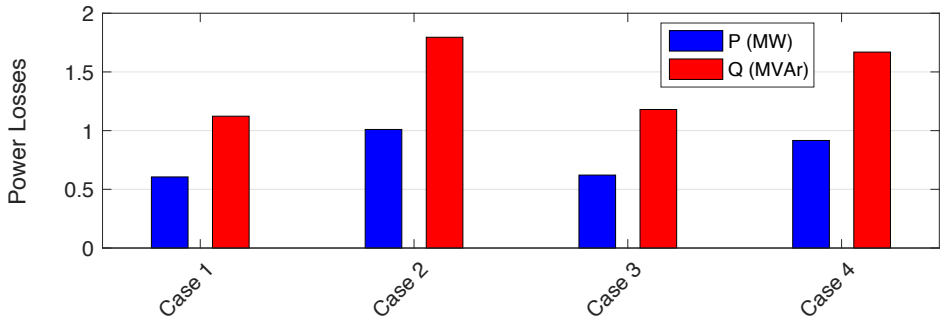

Figure 3-16 Power distribution network losses for different sceneries.

The increased loads of the Albaha airport and Albaha University hospital in Case 2 resulted in a 1 MW active power loss in the eastern region, which is almost double that of Case 1. Case 3 and Case 4 indicate the impact of the power injected by the MVDC system on the power network losses around where the development projects take place. The results suggest that there will be a considerable reduction in network losses by optimising the settings of the active and reactive power setpoints of the MVDC system for optimal power demand management. With 15 MW at unity power factor operation of the MVDC system, the impact of the increased loads can be eliminated. In Case 4, for the current loading condition, high power losses can be experienced when the MVDC system supplies its maximum rated power. However, for the growing energy consumption due to the continuous developments in the region, the MVDC system can further tackle the future losses problems in the distribution network.

3. 3. MVDC Converter Harmonic Penetrations into the Albaha Power Network

Conventionally, electric power systems are intended to operate with sinusoidal voltage and current waveforms. Yet, the PE-based nonlinear loads and RES-based systems would distort these AC waveforms at the steady-state operation, and equivalent harmonic components of such distorted waveforms can be computed. Power harmonic studies investigate the generation and propagation of these harmonics through the power system [13], [99]. Harmonic analysis has become of significant importance for power system engineers to compute the voltage and current distortions at different points and determine potential risky resonant points and how they might be lessened. Such investigations are essential in today's power networks because of the growing number of harmonic-producing systems. As power harmonics flow into the network, increased losses and potential equipment loss-of-life are predicted. Harmonic resonances resulting in overcurrent or overvoltage can damage power system components. Moreover, harmonics can affect the control, communication, and protection systems [13], [17].

The simple frequency domain approach utilised in harmonic flow analysis, primarily for the characteristic impedance scans and harmonic penetrations studies, is the most widely used in the industry for evaluation against standard limits [13], [100]. Harmonic analysis formulation in the frequency domain can be reliable and efficient, and it requires a low computation cost for steady-state solutions. Yet, for power converters and the non-linear behaviour of power transformers and motors, the use of this solution can be sufficient but not accurate [101], [102]. The harmonic standard limits, which can vary from one country to another and depend on the network voltage level, provide the permitted harmonic distortions levels with the consideration of the pre-existing or background harmonics in the network. The THD limits defined by the SERA for different voltage levels are shown in Table 3-7.

Table 3-7 Total harmonic distortion limits defined by the SERA.

Nominal Voltage (kV)	THD (%)
132	1.5
33	3.0
13.8	4.0
0.38	5.0

With the presence of a harmonic generating source such as the MVDC system in the Albaha power network, harmonic flow analysis is performed to determine at different nodes the consequential voltage total and individual harmonic distortion resulting from the propagation of the current components of frequencies other than the fundamental frequency. The Albaha power network is modelled in this section to assess the performance of the MVDC converter harmonics and evaluate their penetrations at different voltage levels. Using the collected data with the geographical specifications of the power system, the overhead lines are modelled first with the nominal-π models since they are categorised as short lines.

3. 3. 1. 33 kV Overhead lines Modelling

The harmonic flow in a power system is greatly influenced by the level of the representation of the system components and the end-users loads supplied radially. To calculate the harmonic impedances at the distribution level (33-69 kV), an appropriate harmonic model should be used to represent the overhead lines. The high resistance of overhead lines, which plays a key role in damping resonances, should be incorporated into the equivalent harmonic model [13]. To compute the shunt capacitance of the overhead lines, a method that uses conductors' specifications and their images shown in Figure 3-17 is employed [83].

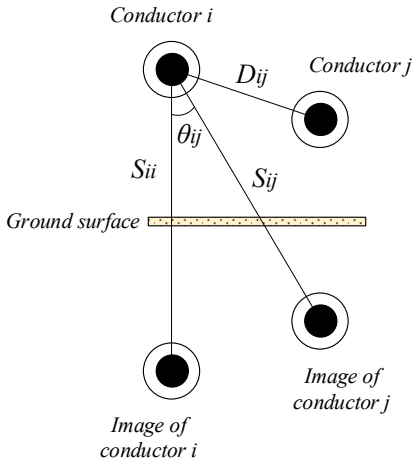

Figure 3-17 Overhead conductors and images for lines' capacitance calculation [83]**.**

The air relative permittivity is approximated to 1, so the free space permittivity becomes:

$$\varepsilon = 1.0 \times 8.854 \times 10^{-3} \ (\mu F/km) \tag{3.25}$$

The self- and mutual-potential coefficients are then described as [83]:

$$P_{ii} = \frac{1}{2\pi\varepsilon} \cdot In\left(\frac{S_{ii}}{RD_i}\right) \ (km/\mu F) \tag{3.26}$$

$$P_{ij} = \frac{1}{2\pi\varepsilon} \cdot In\left(\frac{S_{ij}}{D_{ij}}\right) \ (km/\mu F) \tag{3.27}$$

Where D is the distance between conductors in cm, S is the distance between conductor and image in cm, RD is the radius of the conductor in cm, and θ is the angle between images in degrees.

For an overhead line of n conductors with a four-wire grounded configuration, an $n \times n$ matrix of the primitive potential coefficients "$P_{primitive}$" can be built as [83]:

$$[P_{primitive}] = \begin{bmatrix} P_{aa} & P_{ab} & P_{ac} & \vdots & P_{an} \\ P_{ba} & P_{bb} & P_{bc} & \vdots & P_{bn} \\ P_{ca} & P_{cb} & P_{cc} & \vdots & P_{cn} \\ \cdots & \cdots & \cdots & \cdot & \cdots \\ P_{na} & P_{nb} & P_{nc} & \vdots & P_{nn} \end{bmatrix} \tag{3.28}$$

The partitioned matrix can be written as:

$$[P_{primitive}] = \begin{bmatrix} [P_{ij}] & [P_{in}] \\ [P_{nj}] & [P_{nn}] \end{bmatrix} \tag{3.29}$$

The matrix can be reduced using the method of Kron reduction for the *abc*-frame potential coefficient matrix as:

$$[P_{abc}] = [P_{ij}] - \frac{[P_{in}][P_{nj}]}{[P_{nn}]} \tag{3.30}$$

By inverting the *abc*-frame potential coefficient matrix, the susceptance matrix of overhead lines can be obtained as:

$$[B_{abc}] = j2\pi f \cdot [P_{abc}]^{-1} \ (\mu S/km) \tag{3.31}$$

For the Albaha 33 kV distribution network with technical specifications shown in Table 3-8, the average of diagonal elements of susceptance matrix of 4.5 $\mu S/km$ that refer to line-to-ground capacitances is adopted to represent the overhead lines with the harmonic model shown in Figure 3-18. This can be justified as the distribution network has an untransposed horizontal configuration with the same spacing between the conductors, and three-phase conductors are symmetrical with a neutral line grounded. The capacitances between conductors are neglected due to their very small values and thus negligible effects on the harmonic analysis.

Table 3-8 33 kV Albaha network overhead lines specifications.

Design Parameter	Value
Pole height	10 m
Conductor separation distance	0.9 m
Conductor cross-sectional area	150 mm^2
Neutral conductor height	8 m
Neutral conductor cross-sectional area	50 mm^2

The overhead lines of the eastern region of the Albaha distribution network around where the proposed MVDC converter will be connected are modelled by the nominal-π model with the parameters calculated and presented in Table 3-9, for which the parasitic resistance of the capacitive elements is assumed negligible.

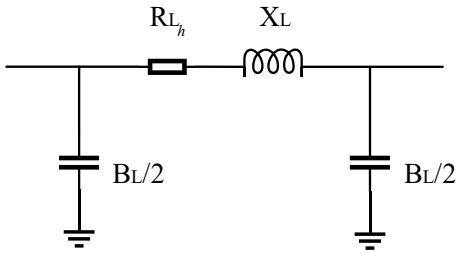

Figure 3-18 Overhead line representation.

Table 3-9 Developed 33 kV Albaha network overhead lines parameters.

Lines		Line Length (km)	Resistance R (Ω)	Inductance X (Ω)	Susceptance B (μS)
From	To				
BE33	SPRT-CTY	3	0.41	0.88	15
BE33	TEQ-CLG	6	0.62	1.32	30
BE33	BH-UNI	15	2.63	4.85	75
BE33	BH-UNI	15	2.63	4.85	75
BE33	AIR-PRT	22	3.32	4.41	110
BH-UNI	AIR-PRT	12	1.32	2.50	60

By adhering to the recommendations on the harmonic models of power system components in the frequency domain, the harmonic model of the Albaha network is now applicable for harmonic analysis studies. Model 1 and the simplified model, respectively, are used for the power transformers and generators since they were appointed in the literature as the most accurate models. The nominal-π model including the skin effect is used for the overhead lines since they are shorter than 80 km. The parallel linear load model is used with average power demand to represent the linear loads of the Albaha network.

For the MVDC converter connected to the Albaha airport bus, the frequency domain method is conducted using the IPSA power system simulator to study their penetrations at different voltage levels. The Albaha network is modelled with the assumption of balanced loads and symmetrical lines. The harmonic currents of the MVDC converter modelled in Simulink/MATLAB are softly linked to the network model to reduce the simulation running time and enable such study in the IPSA. The soft linking approach is a common practice to represent the harmonic spectrum by multiple current sources of different frequencies [20].

3. 3. 2. Harmonic Propagations at 132 kV Level

Commonly for harmonic flow analysis studies, harmonic orders up to 50th are of interest. However, harmonic orders up to 100th are included to capture the MVDC converter harmonic performance with possible high-frequency resonances. At the 132 kV buses, the impedance plots shown in Figure 3-19 indicate a resonant point around 52nd due to the high-voltage lines capacitances, with another resonance

beyond the scope of this study. Therefore, there is an expected harmonic voltage amplification at this resonance point, especially for BN132 bus depending on the harmonic currents. Figure 3-20 depicts the voltage distortion of 132 kV buses. BN132 has the highest harmonic content around the 52nd order, while BE132 has higher low-order harmonics due to its short distance to the harmonic source. For transmission systems, the SERA stresses that the voltage THD should be less than 1.5%. Fortunately, the voltage THD does not exceed the standard limits as shown in Table 3-10.

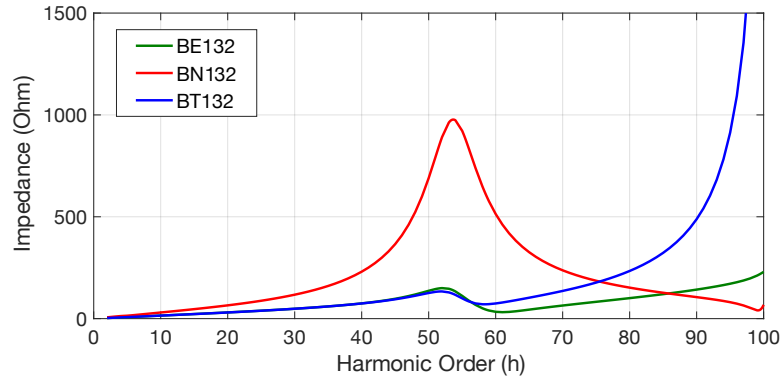

Figure 3-19 Impedance scan performed at 132 kV levels.

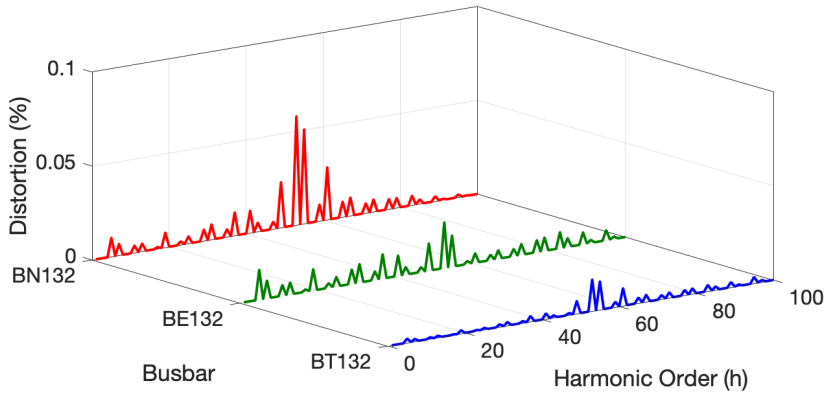

Figure 3-20 MVDC harmonic propagations at 132kV.

Table 3-10 Harmonic distortions at the 132kV level

Name	Voltage THD (%)	Harmonic Order of Max. Distortion	Maximum Individual Voltage Distortion (%)
BE132	0.05	53	0.02
BN132	0.09	53	0.06
BT132	0.03	53	0.02

3. 3. 3. Harmonic Propagations at 33 kV Level

At the 33 kV buses near the harmonic source, the impedance plots with the overhead lines modelled by their equivalent nominal-π models are shown in Figure 3-21. They are almost linear with a negligible resonance around 52nd caused by the transmission lines' capacitance. In this case, when there is no amplification risk from significant resonances, the voltage distortion on a specific bus is subject to the impedance seen, the harmonic currents fed, and how close to the harmonic source it is. Figure 3-22 shows the voltage distortions of some 33 kV buses. High voltage distortions are observed at AIR-PRT bus, which has the highest impedance and is the closest to the harmonic source. BAH-UNI bus, with a smaller impedance in comparison to TEQ-CLG bus at higher frequencies, is the second highly distorted voltage due to its location with respect to the harmonic source. A summary of the voltage distortions with THD and individual distortion is provided in Table 3-11, and they comply with THD limits of 3%.

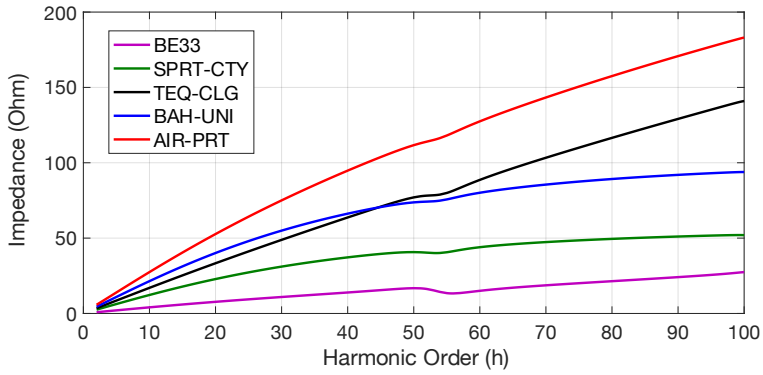

Figure 3-21 Impedance scan performed at 33 kV levels.

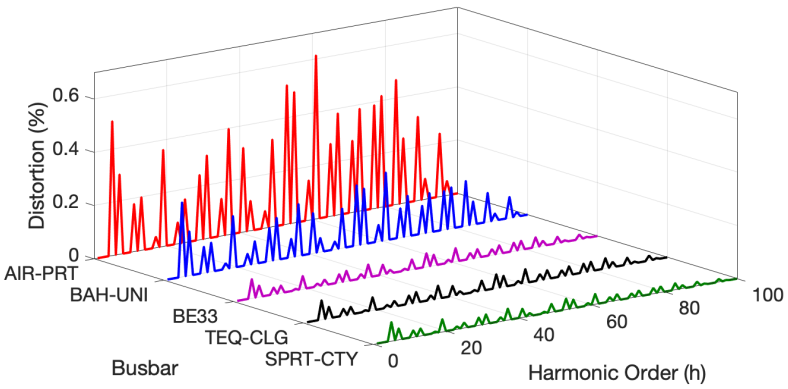

Figure 3-22 MVDC harmonic propagations at 33 kV.

Table 3-11 Harmonic distortions at the 33 kV level

Name	Voltage THD (%)	Harmonic Order of Max. Distortion	Maximum Individual Voltage Distortion (%)
BE33	0.19	5	0.07
SPRT-CTY	0.16	5	0.07
TEQ-CLG	0.18	5	0.07
BAH-UNI	0.85	5	0.28
AIR-PRT	1.90	61	0.61

3. 3. 4. Harmonic Propagations at 13.8 kV Level

For the 13.8 kV level, the impedance plots are depicted in Figure 3-23. BT13.8 with its high-power demand acts as a resistive load over a wide range of frequencies, which is expected to dampen the harmonic currents and suppress them from propagating into further loads along the bus. On the other hand, the transmission lines' capacitance through the transformers impedances of BN13.8 and BE13.8 result in marginal resonances that can magnify the harmonic current at these frequencies. Figure 3-24 shows the voltage distortions at these buses. It is observed that the closer bus to the harmonic source has the largest voltage distortion as for BE13.8, and the damping behaviour seen at BT13.8 being away from the harmonic source has the lowest voltage distortion. Table 3-12 shows the voltage THD with the highest individual harmonics at 13.8 kV buses. The distortions comply with the standard limits of 4% THD, and future installations of harmonic sources at BE13.8 should consider these as background distortions.

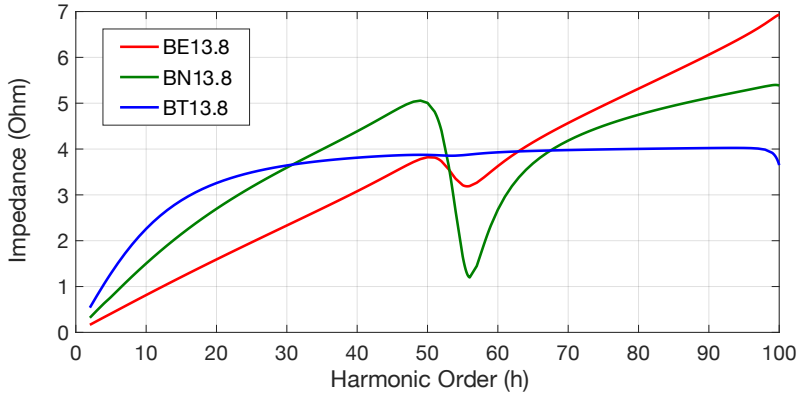

Figure 3-23 Impedance scan performed at 13.8 kV levels.

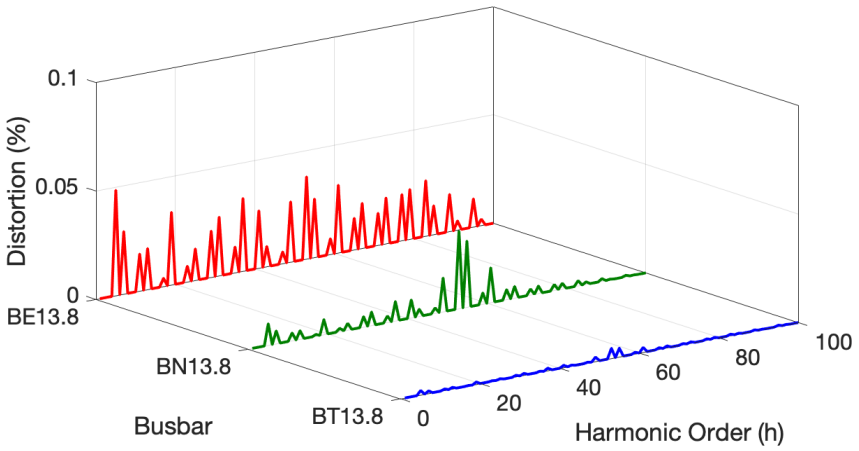

Figure 3-24 MVDC harmonic propagations at 13.8 kV.

Table 3-12 Harmonic distortions at the 13.8 kV level

Name	Voltage THD (%)	Harmonic Order of Max. Distortion	Maximum Individual Voltage Distortion (%)
BE13.8	0.13	5	0.050
BN13.8	0.06	53	0.040
BT13.8	0.01	53	0.004

The SERA regularly revises the standard limits with the increased penetrations of the DER-based power sources into the existing power systems. It defines the regulations for a variety of participants accessing and utilising the power distribution networks. Obligations, responsibilities, and accountabilities are also clarified so that the operation safety, reliability, and efficiency are maintained by all the parties involved. It defines the minimum technical requirements to guarantee the operation without extra costs and undesirable consequences [97].

When the MVDC system operates in the Albaha power distribution network, the resultant voltage distortions at different voltage levels comply with the THD limits defined by the SERA. The voltage THD of 1.90% at the PoC also complies with the standard limit at the 33 kV level. However, individual harmonic components should undergo further investigations to explore the risk of the EMC to the sensitive electronic loads at the nearby airport and hospital.

3. 4. Summary

In this chapter, the available harmonic models of the most crucial power system components in the literature were reviewed and compared. Recommendations for accurate harmonic models were highlighted. The Albaha Power system was modelled based on the data collected for load flow and harmonic flow analysis studies. For different scenarios, the MVDC system has improved the system's voltage profile at different substations, reduced power losses, and provided power flow controllability that can enable future connection of renewables in the AC grids. The MVDC converter harmonic propagations and penetrations were also investigated in the Albaha power system at different voltage levels, and harmonic distortions compliance with local standard limits were evaluated, and results were discussed. The MVDC converter harmonic performance in the Albaha power system revealed that the THD at different voltage levels comply with the standard limits

Chapter 4. Passive Power Filter Design and Harmonic Performance Analysis

In this chapter, the recently developed Manta Ray Foraging (MRFO) optimization algorithm is implemented for the Passive Power Filter (PPF) applications, and its performance is investigated. Additionally, an analytical approach based on the Monte Carlo Simulation (MCS) method is developed for statistical evaluation of the harmonic performance of an optimally designed PPF with uncertainties at the network level. A critical review of the optimization algorithms employed for PPF applications is undertaken. The problem formulation, objective function, and constraints are set for the PPF parameters design problem. A comprehensive comparison between the MRFO and the most recently proposed optimization algorithms is presented for superiority validation. The harmonic performance of the PFF using the developed MCS-based method is presented and discussed.

4. 1. Introduction

Modern power distribution networks are anticipated to be contaminated with significant harmonic distortions due to the increased utilisation of Power Electronics (PE)-based systems [11], [103]. The harmonic currents generated by a grid-connected power converter such as an MVDC converter must comply with the planning harmonic levels [45]. However, due to the aggregation of the harmonic distortions of one bus with those of the neighbouring buses, the voltage at various nodes and current through power lines can undergo significant distortions. Power harmonics are not only known to cause excessive heating and power losses in power system components but are also harmful to consumer electronic loads, industrial drives, and communication systems [13]. Furthermore, they can significantly limit a power network's capacity for high penetrations of the Distributed Energy Resources (DER)-based power sources. Power transformers and cables loading capacity can also be affected by harmonic distortions [104]. Therefore, harmonic distortions should be controlled to maximise the network's capacity, improve system components' performance, and comply with the locally established standard limits. At the power network level, an appropriate harmonic mitigation technology, such as passive and active power filters (or a combination of both), can be utilised

to overcome the adverse effects of the power harmonics [13]. PPFs are the most favourable solution due to their simple implementation and low cost [105], [106]. However, the design of PPF parameters remains a challenging task for engineers, given the power system requirements.

The shunt PPFs shown in Figure 4-1 are the most popular harmonic reduction solutions in the industry. High-pass power filters are referred to as damped-type passive power harmonic filters. Unlike the single and double tuned PPFs, these damped-type harmonic filtering solutions, which introduce a low impedance over a wide range of high frequencies and have a broadband damping characterization, can simultaneously suppress a wide range of the high-order harmonic components.

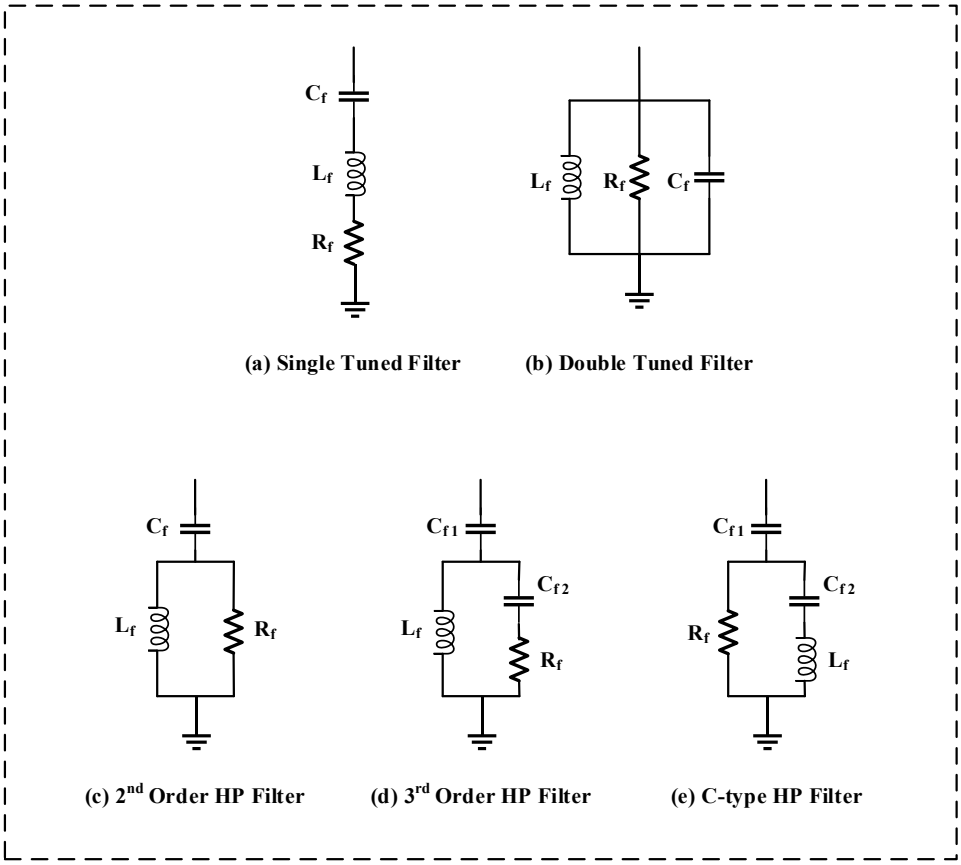

Figure 4-1 PPFs common topologies.

In practical applications, there are several common configurations of high-pass power filters including the 2nd-order, 3rd-order, and C-type high-pass filters. Due to their low cost, unique filtering characteristics, and simple implementation, PPFs

have been widely utilised in real applications. The 2nd-order filters were adopted to eliminate the telephone interference issues caused by a High Voltage Direct Current (HVDC) system [107]. The high order harmonics problems of the New Zealand HVDC link, Vancouver Island HVDC, and Cross-Channel HVDC were addressed by the employment of 3rd-order high-pass power filters. The developed C-type power filters were also proposed for real power systems such as HVDC links to reduce the high-order harmonic contents with lower power losses [108].

These power filters have similar characteristics but different components and layouts to achieve a certain objective. Firstly, the PPFs shown in Figure 4-1(a and b) are used for specific harmonic orders to attenuate. The 2nd-order high-pass filter topology is like the single-tuned power filters but with a resistor connected in parallel with the inductor as depicted in Figure 4-1(c). The 2nd-order filters are a more economical decision for situations where a wide range of harmonics are to be reduced in comparison with the multiple single-tuned filters solution. However, the 3rd-order filters shown in Figure 4-1(d), which are believed to reduce the power losses associated with the 2nd-order type, have an extra capacitor connected in series with the resistor to achieve better filtering efficiency. Similarly, the C-type power filter depicted in Figure 4-1(e) with the same number of passive components of 3rd-order filters has a potential for reduced fundamental power losses.

To achieve the desired harmonic filtering performance, a sophisticated design approach for these high-pass filters is required. Since the 2nd-order filter has a lower number of passive components implying lower weight, cost, and size, it stands out as the optimal option among other high-pass power filters. This is because of the inherent limitations associated with 3rd-order and C-type power filters such as the effect of the operating conditions and ambient temperature on the filter components parameters that can lead to parameters' variations and thus can result in a different system characteristic impedance. Besides, the complexity of the design is due to the involvement of more governing equations for the 3rd-order and C-type filters in the design stage.

For the design of a 2nd-order high-pass filter, the capacitor can be sized based on the reactive power and PFC requirements at the PoC. However, in a distorted power system, the PFC is more complicated to address and conventional methods that are

based on sinusoidal voltage and current traces can lead to a poor PFC solution. Another challenge is the inductor size, which should be tuned for a maximum harmonic reduction. Furthermore, the filter quality factor related to the damping resistance should be optimally selected to ensure the required performance of the 2nd-order high-pass filter. To overcome these challenges, optimization algorithms with the capability of global searching for the best solutions have been used in many applications including PPFs design.

4. 2. Previous Work

The PPFs can be designed through a power load flow program to determine their parameters using the trial-and-error approach. Instead, optimization algorithms have been widely used to obtain an accurate design with reduced time and effort burdens although this approach requires prior knowledge about the system. The nature-inspired optimization algorithms developed for engineering applications have placed attention on the optimal design of PPFs to improve their performance for given criteria [106], [109]. In [110][111], the Genetic Algorithm (GA) was used to optimise the parameters of different PPF topologies. The authors considered the impact of parameter variations on the PPFs' performance. In addition, the use of a GA to minimise the THD of current and reduction in total cost was discussed in [112]. GA was also adopted in [113] for the proposed approach for the optimal location and sizing of PPFs. Similarly, a modified, GA-based, multi-objective optimization problem for the placement and selection of filters was developed and discussed in [114]. An optimal design for a dynamic tuning PPF using the GA for harmonic distortions and cost minimization was discussed in [115]. This classical optimization algorithm has shown better computational effort, but it would require optimal coefficients setting to overcome local optimal solutions issue.

The authors in [116] compared the GA and some other algorithms with a built-in optimization tool for a power system simulation software to size and place some PPFs in a test network. The optimization problem was formulated using the Decoupled Harmonic Power Flow (DHPF) method, which was also adopted to design a high-pass PPF utilising the multi-objective Firefly Optimization Algorithm in [21]. In [117], GA was adopted to design a C-type filter in a distorted system with maximising the load Power Factor (PF). The performance of the GA solution

could be evaluated against the generic programming code-based solution discussed in [118]. Regarding C-type filters, Harris Hawks Optimization performance was investigated against some other algorithms with reduced overloading on PPFs as an objective in [119]. In [120], the Crow Search Algorithm was applied to minimise the total cost of 3rd-order and C-type PPFs. Several PPF configurations were optimally designed to minimize the Total Demand Distortion (TDD) by employing the Crow Spiral Algorithm [121]. A single-tuned PPF was designed in [122] to minimise the voltage Total Harmonic Distortion (THD) using Particle Swarm Optimization (PSO). The optimization problem formulation is based on harmonic power flow, in comparison with [123], which used the relative weighted harmonic attenuation factors of the PPF design. [124][125] suggested a continuous and discrete, neural-network-based, optimally designed, single-tuned PPF, respectively, with a single weighted objective function for the multi-objective problem. In [126] and [127], two single-tuned and high-pass PPFs were designed using PSO with multi-objective optimization, THD, cost, and PF. Although the PSO algorithm seems to have better performance than the GA algorithm for different applications, they both require coefficients optimization to improve their global searching capability and computational cost.

The recently developed optimization algorithms were also applied for optimal PPF design. A Bat Optimization Algorithm was developed in [128] to design a set of PPFs as a multi-objective problem. THD, cost, and PF were considered, and results were compared to those obtained from the Simulated Annealing (SA) and PSO-based solutions. In [129], an SA-based, single-tuned PPF was designed to reduce THD and maximise power factor in a simple medium voltage network, but the performance of the SA could be estimated with different algorithms. Different PPF topologies were designed using the Bee Swarm Optimization and Teaching–Learning-Based Optimization algorithms for multiple objectives, as presented in [130] respectively. The work in [131] developed the Ant Colony Optimization (ACO) algorithm for two single-tuned PPFs operating with an active filter to minimise the total cost and THD. Moreover, a study that proposes a modified ACO algorithm for a single-tuned filter is presented in [132]. Single- and double-tuned PPFs were also designed using Bee Colony Optimization in [133]. This considered

THD and reactive power as weighted objective functions. In [134], the Whale Optimization Algorithm was employed for the design and location of PPF. The results imply that the selected PPF and the objective function, which included the power losses minimization only, had a minor impact on harmonic reductions. The Cuckoo Optimization Algorithm was employed to design an optimal PPF with the lowest cost [135]. In [136], three single-tuned filters for different individual harmonic orders were designed and placed for a radial distribution system using the Bacterial Foraging Optimization Algorithm. The objective function comprised power losses and a reduction in investment costs. A Gravitational Search Algorithm was adopted in [137] for the optimal design of a single-tuned PPF in an industrial power network. Class Topper Optimization Algorithm and Slime Mould Optimization Algorithm were also adopted for the optimal design of PPFs, as discussed in [39,40], respectively. In the literature, the newly developed MRFO algorithm has not yet been implemented for the PPF design problem, and the harmonic performance of an optimally designed PPF with variations at the network level has not been investigated. These studies have highlighted the feasibility of a wide range of optimization algorithms for PPF applications and thus would necessitate exploring the feasibility of newly proposed algorithms for such applications.

However, the performance and feasibility of the MRFO algorithm, which was first proposed in [138], has not been investigated for the PPF applications, and an extensive analysis tool for evaluating the optimally designed PPF performance in power distribution networks subjected to uncertainties and inevitable variations has not been addressed. Therefore, the PPF design optimization problem is addressed using the MRFO algorithm, which has shown considerable computational progress, a powerful ability to solve non-linear optimization problems, easy implementation, and relatively fewer parameters that need to be adjusted [139], [140]. Additionally, the most recently proposed optimization algorithms, namely Golden Eagle Optimizer (GEO) [141], Red Fox Optimization (RFO) algorithm [142], and Chameleon Swarm Algorithm (CSA) [143], are adopted for comparison and verifying the superiority of the MRFO algorithm. The prime reason for the adoption of these newly developed algorithms is their similarity in the inspiration and

modelling of hunting behaviours. The performance of each algorithm is analysed to help nominate the most appropriate and efficient algorithm. Moreover, a new method based on an MCS solution is proposed to extensively evaluate the harmonic performance of an optimally designed PPF solution in a power system. This tool can capture the influences of the variations in the system components on the performance of the PPF and the system performance parameters to assure continuous compliance with the standard limits.

4. 3. Optimization Problem Formulation

4. 3. 1. Modelling of the System Equivalent and PPF Circuits

To help formulate the optimization problem and evaluate the performance of the PPF system design using an optimization algorithm, a simple power network, modelled with the equivalent grid and overhead line impedance, is used. This simplified circuit approach was also employed to validate the performance of the optimization algorithms that were applied for PPF design studies [21], [144].

Among the several modelling techniques for the harmonic sources addressed in the literature, the simple and easy-to-implement current source model in the frequency domain, representing a harmonic source by the current sources of the range of frequencies of interest, can still provide an accurate harmonic performance analysis when the interactions between the control system of a harmonic source and the existing background harmonics within the power network are assumed to be negligible [13], [144]. Additionally, the harmonic current source modelling approach has been widely adopted to conduct harmonic performance analysis studies for the optimal design of the PPFs [21], [104]. The equivalent circuit utilised in this work for the PPF design problem is shown in Figure 4-2(a) with the equivalent grid, overhead line, 2nd-order PPF, linear load, and a harmonic source.

Since the system is assumed to be balanced and symmetrical, the DHPF solution is conducted to iteratively compute the corresponding components at each frequency [144]. This enables the application of Kirchhoff's voltage and current laws for fundamental and harmonic frequencies, and then the harmonic indices, such as the THD, power losses, and PF, can be computed.

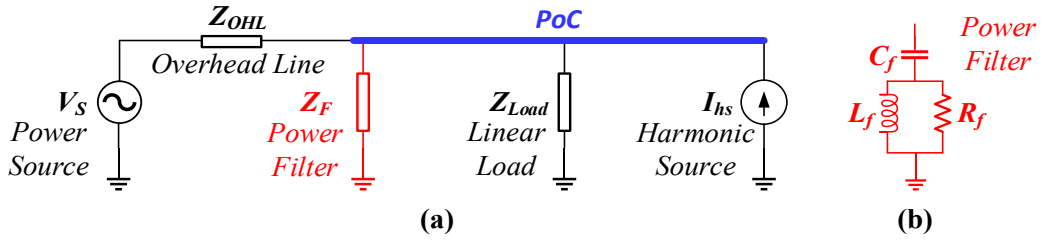

Figure 4-2 (a) Equivalent circuit modelled for problem formulation, (b) 2nd-order high-pass PPF.

To perform the harmonic flow solution for the equivalent power system shown in Figure 4-2, typical harmonic modelling of the system's components must be followed, as defined in [13]. The power grid is represented by a voltage source of 1 p.u. at the power frequency with background harmonics as:

$$V_s(h) = V_s(1) + A_{BGH} \sum_{h=2}^{H} V_s(h) \tag{4.1}$$

Where $V_s(1)$ is the fundamental RMS of the voltage source, $V_s(h)$ is the RMS of the harmonic voltage components, and H is the highest harmonic order of interest. The grid voltage is associated with a Background Harmonics (BGH) factor (A_{BGH}), which will further help evaluate its effect on the PFF harmonic performance.

The harmonic impedance of the overhead line (Z_{OHL}) is modelled as:

$$Z_{OHL}(h) = \sqrt{h}\, R_{OHL} + jhX_{OHL} \tag{4.2}$$

Where R_{OHL}, X_{OHL} are the overhead line's resistance and reactance at power frequency, respectively. $\sqrt{h}$ is included in the model to capture the frequency dependency and skin effect of the resistive part [13].

In comparison to the different high-order PPFs configurations proposed in the literature, the 2nd-order PPFs have a lower number of passive components, implying a lower weight, cost, and size. Thus, they stand out as the ideal option among other high-pass PPFs. This is due to the inherent limitations associated with 3rd-order and C-type power filters, such as the effect of the operating conditions and ambient temperature on the filter parameters, which can lead to significant

parameter variations and, thus, can result in a different system's characteristic impedance. In addition, the complexity of the design is due to the inclusion of more governing equations for the 3rd-order and C-type filters in the design stage [105]. The 2nd-order, damped PPF depicted in Figure 4-2(b) is the most common and favourable type due to its lower cost, high attenuation behaviour, and design simplicity [106]. The equivalent impedance of a 2nd-order PPF (Z_F) is modelled as [130]:

$$Z_F(h) = \left(\frac{R_f \left(hX_{L_f}\right)^2}{R_f^2 + \left(hX_{L_f}\right)^2} \right) + j \left(\frac{R_f^2 \, hX_{L_f}}{R_f^2 + \left(hX_{L_f}\right)^2} - \frac{X_{C_f}}{h} \right) \tag{4.3}$$

Where Z_F is PPF impedance, R_f is PPF resistance, X_{L_f} and X_{C_f} are the PPF inductive and capacitive reactance, respectively.

The parameters of such a PPF are conventionally calculated as follows [13], [100].

$$C_f(\mu F) = \frac{Q_{MVAr}}{\omega_f \; V_{PoC}(1)^2_{kV}} \times 10^6 \tag{4.4}$$

$$L_f(mH) = \frac{1}{\omega_f^2 \; h_f^2 \; C_{f_{(\mu F)}}} \times 10^3 \tag{4.5}$$

$$R_f(\Omega) = Q_F \times \sqrt{{L_f}_{mH} / {C_f}_{\mu F}} \tag{4.6}$$

Where $V_{PoC}(1)$ is the RMS voltage of the fundamental frequency component at the PoC. Q_{MVAr}, ω_f are the reactive power delivered by the PPF and fundamental angular frequency in rad/sec respectively. h_f is the tuning frequency and Q_F is the quality factor of the PPF.

The limitation of this calculation method is that the PPF parameters can use different values to achieve different Voltage THD (VTHD), Voltage Individual Harmonic Distortion (VIHD), Current Individual Harmonic Distortion (CIHD), and TDD. Since this can also lead the grid voltage and the PF to violate the standard limits, the PPF

parameters should be optimally designed with the proposed optimization algorithms to address these challenges and ensure compliance with the standard limits.

To model a linear load for harmonic analysis studies, the rated active power (P_{Load}) and reactive power (Q_{Load}) components are employed to calculate the corresponding load's resistance (R_{Load}) and reactance (X_{Load}) at the fundamental frequency, respectively. The linear load is commonly represented as an assembly of a resistor, connected in parallel with an inductor, and the linear static load harmonic impedance (Z_{Load}) is computed as:

$$R_{Load}(h) = \frac{|V_{PoC}(1)|^2}{P_{Load}} \tag{4.7}$$

$$X_{Load}(h) = \frac{|V_{PoC}(1)|^2}{Q_{Load}} \tag{4.8}$$

$$Z_{Load}(h) = \sqrt{h}\, R_{Load} \;//\; jhX_{Load} \tag{4.9}$$

when the interactions of the power converter control circuit are negligible, the harmonic source can be represented by the current sources in a range of frequencies of interest. Additionally, since the harmonic performance varies with the operating point, as discussed in [145], [146], the harmonic content (I_h) is associated with a factor (A_h), which will further help it to investigate the PPF harmonic performance with the variations in harmonic source emission. The harmonic source emissions can be expressed as:

$$I_{hs}(h) = A_h \times I_h(h) \qquad h > 1 \tag{4.10}$$

By using Kirchhoff's current law at the PoC of the system under the study, the following can be obtained.

$$I_s(h) = I_F(h) + I_{Load}(h) - I_{hs}(h) \tag{4.11}$$

I_s, I_F, and I_{Load} are the current components following through the power lines, PPF, and linear load respectively, and I_{hs} denotes the harmonic source current.

By substituting the harmonic impedance modelled for the system components with the corresponding voltages in Equation (4.11) and considering the grid as a reference node, the following representative equations decoupling fundamental and harmonic components are used for solving the system modelled for harmonic flow analysis shown in Figure 4-3, where $V_s(1)$ is 1 pu $\angle 0°$.

$$\frac{V_s(1) - V_{PoC}(1)}{Z_{OHL}(1)} = \frac{V_{PoC}(1)}{Z_F(1)} + \frac{V_{PoC}(1)}{Z_{Load}(1)} - I_{hs}(1) \qquad for\ h = 1 \tag{4.12}$$

$$\frac{V_s(h) - V_{PoC}(h)}{Z_{OHL}(h)} = \frac{V_{PoC}(h)}{Z_F(h)} + \frac{V_{PoC}(h)}{Z_{Load}(h)} - I_{hs}(h) \qquad for\ h > 1 \tag{4.13}$$

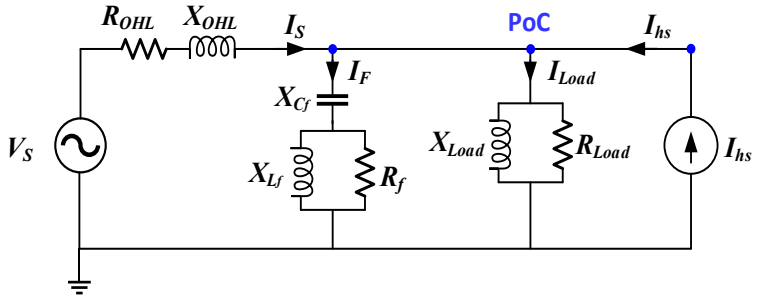

Figure 4-3 Detailed circuit modelled for harmonic flow analysis for PPF design.

4. 3. 2. Decision on the Optimization Objectives and Constraints

The principal goal of installing PPFs in power systems is to reduce harmonic distortions mainly avoiding the maloperation of sensitive loads and increasing the system's hosting capacity for future renewable systems. Additionally, it has been stated in the literature that by eliminating harmonic distortions, network power losses can be reduced and thus system efficiency can be improved. Therefore, the voltage THD at the PoC is considered the major PPF design objective function to be minimised, while other operational aspects such as individual harmonic distortions, the PoC voltage, PF, and some concerns related to PPF parameters requirements are

treated as constraints to be tackled. The objective function is the voltage THD, which is expressed as:

$$Minimum\ Voltage\ THD\ (\%)\ = \frac{\sqrt{\sum_{h=2}^{H}|V_{PoC}(h)|^2}}{|V_{PoC}(1)|} * 100 \tag{4.14}$$

Where $V_{PoC}(h)$ is the RMS voltage corresponding to the harmonic order, and $V_{PoC}(1)$ is the RMS voltage of the fundamental frequency component.

For the PPF parameters design, as for any optimization problem with some inapplicable solutions, some constraints are required to ensure the system performance is kept within the defined limits for the power network and PPF solution. The voltage at the PoC should not exceed the standard limits. The PF at the PoC is required to be corrected to unity. Total and individual voltage and current distortions to be within the defined limits. The PPF quality factor (Q_F) is to obey the design requirements as discussed in [9], [13]. These constraints must be checked during the optimization over each iteration and largely suitable penalties are used to ensure their validity. In this work, the constraints are set according to IEEE Std. 519 [99] as follows.

$$0.95\ pu \leq V_{PoC}(R_f, L_f, C_f) \leq 1.05\ pu \tag{4.15}$$

$$0.9 \leq PF(R_f, L_f, C_f) \leq 1.0 \tag{4.16}$$

$$0.5 \leq Q_F\ (R_f, L_f, C_f) \leq 2.0 \tag{4.17}$$

$$VTHD(R_f, L_f, C_f) \leq 5\% \tag{4.18}$$

$$VIHD(R_f, L_f, C_f) \leq 3\% \tag{4.19}$$

$$TDD(R_f, L_f, C_f) \leq 8\% \tag{4.20}$$

$$CIHD(R_f, L_f, C_f) \leq IEEE\ Std.519 \tag{4.21}$$

The maximum allowed individual odd current distortions defined by IEEE Std. 519 are shown in Table 4-1. However, the IEEE Std. 519 limits the even harmonics to 25% of the odd harmonics. The ratio between the maximum short circuit current and maximum demand load current of the harmonic source is assumed between 20 and 50.

Table 4-1 IEEE Std. 519 current individual distortions limits for systems rated 33 kV.

Harmonic Order	$h < 11$	$11 \leq h < 17$	$17 \leq h < 23$	$23 \leq h < 35$	$35 \leq h$
$CIHD_{max}$	0.02 %	0.02 %	0.02 %	0.01 %	0.01 %

4. 4. Brief Description of the Algorithms Adopted

This section is dedicated to the introduction of the most recently developed algorithms adopted in this work. The inspiration and principal concept of these algorithms are briefly presented.

4. 4. 1. Manta Ray Foraging Optimizer (MRFO)

Despite their appearance, Manta Rays, being one of the world's biggest marine animals, are fascinating creatures. Manta Rays have a flat upper–lower body and a set of pectoral fins that allow them to swim gracefully, like birds. Manta Rays eat plankton, which is primarily made up of minute creatures found in the ocean because they do not have sharp teeth. When Manta Rays go foraging, they use their horn-shaped cephalic lobes to funnel water and prey into their mouths. Modified gill rakers filter the prey out of the water. Manta Rays consume a significant number of plankton. Oceans are thought to be the most abundant source of plankton. Plankton, however, is not equally distributed or consistently concentrated in certain specific regions due to the water dynamics and changing seasons. Manta Rays, interestingly, are adept at locating plankton.

The most fascinating aspect of Manta Rays is their foraging activity. They can move alone, although foraging is commonly observed in groups. These critters have developed a wide range of incredible and clever foraging techniques. The MRFO algorithm is inspired by three foraging strategies, involving chain, cyclone, and somersault foraging strategies, as shown in Figure 4-4. Detailed modelling and

performance evaluation compared to common optimization algorithms are provided in [138].

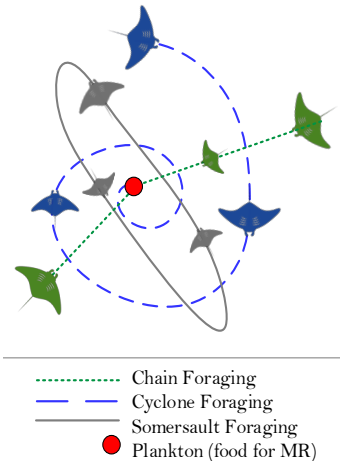

Figure 4-4 Foraging behaviour of the Manta Rays [138].

4. 4. 2. Golden Eagle Optimizer (GEO)

Golden eagles are expert hunters with outstanding vision, speed, and powerful talons, which are capable of catching prey ranging in size from insects to mid-sized animals. Their cruising and hunting are distinct in that they occur in a spiral trajectory, indicating that the prey is usually on one side of the eagle. This allows them to keep an eye on the prey, as well as adjacent stones and shrubs, to choose the best angle of attack. Meanwhile, they scout different areas to see if they can locate better food. The golden eagle's behaviour is always guided by two factors during the flight: the tendency to attack and the propensity to cruise. Golden eagles understand that if they strike very quickly, they may only grab tiny prey that is insufficient to pay for the energy spent in hunting. However, if they keep looking for bigger prey indefinitely, they may exhaust their energy and miss the target.

Golden eagles cleverly strike a balance between these two goals, snatching the best prey possible, using a fair amount of time and energy. They seamlessly transition from a low-attack–high-cruise to a high-attack–low-cruise profile. Each golden eagle begins its hunt by searching for prey by soaring in wide circles at high altitudes inside its domain. When prey is sighted, it begins to move around the perimeter of an imaginary circle centred on the prey. The golden eagle remembers where the prey is, yet it continues to circle.

As the eagle lowers its altitude and approaches the prey, the radius of the hypothetical circle surrounding the prey shrinks. Simultaneously, it looks for better options in the surrounding areas. Golden eagles may occasionally tell other eagles where they discovered the best prey that they have found to date. If the eagle cannot find a better location/prey, it will continue to circle in smaller circles around the current one before attacking the prey. If the eagle discovers a better prey, it will fly in a new circle and forget about the old one. The last assaults are executed in a straight line, as can be observed in Figure 4-5. A detailed modelling and performance evaluation compared to common optimization algorithms are provided in [141].

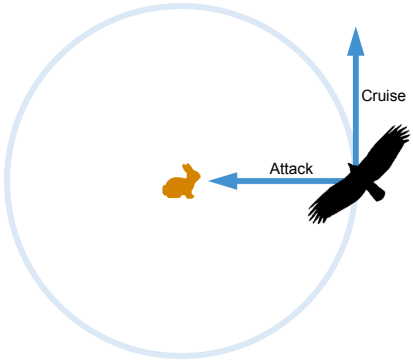

Figure 4-5 Hunting behaviour of the Golden Eagles [141]**.**

4. 4. 3. Red Fox Optimizer (RFO)

The red fox predator's lifestyle and hunting behaviour are rather unusual. It hunts both domestic and wild animals, roaming the landscape, and uses a variety of tactics to confuse victims while crawling, making it a particularly effective predator. The fox's territorial behaviours and the familial relationships between young and adults help adapt to changing situations and, thus, survive.

Red foxes are divided into two groups: those who occupy well-defined areas and those that roam freely. Under the alpha couple's structure, each herd is responsible for a specific region. If the possibility of taking control of another region is good, the young may leave the herd and start their herd. Otherwise, they stay in the family and receive hunting skills from their parents.

The red fox is a skilled predator of small animals. While travelling across the area, the fox seizes any opportunity for food, creeping up to the prey until it is close enough to attack. Figure 4-6 depicts the main hunting attitude of a red fox. When the fox detects prey in the distance, the exploration of territory in search of food, as a worldwide search, is followed by a local search to navigate the environment and move as near to the prey as possible before the attack. A detailed modelling and performance evaluation compared to common optimization algorithms are provided in [142].

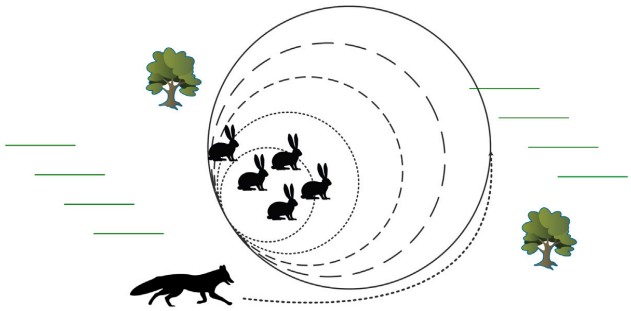

Figure 4-6 Hunting behaviour of the Red Fox [142]**.**

4. 4. 4. Chameleon Swarm Algorithm (CSA)

The dynamic behaviour of chameleons when travelling and foraging for food sources on trees, deserts, and near wetlands served as the idea for this algorithm. This mimics the chameleons' behavioural stages in their quest for food, rotating their eyes to a nearly 360-degree field of view to detect prey, and grabbing prey with their sticky tongues that launch at fast speeds, as shown in Figure 4-7.

Chameleons wander the search space looking for prey in this algorithm. Chameleons utilise their globular eyes to scan a large radius in this manner, using every possible region in the search domain. They utilise their incredibly lengthy and sticky tongues to pick up prey quickly and efficiently when hunting. An adjustable parameter was suggested to help chameleons better explore the search space throughout CSA iterations to achieve a better balance between exploration and exploitation for more dependable performance. A detailed modelling and performance evaluation compared to common optimization algorithms are provided in [143].

Figure 4-7 Hunting behaviour of Chameleons [143]**.**

Broad similarities can be observed among the recently proposed algorithms, and thus it can be said that the MRFO algorithm with the three foraging strategies can sufficiently represent the adopted algorithms. The GEO and RFO algorithms search for the solutions in an orbital manner like the cyclonic behaviour of MRFO searching for plankton. The chain or straight-line approach of the MRFO is quite like the CSA in terms of the chameleon's behaviour in attacking prey, with its sticky tongue. Furthermore, the recently developed MRFO algorithm has been employed in power system planning and control applications [139], [140], showing its powerful ability to solve non-linear optimization problems, easy implementation, and the lower number of parameters that need to be adjusted compared with other common algorithms. Therefore, the different behaviour of the MRFO algorithm and their detailed modelling are discussed as follows:

4. 5. The MRFO Algorithm Modelling

The MRFO algorithm is inspired by three foraging strategies: chain, cyclone, and somersault foraging strategies. The MRFO algorithm that incorporates the different foraging techniques can offer a global searching solution in comparison to the recently developed algorithm. The different searching strategies are modelled as follows:

4. 5. 1. Chain Foraging Strategy

Manta Rays can identify locations with a high intensity of plankton and swim in their direction. Although the best location is not yet known, MRFO presumes that the best solution found to date has a high concentration of plankton for Manta Rays

to approach. Manta Rays move in lines, head-to-tail, and develop a foraging chain. Individuals not only swim toward the plankton, but they also swim toward the Manta Ray in front. Therefore, in every iteration, the best candidate solution found is updated for each Manta Ray. The mathematical model of chain foraging is expressed as [138]:

$$x_i^d(t+1) = \begin{cases} x_i^d + r\left(x_{best}^d(t) - x_i^d(t)\right) + \alpha\left(x_{best}^d(t) - x_i^d(t)\right) & for\ i = 1 \\ x_i^d + r\left(x_{i-1}^d(t) - x_i^d(t)\right) + \alpha\left(x_{best}^d(t) - x_i^d(t)\right) & else \end{cases} \quad (4.22)$$

$$\alpha = 2r\sqrt{|\log(r)|} \quad (4.23)$$

where x_i^d is the location of i^{th} Manta Ray at time *t* in d^{th} dimension, r is a random number between [0,1], α is a weight coefficient, x_{best}^d is the highly concentrated plankton. The position update of the i^{th} member is decided by the location x_{i-1}^d of the $(i-1)^{th}$ member and the position x_{best}^d of the plankton.

4. 5. 2. Cyclone Foraging Strategy

When a group of Manta Rays distinguishes potential plankton in deep water, a long foraging series, one behind the other, develops, and a spiral movement will be formed towards the plankton. The mathematical representation can be further simplified as [138]:

$$x_{rand}^d = L_b^d + r(U_b^d - L_b^d) \quad (4.24)$$

$$x_i^d(t+1) = \begin{cases} x_{rand}^d + r\left(x_{rand}^d(t) - x_i^d(t)\right) + \beta\left(x_{rand}^d(t) - x_i^d(t)\right) & for\ i = 1 \\ x_{rand}^d + r\left(x_{i-1}^d(t) - x_i^d(t)\right) + \beta\left(x_{rand}^d(t) - x_i^d(t)\right) & else \end{cases} \quad (4.25)$$

$$x_i^d(t+1) = \begin{cases} x_{best}^d + r\left(x_{best}^d(t) - x_i^d(t)\right) + \beta\left(x_{best}^d(t) - x_i^d(t)\right) & for\ i = 1 \\ x_{best}^d + r\left(x_{i-1}^d(t) - x_i^d(t)\right) + \beta\left(x_{best}^d(t) - x_i^d(t)\right) & else \end{cases} \quad (4.26)$$

$$\beta = 2\sin(2\pi r) \cdot e^{r\left(\frac{T-t+1}{T}\right)} \quad (4.27)$$

where $x_{rand}^d$is a random spot produced in the predefined search space, β is the weight coefficient, L_b^d and U_b^d are the lower and upper boundaries of the d^{th} dimension, respectively, T is the number of iterations, and r is a random number of (0–1).

4. 5. 3. Somersault Foraging Strategy

In this final foraging behaviour, the location of the plankton is considered as a swing. Every member tends to move and turn a somersault to a different pivot. Consequently, they always renew their spots around the best candidate position determined to date. The mathematical expression can be developed as [138]:

$$x_i^d(t+1) = x_{\ i}^{\ d} + S\left(r_2\, x_{best}^d(t) - r_3\, x_i^d(t)\right), i = 1\ to\ N \quad (4.28)$$

where S is the factor of somersault that indicates the somersault range, and $S = 2$. r_2 and r_3 are two random numbers between [0,1]. N is the population number.

A flowchart illustrating the optimization process for the PPF design using the MRFO algorithm is shown in Figure 4-8.

After providing the required parameters of the studied system, the maximum number of iterations and population size are defined. An initial DHPF solution is performed to help initialise the calculation of the system performance parameters, such as V_{PoC} and PF, and the harmonic indices, such as $VTHD$ and $VIHD$. Then, the MRFO algorithm is performed, following the different foraging behaviours and their locations, and the DHPF solution is performed for each solution with respect to the objective function and constraints. When the solutions are found to violate any

constraint, large penalties are assigned, and the process is repeated without affecting the number of iterations.

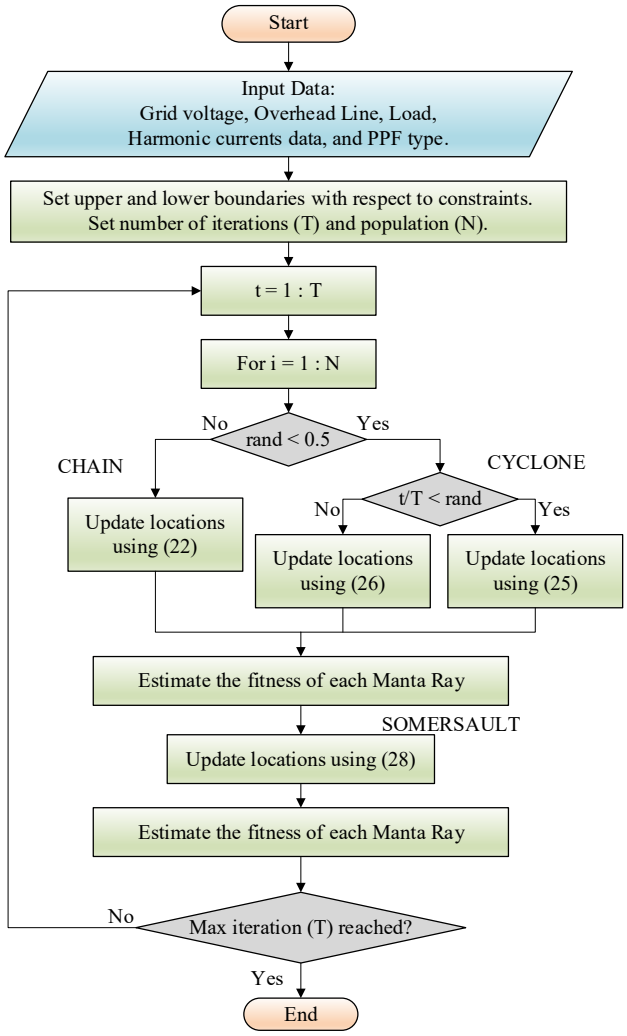

Figure 4-8 Flowchart of the PPF optimization problem using the MRFO Algorithm.

For the optimal design of the PPF parameters ($C_f, L_f and\ R_f$), instead of limiting the search space of the optimization problem to, for example, a unity PF, the single objective function to be minimised is associated with a suitably large penalty factor (pf) for each inequality constraint Equation (4.15) to (4.21), and a reasonably small tolerance for variations in the PPF components' parameters is included. In other words, the objective function becomes (Equation (4.14) + $\sum pf$) and the DHPF is performed for each optimal solution, with the feasibility of the solution checked without affecting the number of iterations. The use of the penalty technique helps

maintain inequality constraints and enables an algorithm to search globally for more feasible solutions in a simple manner. These procedures are followed for all the algorithms adopted in this work. To ensure that the global minimum is reached, the built-in algorithms developed by MATLAB were employed offline as a reference solution.

4. 6. Development of the proposed MCS-based Harmonic Analysis Method

4. 6. 1. Monte Carlo Simulation (MCS)

The stochastic operating characteristics of power distribution networks can lead to a poor realisation and prediction of the actual harmonic performance when deterministic analytical approaches are utilised. Therefore, the MCS approach, which is a computer-based simulation technique that uses probabilistic theory and statistical solutions, is adopted to overcome these issues [22]. The principal idea is to replace the fixed operating point at which the system operates and/or system parameters with a probability function composed of different points, which could be normally or uniformly distributed around a fixed point and determine the system behaviour and response in a semi-dynamic manner. For the power harmonic solutions, the MCS method can help provide statistical insight into the harmonic performance of the PPF to help engineers account for extreme case scenarios related to power system operational uncertainties.

Different probabilistic methods, such as numerical integration, convolution, and semi-empirical methods, were proposed in the literature to assess the harmonics flow with the variations in power networks. In [23], the MCS was developed to investigate the effect of the power network and the harmonic source variations on voltage and current individual harmonic components. Furthermore, a method was developed based on MCS to investigate the impact of the solar PV system and variations in low-voltage customer loads on the system harmonic impedance [101]. The use of probability density functions to represent the variations in the power system components has successfully resulted in efficient harmonic performance analysis, with confidence regarding the extended evaluation process, in comparison to the deterministic approach. The MCS approach was nominated as the most effective

solution to evaluate the stochastic characteristics of the power harmonics considering reasonable variations in the system's variables. Thus, an MCS-based method is proposed in this work to enable the performance of the DHPF solution, and to analyse the performance of the designed PPF. The generalised process of the MCS-based approach that was developed to investigate the PPF harmonic performance is shown in Figure 4-9.

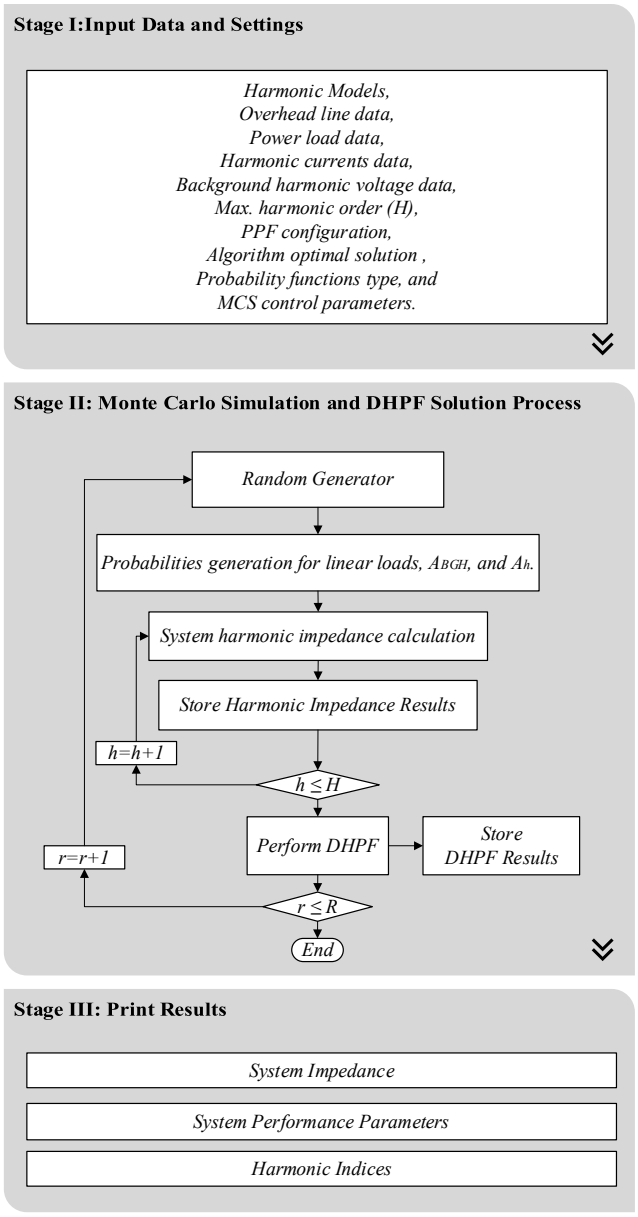

Figure 4-9 Generalised process of the proposed MCS-based method.

The proposed, MCS-based method incorporates three main stages: defining power system data and the MCS parameters, the extended harmonic flow calculations

including the MCS and DHPF solutions, and, lastly, the processing and presenting results. After providing the system specifications and the harmonic models, the harmonic impedance of the system is calculated for the range of frequency of interest. This process is known as a harmonic impedance scan in the frequency domain, and the results are stored in the form of a matrix, which easily enables calling by the next step. The stored harmonic impedance matrices are used to perform the DHPF solution, and the results are simultaneously stored for the corresponding harmonic impedance matrix. The random generator iteratively triggers the probabilities' function generator to produce unique solutions based on the predefined number of samples and distribution function settings. The large matrix that is formed is used to generate results depicting the system performance and enable a statistical representation of the harmonic indices.

4. 6. 2. Origins of Uncertainties

The MCS approach is utilised in this work to extend the evaluation of the harmonic performance of the designed PPF solution in power distribution networks. This helps to consider several variations at the network level such as the linear power load, background harmonics, and harmonic source emissions.

The linear power load, which represents the aggregated low-power loads, requires a stochastic approach to include the uncertainties attributed to the future connection of loads, monthly, daily, and even momentary changes in the existing loads' profile, and the accuracy of the harmonic model of the loads, depending on their nature. The use of a probability distribution function can help include these uncertainties to an acceptable extent [101].

The variations in the harmonic source emissions and their influence on the PPF harmonic performance should also be considered. The harmonic source emissions were shown [145], [146] to vary depending on the amount of power being transferred through the DC link. Additionally, the interactions between the converter control system and the system impedance, and the other harmonic sources, can result in different power harmonic performance profiles [147]. Furthermore, the background/existing harmonics that originate from other harmonic sources that are electrically distant from the PoC can be subject to momentary variations, especially

in rich renewable-based power systems [145], [147]. Another source of uncertainty is imposed by the accuracy of the harmonic analysis solution and limitations of the modelling approaches of the harmonic sources when, for instance, the control circuits and their effects are brought into the picture and required to be considered for accurate harmonic analysis [13]. Therefore, these different operational uncertainties necessitate a sophisticated method to comprehensively investigate the performance of an optimally designed PPF.

The objective of this method is to statistically present the PPF harmonic performance indices when the linear load, background harmonics, and harmonic source emissions are expressed as arbitrary values based on defined distribution functions. The MCS-based method is subject to some input parameters that should be realistically defined for an efficient process and sensible results. These inputs are defined as follows [101]:

- Probability distribution functions in which the system variables are defined and represented can be defined by normal distribution (Gaussian distribution), continuous or discrete uniform distribution functions. Thus, parameters such as mean, standard deviation, minimum, maximum, or discrete values should be defined.
- The number of runs or number of samples over which the MCS is performed should also be carefully defined for extensive performance evaluation. The larger the number of runs, the more the combinations are encompassed in the simulation.

4. 7. Algorithms and PPF Performance Evaluation

In this section, the power system details are presented, the performance of the most recently proposed optimization algorithms is assessed, and the harmonic performance of the designed PPF is evaluated using the proposed MCS-based method, including key uncertainties at the power network level.

For the system depicted in Figure 4-3, the parameters are as follows. At 60Hz, the grid line voltage is 33 kV, and the overhead line impedance is 1.45 Ω resistance and 2.79 Ω inductive reactance per phase. The commonly representative resistive-inductive load is used, with an impedance of 40 Ω resistance and 20 Ω reactance per

phase, accounting for 0.89 lagging PF. The harmonic currents presented in [146] are adopted and assumed to align with the fundamental current since it is the only harmonic source in this study. Additionally, the PPF parameter variations due to the ambient temperature changes are assumed to marginally affect the PPF performance, as discussed in [111]; thus, a tolerance of ± 5% is involved in the constraints to account for these variations and ensure that the harmonic performance is retained within the specified limits. The boundaries of the decision variables are each set from 0 to 100. The p.u. quantities are calculated based on 33 kV voltage and 100 MVA base values. The harmonic source is assumed to operate at the unity power factor at full capacity and has a fundamental current calculated based on the rated power and the nominal voltage.

4. 7. 1. Algorithms Performance Evaluation

Initially, to compare the performance of the optimization algorithms, the harmonic source is assumed to operate at full capacity, the grid voltage is sinusoidal, with no associated background harmonics, and variations in the linear load are excluded. To solve the optimization problem, the algorithms were performed using MATLAB (R2021a) on a computer with a 64-bit Windows 10 operating system, an Intel® Core™ i7 CPU @ 3.60 GHz, and 16 GB of RAM. The number of iterations and populations are set as identical to 100 to establish meaningful results for a comparison between the algorithms. The initial control parameters of each algorithm are shown in Table 4-2. The typical values recommended by algorithms developers are adopted in this work. These initial parameters can have a significant impact on the overall performance of the algorithms that are adopted for a specific application and should be carefully selected to achieve better performance. However, the auto-tuned coefficients (α and β) of the MRFO algorithm are based on the randomization generated in each iteration and can lower the complexity of algorithm development, with no anxiety about the decision made on these coefficients, as can be experienced in the case of the CSA associated with several control parameters.

Table 4-2 Control parameter settings of the algorithms

Algorithm	Parameter	Typical Value
MRFO	α β	Both are randomly generated and subject to iteration no.
GEO	p_a p_c	Increase linearly from 0.5 to 2 Decrease linearly from 1 to 0.5
RFO	ϕ_0 θ	π 0.4
CSA	p_1 p_2 ρ c_1, c_2	0.25 1.50 1.0 1.75

For performance comparison, the recently developed algorithms are independently performed several times, and the PoC voltage THD, which is the objective function, is computed using the DHPF solution for each execution/run. The statistical results of 40 independent runs are presented in Table 4-3. The best and worst solutions obtained from the algorithms for the minimization problem are recorded, while the mean value and standard deviation are computed offline. The average time required by each algorithm to complete a single execution is also shown.

Table 4-3 Statistical comparison of the algorithms over 40 runs

Algorithm	Best Fitness	Mean	Worst Fitness	Std. Deviation	Avg. Time (Seconds)
MRFO	0.8026	0.8031	0.8036	0.00021	52.44
GEA	0.8195	0.8204	0.8214	0.00043	43.25
RFO	0.8031	0.8091	0.8148	0.00278	46.16
CSA	0.9158	0.9186	0.9192	0.00084	41.93

It can be observed that MRFO can efficiently find the best solution, with the lowest deviation among the algorithms. The RFO can also find a close solution to that found by the MRFO but with a larger diversity of optimal solutions around the mean value over several executions. The GEA and CSA are also able to minimise the optimization problem with a relatively small variation, but they seem to be trapped in a locally optimal solution and may require more iterations to reach near-optimal solutions. The MRFO and RFO have better solutions compared with the GEA, while the CSA has the poorest performance among the recently developed algorithms. The poorness of CSA performance can be imputed to the control parameters' settings.

However, the lowest standard deviation value associated with the MRFO, in comparison with other algorithms, indicates its consistency in finding optimal solutions. The optimal solutions found by the MRFO are attributed to the different foraging strategies that widely cover the search space. It is also noticeable that the CSA requires the shortest computational time, followed by the GEA algorithm. In contrast, the MRFO takes a longer time to find the best solution, and this can be justified by the multiple estimations of each Manta Ray's fitness during each iteration.

The convergence rates of the best solutions offered by the adopted algorithms are superimposed, as shown in Figure 4-10. It is obvious that the MRFO algorithm first reached its best solution of 0.8026. This was followed by the RFO algorithm after about 70 iterations. However, the GEA algorithm converged to its best solution of about 0.8195 after 35 iterations, while the CSA algorithm, which has the poorest convergence rate, reached its optimal value of 0.9158 after 80 iterations. A closer look shows that MRFO and RFO algorithms reached superior solutions compared to the GEA algorithm. The different hunting schemes and auto-tuned coefficients associated with the MRFO can be attributed to its better convergence rate, while the GEA and CSA algorithms are anticipated to require more iterations to converge to a better solution.

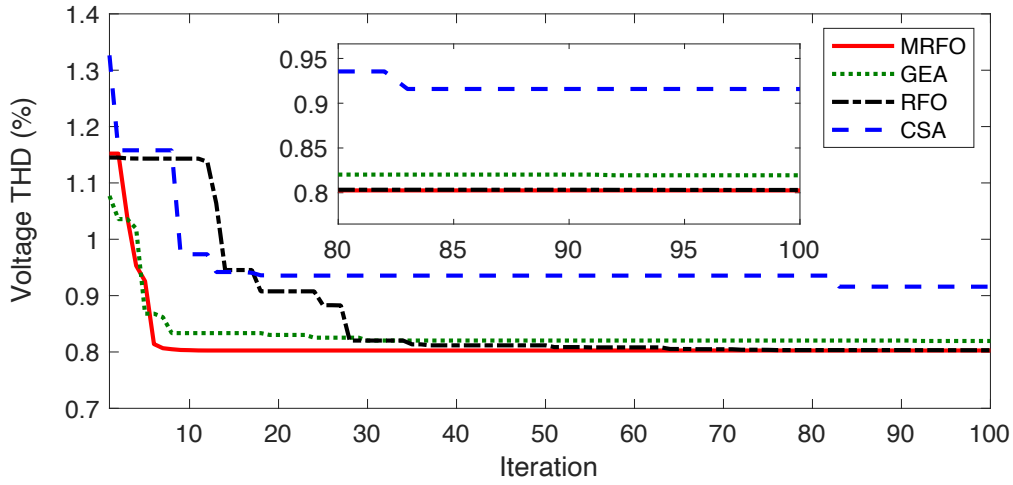

Figure 4-10 Convergence curves of the algorithms.

The decision over the best algorithm performance also depends on the other decision-making factors for which the PPF is designed. The power system performance parameters, such as the PoC voltage, PF, system losses, efficiency, and cost, should be computed for comparison between the different optimization algorithms.

Table 4-4 Comparison of the different solutions proposed by the recently developed algorithms

Parameter (Per phase)	**Uncompensated System**	**Compensated System**			
		MRFO	**GEA**	**RFO**	**CSA**
R_f [Ω]	-	7.083	9.012	7.235	9.364
L_f $[mH]$	-	1.520	1.471	1.496	1.543
C_f $[\mu F]$	-	51.70	52.03	51.89	52.16
$V_{PoC}(h)[pu]$	0.9470	0.986	0.981	0.983	0.979
$VTHD$ [%]	1.9000	0.8026	0.8195	0.8031	0.9158
$Current\ TDD$ [%]	2.5500	1.881	1.948	1.872	1.970
$PF\ at\ the\ PoC$	0.8600	0.9610	0.9648	0.9602	0.9693
$Network\ Losses\ [MW]$	0.1653	0.1411	0.1422	0.1413	0.1425
$P_{F_{losses}}$ $[MW]$	-	0.0297	0.0358	0.0304	0.0371
$Overall\ Cost\ [unit]$	-	23.58×10^3	23.89×10^3	23.67×10^3	24.03×10^3
$Overall\ \eta$ [%]	98.350	98.29	98.22	98.28	98.20
$Hosting\ Capacity$ [%]	87.290	97.06	95.93	96.89	95.04

Table 4-4 shows the system performance before and after utilising the different PPF solutions proposed by the newly developed algorithms. It can be observed that the performance of the uncompensated system appears to violate the standard limits that were mentioned earlier in terms of voltage and power factor at the PoC, and this emphasises the necessity for such a PPF solution. It also presents the optimally designed filter parameters and the system performance with the solutions obtained from the different algorithms. The PF with respect to the line current is computed by Equation (4.29), and network and PPF losses are calculated by Equations (4.30) and (4.31) respectively. The PPF overall cost model including Initial Cost (IC) and Operational Cost (OC) can be approximated by Equation (4.32). The overall system's efficiency and network's hosting capacity are calculated as per Equations (4.33) and (4.34), respectively.

For sinusoidal voltage and current signals, the power factor ($\cos(\emptyset)$) is regularly calculated based on the angle differences between the two waveforms [13], [14]. However, for a distorted system, the power factor calculation should consider a distortion factor that represents the reduction in the actual power factor due to the non-sinusoidal voltage and current waveforms and can be computed as [21], [104]:

$$PF = \frac{\sum_{h=1}^{H} |V_{PoC}(h)||I_s(h)| \cos \emptyset_h}{\sqrt{\sum_{h=1}^{H} |V_{PoC}(h)|^2} \sqrt{\sum_{h=1}^{H} |I_s(h)|^2}} \tag{4.29}$$

Where $\emptyset_h$ is the angle differences between voltage and current components.

$$Network\ Losses = \sum_{h=1}^{H} [I_s^2(h) * R_{OHL}] \tag{4.30}$$

$$P_{PPF_{losses}} = \sum_{h=1}^{H} \left[I_F^2(h) * R_f\right] \tag{4.31}$$

$$Cost = \left[K_1 R_{f_\Omega} + K_2 L_{f_{mH}} + K_3 C_{f_{\mu F}}\right]_{IC} + \left[K_4 P_{F_{kW}} + K_5 Q_{F_{kVAr}}\right]_{OC} \tag{4.32}$$

P_F, Q_F are the PPF fundamental active power dissipated, and reactive power supplied, respectively. The weighting coefficients (K_1 to K_5) are computed as recommended in [148].

$$\text{The Overall System Efficiency } \eta\ (\%) = \frac{P_s - (P_{OHL} + P_{PPF})_{losses}}{P_s} \times 100 \tag{4.33}$$

where P_s is the total active power supplied by or delivered to the power grid, mainly through the harmonic source, and P_{OHL} and P_{PPF} are the active power losses within the overhead line and PPF, respectively.

The ratio of the extreme allowable penetration level of DER systems in MW to the combined load's rated MVA is used to calculate the power network's Hosting Capacity (HC). As a result, with all restrictions fulfilled, the hosting capacity may be equal to the system's instantaneous penetration level and can be expressed as follows [104].

$$\text{Hosting Capacity (\%)} = \frac{\sum_{h=1}^{H} |V_{PoC}(h)||I_s(h)| \cos \emptyset_h}{\sqrt{(P_L + P_{NL})^2 + (Q_L + Q_{NL})^2}} \times 100 \quad (4.34)$$

The rated active and reactive power components of the linear loads are P_L and Q_L respectively. The rated active and reactive power components associated with the nonlinear load, which is the harmonic source, are P_{NL} and Q_{NL}.

It can also be observed from Table 4-4 that the optimally designed PPFs using the recently developed algorithms provided improvements to the system performance in terms of the voltage profile at the PoC, power factor, voltage distortions, current TDD, overhead line losses, and hosting capacity. A marginal deterioration in the overall system efficiency (η) is noticeable when the PPF solutions are employed. This is because of the power losses developed across the PPF's resistance, which build up and result in slightly higher overall system losses. Moreover, the constraints are satisfied in the compensated system with no further risk of violating power system standard limits. However, the compensated system with the PPF designed using the MRFO algorithm has better performance parameters, such as the lowest voltage THD, current TDD, network losses, and a relatively higher PF and hosting capacity in comparison to the other algorithms. The PPF design proposed by the MRFO algorithm can offer the lowest impedance path for the high-order harmonics, and thus results in the lowest voltage THD and current TDD. Improvements in voltage THD and current TDD of about 57% and 26%, respectively, are experienced. Furthermore, the power dissipation of the PPF designed using the MRFO is lower than those obtained from other newly developed algorithms. This is attributed to the lower resistance associated with its optimal solution. It can also be seen that the overall cost corresponding to the solution

offered by the MRFO algorithm is the lowest among the algorithms. This can be justified by the smallest inductive and capacitive components associated with its solution. Moreover, the solution proposed by the MRFO algorithms is associated with the best improvement for the network's hosting capacity by roughly 11%.

To validate the harmonic performance of the PPF with the parameters proposed by the MRFO algorithm, the simplified power system depicted in Figure 4-3 was implemented in the IPSA simulation environment that mimics a real power system and enables harmonic flow analysis studies. By adopting the harmonic currents presented in [146], the PoC voltage spectra of the uncompensated and compensated system are depicted in Figure 4-11. The lower impedance of the PPF at high frequencies has significantly damped the high-order voltage harmonics, while a minor amplification of the low-order harmonics occurs due to the resonance developed by the PPF capacitive component. The optimal solution proposed by the MRFO algorithm is chosen as the best solution and will be used to investigate the performance of the developed MCS-based method for harmonic performance analysis.

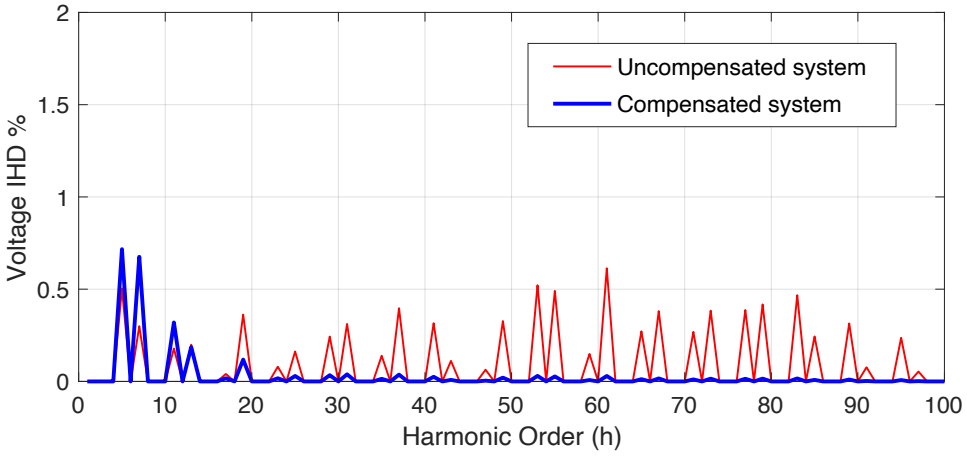

Figure 4-11 The PoC voltage spectra prior to and after installing the PPF proposed by the MRFO algorithm.

4. 7. 2. PPF Performance Analysis Including Uncertainties

Despite its computational time burden, the MRFO algorithm showed superior performance compared to the recently developed algorithms, with potentially better

solutions in most cases. Therefore, in this section, the PPF harmonic performance is extensively analysed based on the optimal solution offered by the MRFO algorithm. When this designed PPF is implemented in a real power system, subjected to several operational variations and unpredictable state changes at the network level, the harmonic performance must be extended to account for these uncertainties and assure compliance with standard limits for various scenarios. To achieve this aim, the MCS-based method is developed by incorporating the DHPF solution to compute the system harmonic impedances and indices in a semi-dynamic approach and statistically present them to ensure continuous compliance with the standard limits.

4. 7. 2. 1. Handling Uncertainties Using the MCS-based Method

In this work, the harmonic source emissions were illustrated in [146] to vary with the operating point. Additionally, the assumption of electrically distant harmonic sources connected to the grid and their variations due to their unpredicted renewable sources should be considered as time-varying background harmonics. Therefore, the existing harmonics of the grid and the harmonic emissions of the harmonic source are associated with the factors A_{BGH} and A_h, respectively, as shown in Equations (4.1) and (4.10) and can be represented in a continuous uniform distribution function to enable the MCS solution. The background voltage spectrum is reasonably assumed, and details are presented in Table 4-5.

Table 4-5 Odd individual background harmonic voltage components

Harmonic Order	$\mathbf{5 \leq h < 17}$	$\mathbf{17 \leq h < 35}$	$\mathbf{35 \leq h < 55}$	$\mathbf{55 \leq h < 75}$	$\mathbf{75 \leq h < 95}$
Harmonic Contents	0.02 %	0.02 %	0.02 %	0.01 %	0.01 %

The MCS parameters are shown in Table 4-6. The linear load, which is composed of active and reactive power components calculated in p.u., is also modelled with normal distribution functions, modelled by normal distribution defined with specific mean values (μ) and standard deviations (σ), to explore their impact on the harmonic performance with the PPF solution. The overhead line impedance, however, is assumed to be constant and not subject to variations.

Table 4-6 The MCS distribution functions and parameters settings

Characteristics	Distribution Functions	Parameters
$A_{BGH}(p.u.)$	Continuous Uniform	min=0.50, max=1.10
$A_h(p.u.)$	Continuous Uniform	min=0.50, max=1.10
$P_{load}\ (p.u.)$	Normal	$\mu = 1, \sigma = 0.15$
$Q_{load}\ (p.u.)$	Normal	$\mu = 1, \sigma = 0.15$

The program is encoded and implemented in MATLAB to solve the problem. Based on the input data and MCS settings, the MCS process starts by generating the profiles of the linear load and harmonic distortion factors (A_{BGH} and A_h). The system harmonic impedance is first calculated, using the provided harmonic models of the system components over the range of frequencies of interest (H), which is equal to 100 harmonic orders. The DHPF solution is applied using the stored impedance that were calculated, and its corresponding harmonic indices are computed and stored. The MCS-based method will proceed with this functionality until it reaches the maximum number of samples/runs (R). Generally, the number of samples should be large enough to include more solution combinations in the MCS. Thus, the number of samples of the MCS in this work is set to 3000 to include more possible variations, represented by the probabilistic distribution functions. To lessen the overall computational complexity, the stored results are treated independently for each run to compute the performance parameters and harmonic indices more easily.

4. 7. 2. 2. System Performance Analysis

The results of the complete application of the developed method are presented and discussed in this subsection. Firstly, to investigate the impact of the different operational uncertainties on each system component, the harmonic impedances are computed independently using the developed MCS-based solution. The impedance of the PPF system with the MRFO optimal solution is initially performed. Then, the driving point impedance seen from the PoC, including only the variation in the linear load without the PPF solution, is also separately computed for the range of frequencies of interest (i.e., from the 1st to 100th harmonic order). To show the impact of the linear load variations on the overall system impedance, the harmonic impedance seen from the PoC is combined with the PPF impedance (i.e., the PPF

is connected in parallel with the linear load and the overhead line impedances), and the MCS is performed to calculate the total harmonic impedance, taking the linear load variations into account.

The resultant harmonic impedances, performed using the developed MCS-based approach, are depicted in Figure 4-12. It is worth mentioning that the plots include the average, maximum, and minimum values, while all other values lay in the area between the max. and min. impedance plots are not shown for simple visualisation. The analysis of these impedances can be interpreted by the mean and standard deviation values.

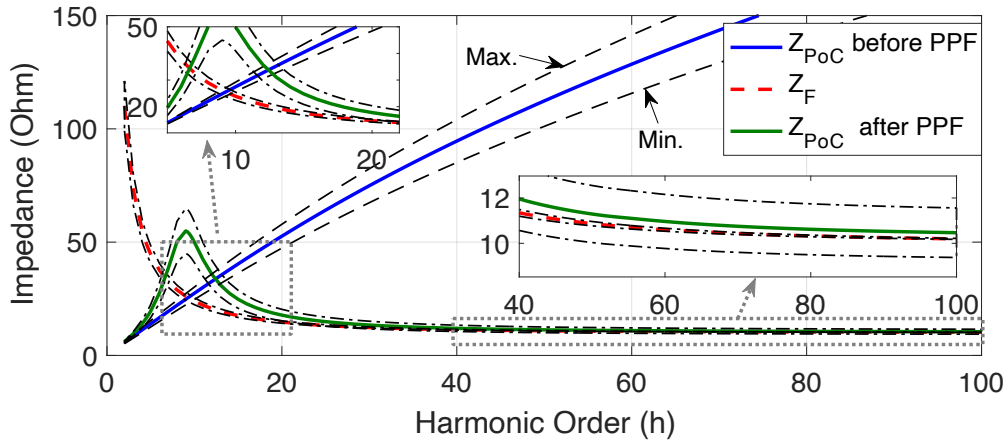

Figure 4-12 System harmonic impedance variations performed using the developed MSC-based method.

The inductive-resistive linear load harmonic impedance linearly increases with the frequency due to the harmonic model, which represents the inductive element with a reactance multiplied by the harmonic order. Moreover, the frequency dependency associated with the resistive part to accommodate the skin effect shows a marginal damping effect at higher frequencies. The impact of the linear load variations on the driving point impedance seen from the PoC (Z_{PoC}) is pronounced at higher harmonic frequencies at which the impedance increases by up to 18%, while smaller variations can be observed at lower frequencies of 6% at the 10th harmonic order. The 2nd-order damped filter impedances (Z_F) corresponding to the MRFO optimal solution are also depicted in Figure 4-12. This indicates the superiority of the 2nd-order high-pass filter selected to eliminate the high-order harmonics and the

performance of the optimization algorithm in generating an optimal solution with a significantly low impedance path for the high-frequency harmonics to achieve the aim of this study.

When the PPF is connected at the PoC, the system impedance (Z_{PoC} after PPF) seen from the PoC is also plotted, as in Figure 4-12. It is evident that the PPF has altered and significantly reduced the system impedance over a wide range of high frequencies. However, the capacitive element of the PPF interacts with the inductive parts of the linear load, overhead line, and the filter itself, and thus resonance results at lower frequencies. The inclusion of the uncertainties of the linear load is considered and roughly 37% variation in the resonance peak is observed, while a small variation in the resonant point of 14% is observed. At higher frequencies, the difference between the maximum and minimum impedance plots is about 17%, which is caused by the uncertainties associated with the linear load.
The harmonic impedance of the system seen from the PoC after the PPF installation indicates a considerable attenuation effect on the harmonic voltage components, since the PPF will provide a low impedance path for high-order harmonic currents, even with the uncertainties imposed by the linear load.
The proposed MCS-based method also helps in investigations into the PoC voltage harmonic components variations with the expected variations in the harmonic source emissions and the grid background voltage harmonics, since it incorporates the DHPF solution, enabling the calculation of harmonic indices. The stored system harmonic impedances after the installation of the PPF (Z_{PoC} after PPF), including the linear load variations, are used to investigate their influence on the PoC voltage harmonic distortions.
The different resultant voltage spectrums obtained from the developed MCS-based DHPF solution are shown in Figure 4-13. The maximum and minimum resultant spectra are shown for illustration. The resulting minor amplification effect on the low-order harmonic components is attributed to the variations in the harmonic resonance due to the PPF capacitance that interacts with the variations in linear load. It is evident that, by including the uncertainties, each harmonic voltage

component is maintained well below the standard limit, and the risk of violating these standard individual limits has been alleviated.

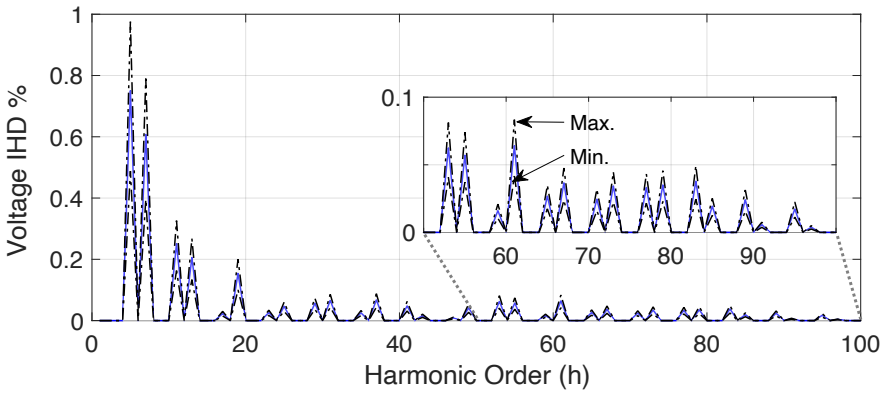

Figure 4-13 Voltage distortions variations at the PoC using the proposed MCS-based method.

The system parameters obtained from the developed method for the uncompensated and compensated systems can be presented by the normal distribution, as shown in Figure 4-14(a–e) and Figure 4-14(f–j), respectively. The uncompensated system exceeds the voltage and PF limits at the PoC, while a larger-voltage THD can be experienced at the PoC and would limit further renewable connections at this point. In contrast, the compensated system performance parameters with the MRFO-based PPF solution continuously comply with the standard limits in terms of voltage and PF. It is obvious that the PPF solution would effectively maintain the PoC voltage and PF within the limits of 0.95 to 1.05, and 0.9 to 1, respectively. This can be attributed to the variations in the load's impedance and, consequently, the voltage across the line impedance.

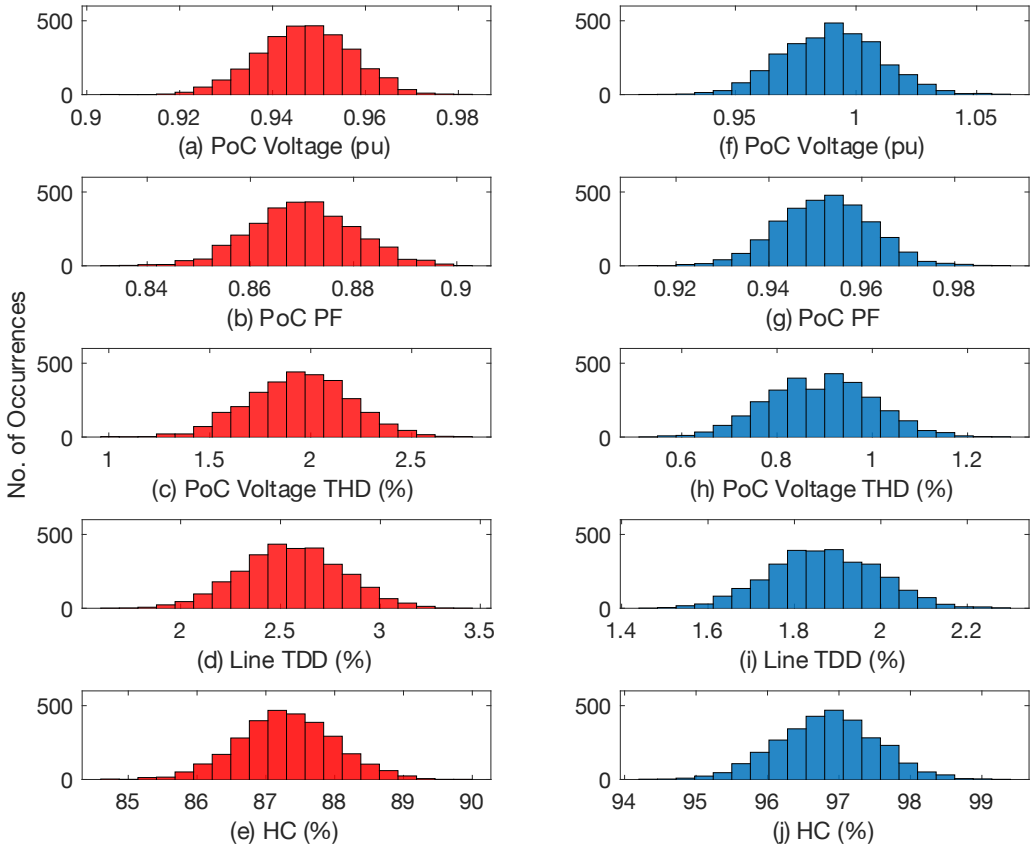

Figure 4-14 System performance parameters obtained from the developed MSC-based method prior to (left) and after (right) installing the PPF proposed by the MRFO Algorithm.

Additionally, the compensated system has a significantly lower voltage THD at the PoC and it is continually maintained well below the IEEE Std. 519 limits. The extreme values that were obtained are assumed to be the worst-case scenario performance parameters. It is observable that the PPF can improve the voltage THD and current TDD for the worst-case scenario by 54% and 30%, respectively. This is attributed to the variations in the apparent power of the linear load and the harmonic source. Additionally, an improvement in the network's hosting capacity of 10% can also be noticed for the worst-case scenario, which provides a more accurate estimation according to the proposed PPF solution.

The MSC-based solution helps provide better insight into the PPF performance in comparison to the deterministic analytical approach shown in Table 4-4. The results provided by the proposed MCS-based method indicate that the optimally designed

PPF would eliminate any potential risk of high-order harmonics. This harmonic protective measure can also help increase the hosting capacity of the power distribution network for further penetrations of the PE-based renewable systems, which are widely acknowledged as harmonics-producing systems.

4. 8. Summary

In this chapter, a literature review of the optimal design approaches and optimization algorithms implemented in this area was presented. The formulation of the optimization problem and decision on the objective function and constraints were discussed. The recently developed MRFO algorithm was implemented for a 2nd-order high-pass PPF parameters design, and an analytical method based on the MCS was proposed to evaluate the harmonic performance of an optimally designed PPF, with variations in the power network. The most recently developed optimization algorithms, namely GEO, RFO, and CSA, were employed for comparison and superiority verification. A thorough harmonic performance analysis study of the designed PPF using the developed MCS-based approach to include the variations in the linear loads, changes in background harmonics, and different harmonic source emissions were conducted, and the results were discussed. The results imply that the optimally designed PPF can effectively attenuate the high-order harmonics and improved the system performance parameters over different operating conditions to continually comply with the standard limits. The proposed MCS method showed that the optimally designed PPF reduced the voltage and current distortions by roughly 54% and 30%, respectively, and improved the network hosting capacity by 10% for the worst-case scenario.

Chapter 5. Harmonic Distortions Estimation using Artificial Neural Networks

This chapter explores the feasibility of the Artificial Neural Network (ANN) for estimating the true harmonic distortions of a grid-connected power converter application with multiple harmonic sources connected, changes in the system's characteristic impedance, and the intermittent nature of renewable resources. A survey of the ANN-based systems utilised for power harmonic distortions estimation is conducted. An improved harmonic distortions estimator is proposed and developed based on voltage, current, and location-specific signals. A simple power system including several renewable systems and events at the power network level is simulated to investigate the variations in the harmonic performance of a solar Photovoltaic (PV) power inverter. The proposed system training and prediction performance are presented. Later, the proposed estimator is validated in the IEEE 34-bus test feeder with established harmonic sources.

5. 1. Background

The international upward trend in utilising more sustainable energy systems in the power sector has mainly been driven by greenhouse gas emissions reduction schemes and growing energy consumption. A possible measure in today's power networks is the integration of more environmentally friendly technologies such as solar PVs, Wind Turbines (WT), and Electric Vehicles (EVs), which emerge into the power grid through Power Electronics (PE) devices. The unpredictability of Renewable Energy Sources (RES) besides the switching behaviour of the PE-based power conversion systems can endanger the quality of supply of the power system [11]. Power harmonics, which are one of the crucial topics of the power quality problems, can lead to undesirable effects on the power system such as increased power losses, overheating and vibration of power transformers and motors, degradation of PF, and maloperation of protection systems [13]. These harmonics-related financial and technical consequences have stressed the necessity for effective measures maintaining harmonic distortions at lower possible levels and ensuring compliance with the standard limits like the IEEE Std. 519.

When multiple harmonic sources are connected to a grid and harmonic distortions violate the standard limits, the grid operators must assign the offending harmonic source for enforcing compliance with the standard limits to improve the power quality and reduce their effects. However, the harmonic emissions of a grid-connected PE-based system can differ from the harmonic performance provided by the vendors and the assessment of the output current distortions of these power converters via conventional metering equipment cannot reflect the true harmonic emissions [147], [149], [150]. This can be attributed to the interactions between the control circuits of the power converters, the network impedance, and background harmonics caused by other existing harmonic sources [101], [102], [151], [152]. Furthermore, the presence of capacitive elements of the passive filters at the converter level and PFC capacitors at the network level can trigger resonances amplifying the existing harmonic components in the network and influencing the harmonic performance of a grid-connected power converter, and thus misestimation of actual harmonic source contribution can occur [10], [153]. Besides, the intermittent nature of the RES resulting in different operating conditions has a significant impact on the harmonic performance of such harmonic sources [145], [154]–[156].

To clarify the problem, Figure 5-1 depicts a power distribution network including the grid equivalent circuit, PE-based renewable power sources, PFC capacitors, and a linear load. The time-variant currents of the PE-based applications (i.e., $i_{PV}(t), i_{WT}(t),$ and $i_{EV}(t)$) are composed of fundamental and harmonic components being injected into the power grid at the Point of Common Coupling (PCC). The power grid is usually associated with background harmonics originating from other electrically distant harmonic sources that could be amplified by resonances introduced by the PFC capacitor. Due to the interactions between the harmonic sources and the state changes at the power network level, the resulting harmonic distortions calculated only from a harmonic source output current would not accurately reflect its actual harmonic distortions.

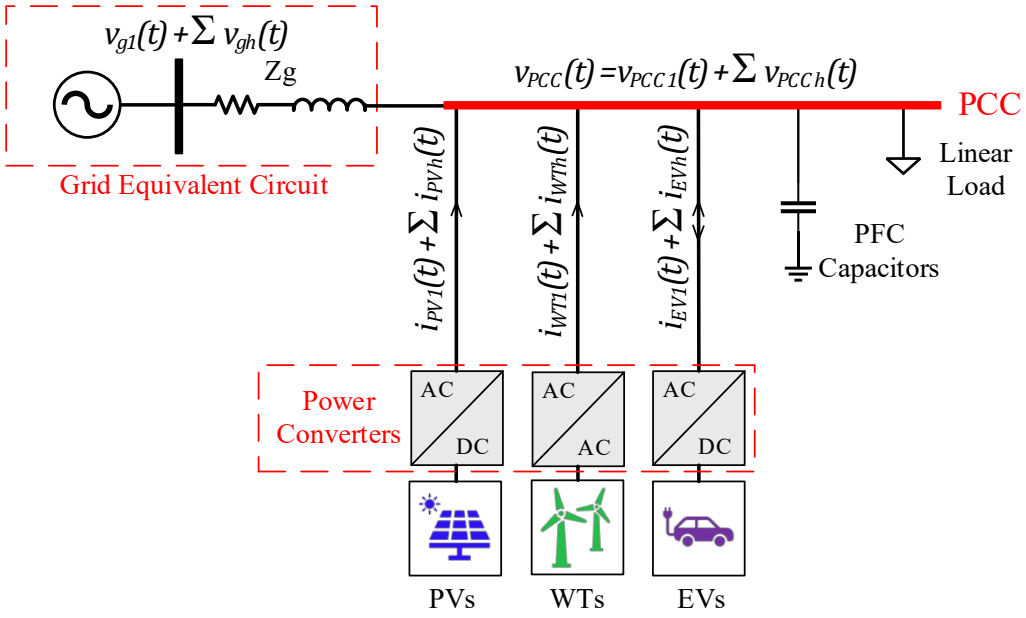

Figure 5-1 Illustration of modern power distribution systems.

The power systems operators and users are, therefore, required to extensively monitor the harmonic performance of each grid-connected system over different operating conditions to identify its actual contribution to the harmonics-related problems. However, the true harmonic distortions can only be obtained when the voltage at the PCC is pure-sinusoidal, which is impractical since it requires the disconnection of all other potential nonlinear loads/harmonic sources and reducing the grid impedance to zero [147], [150], [157].

5. 2. Previous Work

There have been several research works addressing the estimation of harmonic distortions in the literature. For instance, the classical power system analysis-based solutions such as the harmonic impedance estimation [158], active and reactive power flow of harmonics [159], [160], critical impedance measurement [161], and the stochastic approach for the harmonic estimation [162]–[165]. Several recent publications have also attempted to address the harmonic distortions estimation problem as in [166]–[169]. These methods, however, require prior knowledge about

the system components for accurate harmonic models and network configurations to accurately calculate the harmonic distortions.

The development of AI-based systems such as ANN has motivated many researchers in the power harmonics area due to its simple implementation, learning and generalisation capability, and wide applications in several engineering fields. The ANN systems were adopted in several studies dedicated to PE harmonic performance estimation [170] and active power harmonic filters [171], [172]. Furthermore, an ANN system was developed to evaluate the fundamental and harmonic components deviations in a power network requiring parallel processing operation for its high computational burden [173]. An intelligent harmonic estimating method based on ANN for power harmonics sources was proposed in [174]. This solution is based only on distorted voltage and current measurements, and it resulted in a relatively high error in estimating high-order harmonics. A single harmonic source power system was considered with neglecting the impact of background harmonics, which can adversely affect the distortions estimated.

A Multi-Layer Perceptron (MLP) ANN system in [150], Recurrent Neural Network (RNN) system in [175], and Echo State Network (ESN) system in [176] were developed to estimate the true harmonic distortion of a nonlinear load. The proposed approach relied only on measured distorted voltage and current signals and considered several time-invariant nonlinear loads. A similar method considering multiple ANN for each harmonic component with prior knowledge of the nonlinear load specifications to estimate the harmonic distortions through equivalent coefficients was developed in [177]. A method based on the Nonlinear Auto-Regressive eXogenous (NARX) neural network system was developed for the estimation of the power harmonic distortions [178]. However, these proposed approaches do not capture the variations in the nonlinear load under the estimation, which can result in a different harmonic performance, and thus they can lead to inaccurate prediction of the harmonic distortions for different operating conditions in the prediction stage.

On the other hand, an approach capturing the impact of time-varying nonlinear loads on harmonic performance was proposed in [179]. The work includes several nonlinear loads, but the true harmonic distortions were not considered and thus can inaccurately evaluate the nonlinear loads' contribution to the harmonic voltage distortions at the PCC. A power harmonic predicting system for solar PV systems was developed in [180]. The system only predicts the THD for various operating conditions and no attention was paid to the variations and uncertainties at the network level, which should be considered for accurate and reliable harmonic distortions estimation of a specific application. A summary of the established systems in the literature and proposed harmonic distortions estimator with requirements, features, and limitations are shown in Table 5-1.

However, there has been no such a power harmonic distortions estimator that considers the impacts related to the different operating conditions caused by the variations in the renewable resources, the interactions with other harmonic sources and system components, and power network impedance state changes. Therefore, this research work aims to fill the gap by developing an improved harmonic distortions estimator based on an ANN system considering the location-specific data, which will help to predict the harmonic distortions over a wide range of operating conditions. It is anticipated that the proposed system will accurately estimate the true harmonic distortions of a grid-connected power converter operating with multiple harmonic sources considering the variations in harmonic emissions due to the nature of intermittent renewable resources, effects of PFC capacitors, interactions with other harmonic sources, and the system impedance changes. The proposed system will be validated using the IEEE 34-bus test feeder with different harmonic sources obtained from a test field.

Table 5-1 A Summary of the ANN-based methods for estimating the power harmonic distortions.

Reference	Applications	ANN	Required Data for Training	Features/Limitations	
				True THD	Variations in Operating Conditions
[150]	Nonlinear load	MLP	• PCC distorted voltage. • Delayed PCC distorted voltage. • Nonlinear load Current.	✓	✗
[175]	DC Drives	RNN	• PCC distorted voltage. • Delayed PCC distorted voltage. • Nonlinear load Current.	✓	✗
[176]	AC Drives	ESN	• PCC distorted voltage. • Nonlinear load Current.	✓	✗
[177]	Nonlinear load	MLP	• PCC distorted voltage. • Nonlinear load Current.	✓	✗
[178]	AC Drives	NARX	• PCC distorted voltage. • Nonlinear load Current.	✓	✗
[179]	Nonlinear loads	AWNN	• PCC distorted voltage. • Nonlinear load Current.	✗	✓
[180]	Solar PV Inverters	MLP	• Solar irradiance. • THD of the inverter Current.	✗	✓
[157]	Renewables Applications	MLP	• PCC distorted voltage. • System distorted Current.	✓	✗
Proposed	Renewables Applications	MLP	• Solar irradiance or wind speed profile. • PCC distorted voltage. • System distorted Current.	✓	✓

5. 3. Harmonic Distortions Estimator Development

5. 3. 1. Operation Description of the Proposed Estimator

The ANN systems have been widely used as an alternative modelling method for power system applications. In this work, ANN is implemented to predict the actual injected harmonic current of a specific harmonic source without disrupting the

operation of the grid, connected loads, and power sources. A single-line diagram comprising the grid equivalent circuit with background harmonics, PFC capacitors, other linear and nonlinear loads, and the ANN-based harmonic distortion estimator is shown in Figure 5-2.

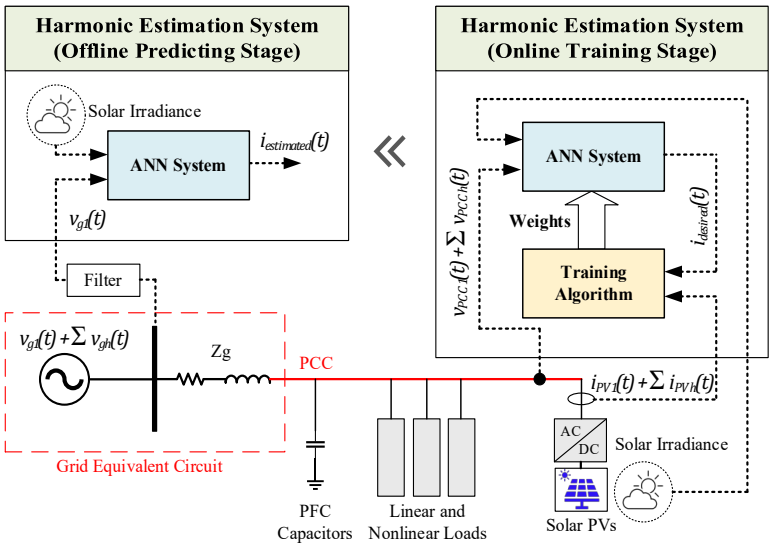

Figure 5-2 Configuration of the proposed harmonic distortion estimator.

The distorted current of the PV inverter, $i_{PV}(t)$, under the estimation along with the currents of other nonlinear loads/harmonic sources and background harmonics will consequently result in a distorted grid voltage, $v_{PCC}(t)$, and thus the $i_{PV}(t)$ is affected by its actual and grid supply harmonic components. The ANN-based harmonic distortions estimator is trained to capture the nonlinear characteristics of the system under the study and help model the admittance between the grid and the harmonic source.

The location-specific data such as solar irradiance and wind speed have a significant impact on the harmonic performance of solar PV systems [145] and wind turbine power inverters [154], respectively. Therefore, when operating condition-related data is provided to the ANN-based estimator with the instantaneous distorted PCC voltage signal, an accurate estimation of the harmonic source contribution can be attained over different operating conditions. This proposed method can also be

applicable for nonlinear loads when such a correlation between the operating conditions and the output harmonic distortions can be established.

The weight and threshold coefficients of the ANN are optimised with the aid of a training algorithm that compares the measured instantaneous current signal and the desired signal from the ANN to minimise the system performance error. After this online training stage, the offline ANN is fed with the solar irradiance of interest and a harmonics-free signal of the grid voltage, $v_{g1}(t)$, or mathematically generated pure sinusoidal waveform to predict the output signal, $i_{estimated}(t)$, that attributes to the actual distorted current of the harmonic source when it is connected to a harmonics-free infinite power source with a zero impedance.

5. 3. 2. ANN Architecture and Training Algorithm

A simple feedforward multilayer perceptron ANN system consisting of an input layer, at least a hidden layer, and an output layer is shown in Figure 5-3.

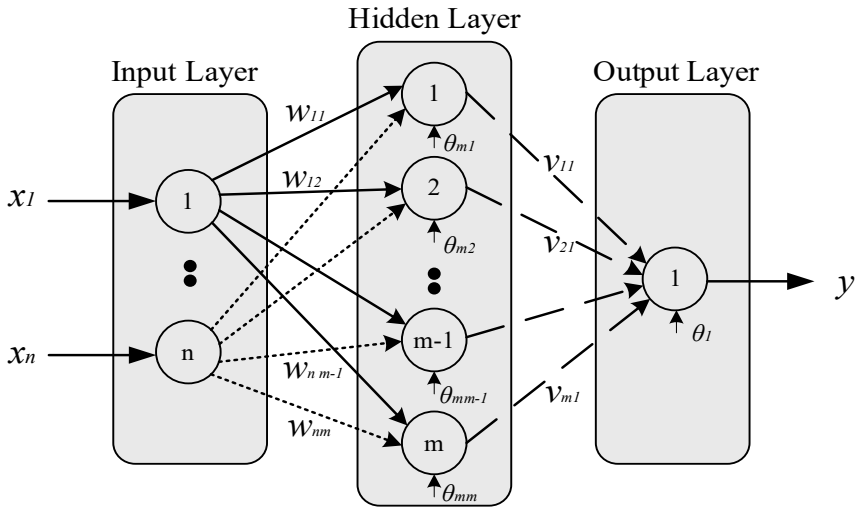

Figure 5-3 Generalised architecture of the MLP-ANN system.

This structure is adopted for the harmonic distortion estimator developed in this work due to its simple implementation and wide utilisation in practical applications. The course of passing the inputs to the output through the ANN is known as feedforward propagation. Each input is fed to each neuron in the hidden layer after applying the corresponding weight, w_{nm}, and the same process applies to the hidden output to the output layer through the related weights, v_{m1}.

The decision of each neuron in the hidden and output layers is governed by an activation function to determine its output. In this work, the ANN system employs the sigmoid and linear activation functions for hidden and output layers' neurons, respectively. Therefore, the neurons' outputs (h_j) of the hidden layer and the output (y) of the output layer are subject to the following governing equations [181]:

$$h_j = \left(1 + e^{-(\sum_{i=1}^{n} w_{ij}\, x_i + \theta_j)}\right)^{-1} \quad j = 1,2,\ldots,m \tag{5.1}$$

$$y = \sum_{j=1}^{m} v_{ij}\, h_j + \theta_1 \qquad i = 1,2,\ldots,m \tag{5.2}$$

Where n is the number of the input signals x_i, w_{ij} is the weight of each connection between the input layer and the hidden layer, θ_j is the threshold of each hidden layer neuron. v_{ij} is the weight of each connection between hidden and output layers, and θ_1 is the threshold of the neuron in the output layer.

Generally, it is challenging to anticipate the fastest training algorithm for a given problem. This is because of various factors including the problem complexity, the data volume in the training set, the number of weights and biases of a certain structure, the performance error goal, and the task that the network is used for such as pattern recognition or function approximation [182]. Although several biologically inspired optimization algorithms have been adopted in many applications to train ANNs, the widely utilised and well-developed Levenberg-Marquardt training algorithm known for its reduced computational effort and high convergence rate is used in this work.

5. 3. 3. ANN Specifications and Performance Criteria

For a given number of inputs and outputs, modelling nonlinear functions using ANNs is significantly affected by the number of hidden layers and their neurons. The number of neurons has a direct effect on the convergence rate, execution time, and performance error of the ANNs [181]. In the literature, the Mean Squared Error (MSE) method is commonly used to estimate the ANN performance error.

The instantaneous measured voltage and current signals are discrete based on the sampling time of the digital metering equipment or simulation environment. Since the ANN in this work has a single output ($y = i_{desired}$), the error for the training algorithm to deal with is expressed as:

$$Training\ Error_{MSE} = \sum_{i=1}^{N} \frac{(i_{desired} - i_{measured})^2}{N} \tag{5.3}$$

Where N is the number of samples in the training data. This is to achieve the best fitting with the measured signal over each epoch.

To generate the required data to train the ANN-based harmonic distortion estimator and evaluate its performance, a simple power system composed of multiple harmonic sources and different events at the power level is simulated as follows.

5. 4. Simple Power System under the Study

5. 4. 1. Description of the Simulated Power System

A single-line diagram of the three-phase simple power system under the study is depicted in Figure 5-4. The system includes a power grid modelled by an equivalent voltage source behind an impedance, two grid-connected solar PV systems, a wind turbine, a nonlinear load, and PFC capacitors. The system specifications are presented in Appendix 2. The power system is simulated using Simulink/MATLAB to investigate with different power events the harmonic performance of the PEs-based applications and their interactions with other system components. The three-phase system is assumed to be balanced and symmetrical, and therefore phase A measurements of the voltage and current and their corresponding distortions are presented.

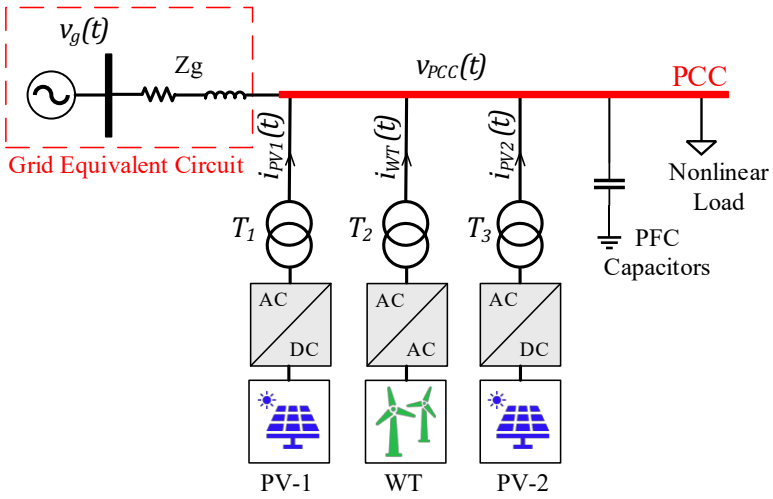

Figure 5-4 Schematic of the simulated power system.

5. 4. 2. Harmonic Performance of the Simulated System

Since the solar PV-2 system is being under the estimation, the solar PV-1 and wind turbine systems operate in steady-state during the simulation time, solar irradiance of 1000 W/m^2 at a constant ambient temperature of 35℃ is used for the solar PV-1 system, and a 12 m/second wind speed is used for the wind turbine system.

Referring to Figure 5-4, to investigate the effects of the potential changes at the network level and the variations in the solar irradiance on the harmonic performance of the solar PV-2 system and the PCC voltage, several events at the power network and two solar irradiance profiles are included in the simulation. At 0.5 seconds the nonlinear load increases by 50%, the grid impedance (Z_g) experiences an increase of 30% at 1.25 seconds, and the PFC capacitor is disconnected at 1.75 seconds. Two distinct solar irradiance profiles of the solar PV-2 system are also considered. Profile 1 involves a gradual decline in solar irradiance at 1 second, from 1000 to 800 W/m^2, while Profile 2 has a downward trend over the simulation time starting from 1200 to 400 W/m^2. The ambient temperature is maintained constant at 35℃ for all the cases.

Additionally, taking the advantage of such a simulation tool can help determine the accurate and true harmonic distortions of a certain PE-based system under the estimation when a sinusoidal voltage is delivered at the PCC, which can only be

achieved by disconnecting all other harmonic sources and reducing the grid impedance to zero, which is not possible in real power systems. The harmonic performance of the solar PV-2 system obtained from this process will be later compared with the predicted results from the ANN-based harmonic estimator. Figure 5-5 depicts the solar PV-2 system connected to a pure sinusoidal infinite power source.

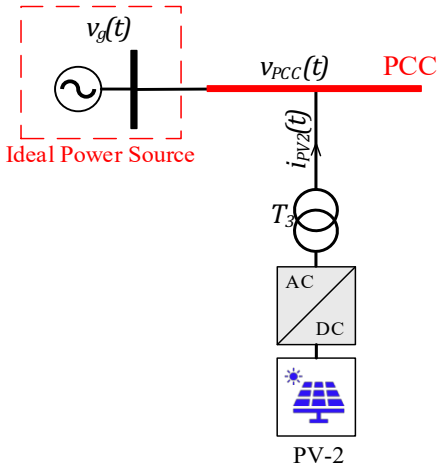

Figure 5-5 Solar PV system connected to a pure sinusoidal infinite power source.

The different cases considered for the simulated system are described in Table 5-2.

Table 5-2 Description of different cases considered for the simulated system.

Cases	**PCC Voltage**	**Information**
Case 1	Distorted	This case considers the power events with all the PE-based applications connected to the grid, and the system is simulated with the solar irradiance of Profile 1 used for the PV-2 system. The results are shown in Figure 5-6.
Case 2	Distorted	Like Case 1 but Profile 2 is used in this case for the solar PV-2 system. The results are presented in Figure 5-7.
Case 3	Sinusoidal	The solar PV-2 system is connected alone to the ideal power source, which is impractical in real power systems, and the solar irradiance of Profile 1 is simulated. The results are displayed in Figure 5-8.
Case 4	Sinusoidal	The solar PV-2 system is also connected alone to the ideal power source, but the solar irradiance of Profile 2 is employed in this case. The corresponding results are shown in Figure 5-9.

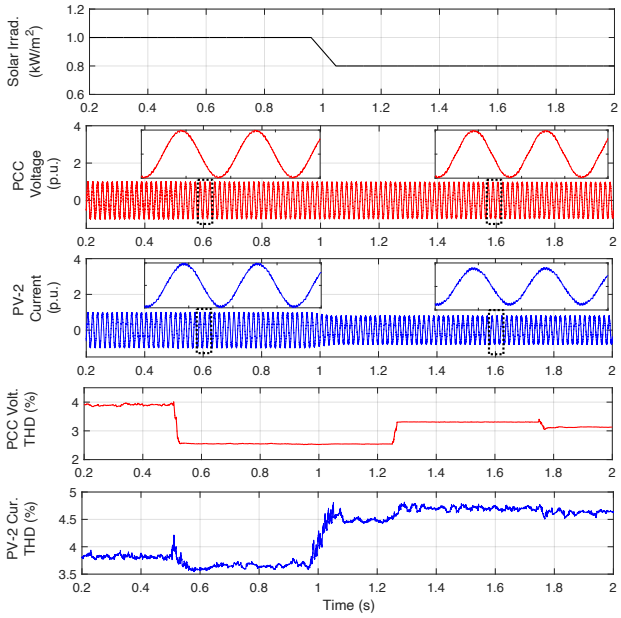

Figure 5-6 Performance of the simple power system simulated for Case 1, including distorted grid voltage due to other harmonic sources and power events under the solar irradiance of Profile 1

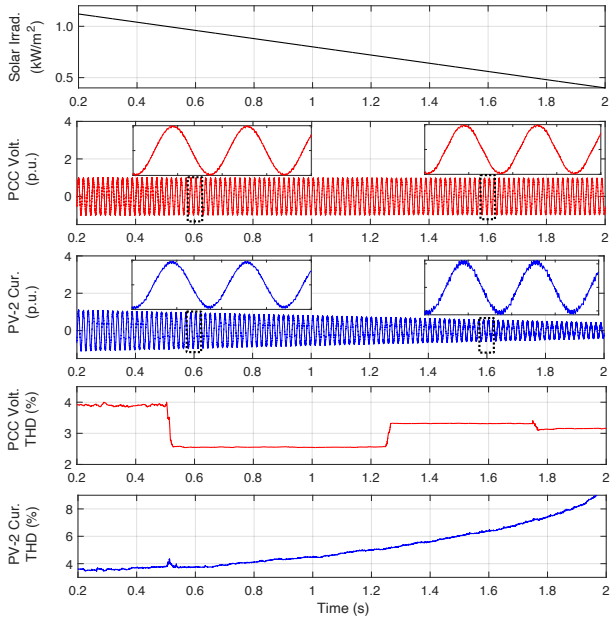

Figure 5-7 Performance of the simple power system simulated for Case 2, including distorted grid voltage due to other harmonic sources and power events under the solar irradiance of Profile 2.

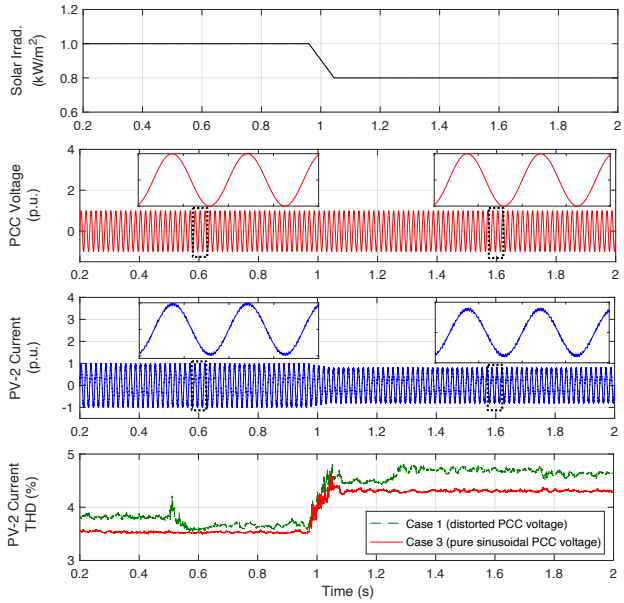

Figure 5-8 Performance of the simple power system simulated for Case 3, including a sinusoidal grid voltage under the solar irradiance of Profile 1.

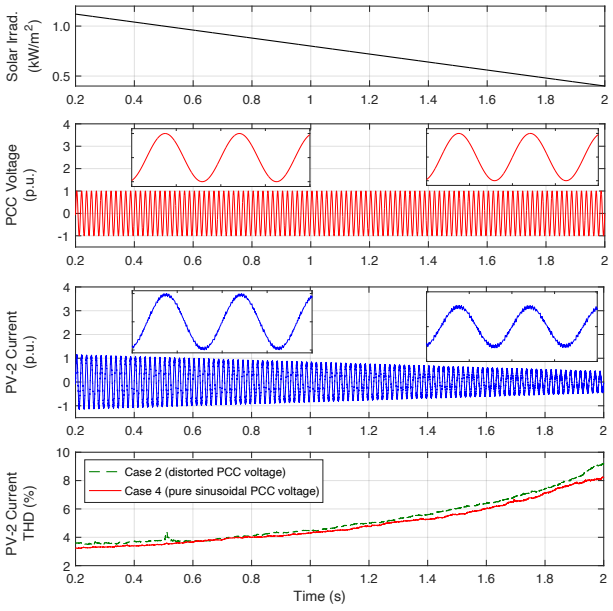

Figure 5-9 Performance of the simple power system simulated for Case 4, including a sinusoidal grid voltage under the solar irradiance of Profile 2.

The THDs of the PCC voltage and solar PV-2 system output current of the simple power system simulated over the simulation time are calculated using the FFT solution applied to the corresponding traces with respect to the fundamental frequency. Some observations from Figure 5-6 to Figure 5-9 are summarised as follows.

- Generally, the harmonic sources and power events have a pronounced influence on both the grid voltage and the PV-2 current THDs and can lead to inaccurate estimation of the PV-2 inverter harmonic emissions in comparison to Case 3 and Case 4 with a pure sinusoidal infinite power source.

- It can be observed that the general trend of the current THD of the solar PV-2 system is inversely proportional to the solar irradiance profile. For example, a decrease of 18% in the current THD due to an increase of 200 W/m^2 is experienced in Case 1. The reason behind this is that the higher solar irradiance means higher power being injected into the grid, and thus higher fundamental current and less THDs. This emphasises the dependency of the THD on the operating conditions.

- In Case 1, there is a noticeable association between the different events simulated and the voltage and current THDs. However, with the continuous variations in the solar irradiance of Profile 2, the impact of the power events can be minor on the solar PV output current THD.

- For Case 1 and Case 2, increasing the nonlinear load power at 0.5 seconds has significantly reduced the resultant voltage distortions at the PCC from 3.9% to 2.6%, and thus a 5.2% reduction in the current distortions of the solar PV-2 system is observed. This is due to the high fundamental current component being drawn from the grid, which is inversely proportional to the THD as shown in Equation (1.6).

- Also, at 1.25 seconds, the 30% increase in the grid impedance, which is heavily inductive and increases linearly with frequency developing higher voltage drops of each harmonic component, has increased the voltage THD at the PCC from 2.6% to 3.3% as shown in Figure 5-8.

- For grid-connected PE-based applications, the synchronization circuit and the control system have a considerable sensitivity to a distorted grid voltage. Therefore, the increase in the PCC voltage distortions has consequently increased the harmonic distortions of the solar PV-2 system by 5% in Case 1.

- The PFC capacitors are usually associated with the undesirable amplification effect on the harmonic components within the resonant point, which is caused by the interaction between the inductive elements of the grid and other system components and the PFC capacitance. These interactions can commonly trigger resonant frequencies, especially parallel resonances. At 1.75 seconds the resonance is absent when the PFC capacitors are disconnected, and thus the PCC voltage THD has dropped to 3.1% with a negligible impact on the solar PV-2 system current THD. This could be due to the fact that the parallel resonance takes place at frequencies where the harmonic components are less significant.

- It can be observed that the actual THD of the solar PV-2 system current when supplied with a pure sinusoidal voltage is considerably lower than that supplied with a distorted voltage at the PCC, depending on the variations in the solar irradiance. This is because that the control system has no interferences with other harmonic sources and the absence of changes in the system impedance.

The results of the system simulated are used next for training and evaluating the performance of the proposed ANN-based harmonic estimator. That is, since Case 2 includes a time-variant solar irradiance over the simulation time, its corresponding voltage and current along with the solar irradiance signals will be used to train the proposed harmonic distortions estimator. The results of Case 3 and Case 4 with the help of the simulation software will then be utilised as a reference to evaluate the performance of the ANN-based harmonic estimator over different solar irradiance points.

It is worth mentioning that since the ANN system performs well with signals rescaled within ± 1 p.u. due to the nature of the activation functions in the neurons [181], the voltage and current signals in the p.u. are applied directly to the ANN without the need for rescaling. However, the solar irradiance is rescaled based on the rated value of 1000 W/m^2.

5. 5. Estimator Training and Performance Evaluation

5. 5. 1. ANN Training Stage

The ANN system shown in Figure 5-3 is developed using MATLAB (R2021a) on a computer with a 64-bit Windows 10 operating system, an Intel Core TM i7 CPU 3.60 GHz, and 16 GB of RAM. The Levenberg-Marquardt backpropagation algorithm is adopted for training the system. The ANN system is trained with the simulated results of the voltage, current, and solar irradiance in Case 2 due to the continuous decay in the solar irradiance of Profile 2. To explore the performance of the proposed estimator, a defined range of the system output results is processed in the training stage. With a sampling time of 5 μs, about twenty cycles (from 0.5 to 0.8 seconds in Figure 5-7) are used based on the fundamental frequency. This results in about 66k samples each including the solar irradiances from 800 to 1000 W/m^2. The process of the proposed ANN-based harmonic distortion estimator is described in Figure 5-10.

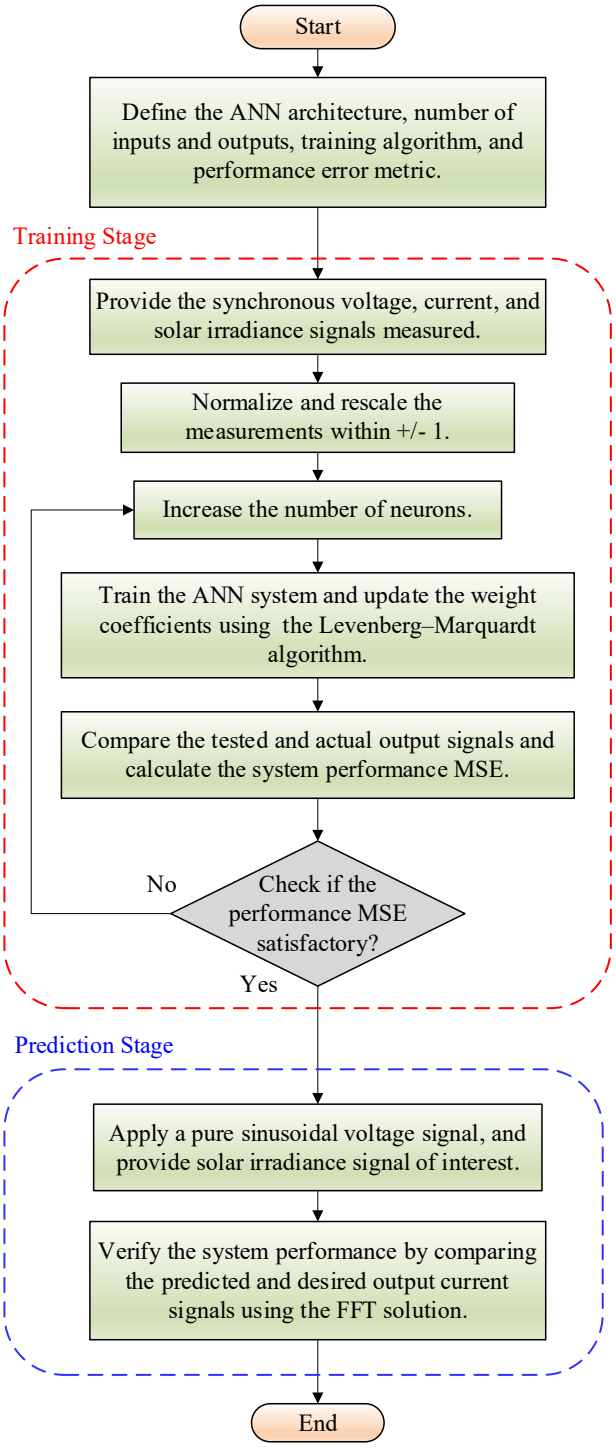

Figure 5-10 Flowchart of the proposed ANN-based harmonic distortion estimator for training and prediction stages.

For the proposed ANN-based harmonic distortions estimator, a multilayer perceptron, with two inputs, an output, and a single hidden layer, is sufficient as discussed in the literature presented before. However, the number of neurons in the hidden layer is chosen based on observations over the resultant MSE of five folds of the number of neurons as shown in Figure 5-11.

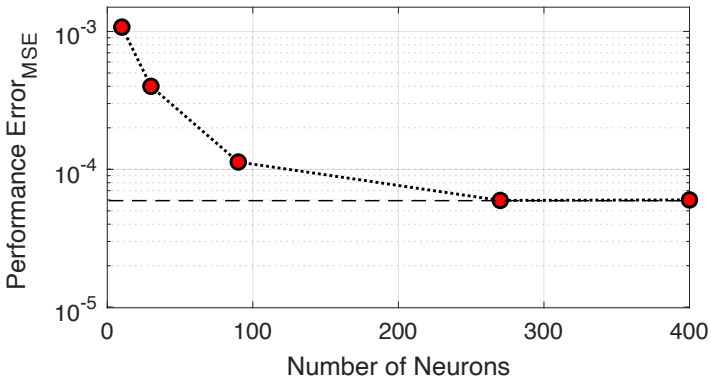

Figure 5-11 ANN performance error with a different number of neurons in the hidden layer.

Commonly, a small value of the MSE is satisfactory for ANN systems in many applications. Yet, the harmonic distortions estimator is required to have the lowest possible error to avoid misestimation of the actual distortion through the ANN system. The lowest MSE of 0.6×10^{-4} was achieved by using 270 neurons in the hidden layer, and it saturated afterwards for the given training algorithm and the data size. The main reasons for the high number of neurons are a large amount of data in the training set and the high accuracy required for such an application. Figure 5-12 illustrates the fitting of the resultant signal of the ANN (in blue) to the simulated current (in red) of the solar PV-2 system in Case 2 with different numbers of neurons.

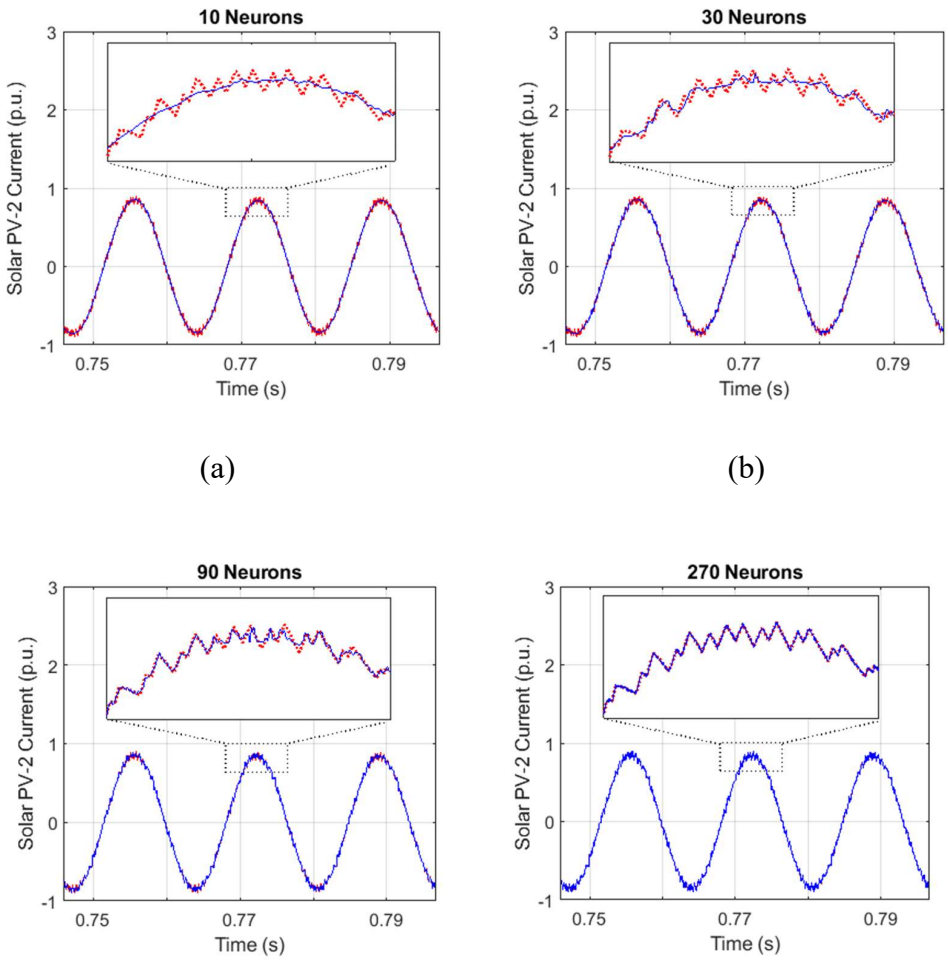

Figure 5-12 Effect of number of neurons on ANN system performance (three cycles are shown for illustration), simulated current (red), and ANN output (blue), (a) for 10 neurons, (b) for 30 neurons, (c) for 90 neurons, and (d) for 270 neurons.

The necessity for the lowest MSE in the training stage for the harmonic estimating system is evident. The solution of 30 neurons introduces a minor improvement to that of 10 neurons. However, with a higher number of neurons, the solution is much improved and predicted to result in an accurate fitting to the actual signal compared to a lower number of neuron solutions, which does not seem to capture the actual distortions of the solar PV-2 current. After training the ANN and ensuring its superior performance with the actual signal, now the system is almost expert and ready for the prediction stage.

5. 5. 2. ANN Prediction Stage

In this section, the expert ANN system performance is evaluated for different solar irradiance points within the training range. A mathematically generated pure sinusoidal voltage signal of 1 p.u. amplitude along with the solar irradiance signal in the form of vectors are applied to the expert ANN system developed in MATLAB. Then, the predicted results are compared with independently simulated system results for the same solar irradiance with a sinusoidal PCC voltage as shown in Figure 5-5. The prediction is performed on three equivalent cycles to reduce the computational burden. The input and output signals of the ANN system are processed as samples, while the simulated results at the steady-state are generated with respect to the simulation time.

The expert ANN performs well for solar irradiances within the training range. In Figure 5-13 and Figure 5-14, when a pure sinusoidal voltage signal is applied to the expert ANN system, for 800 W/m^2 and 1000 W/m^2 solar irradiance values, respectively, the predicted signals show a good agreement with that of the simulated system connected to a pure sinusoidal infinite power source as in Case 2 and Case 4, which reflect the true harmonic distortion of the system under the estimation. The FFT solution was performed in MATLAB for the two signals, and the results emphasise the accuracy of the ANN system in terms of the individual significant harmonic components with a maximum error of about 4%.

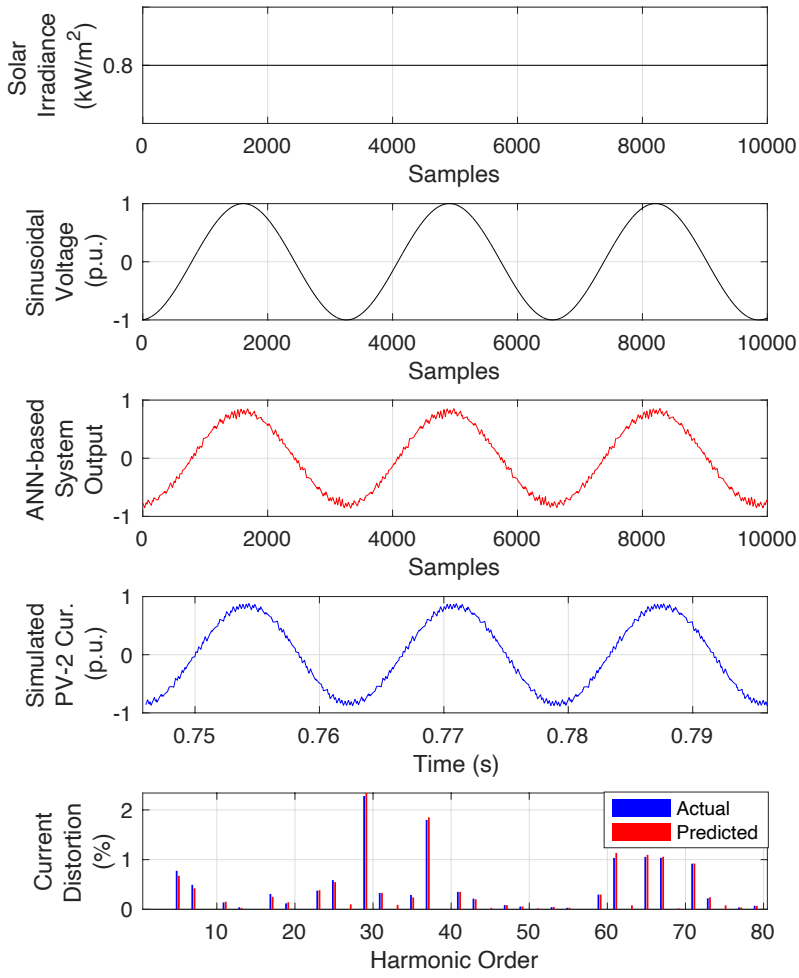

Figure 5-13 Proposed method performance at 800 W/m^2.

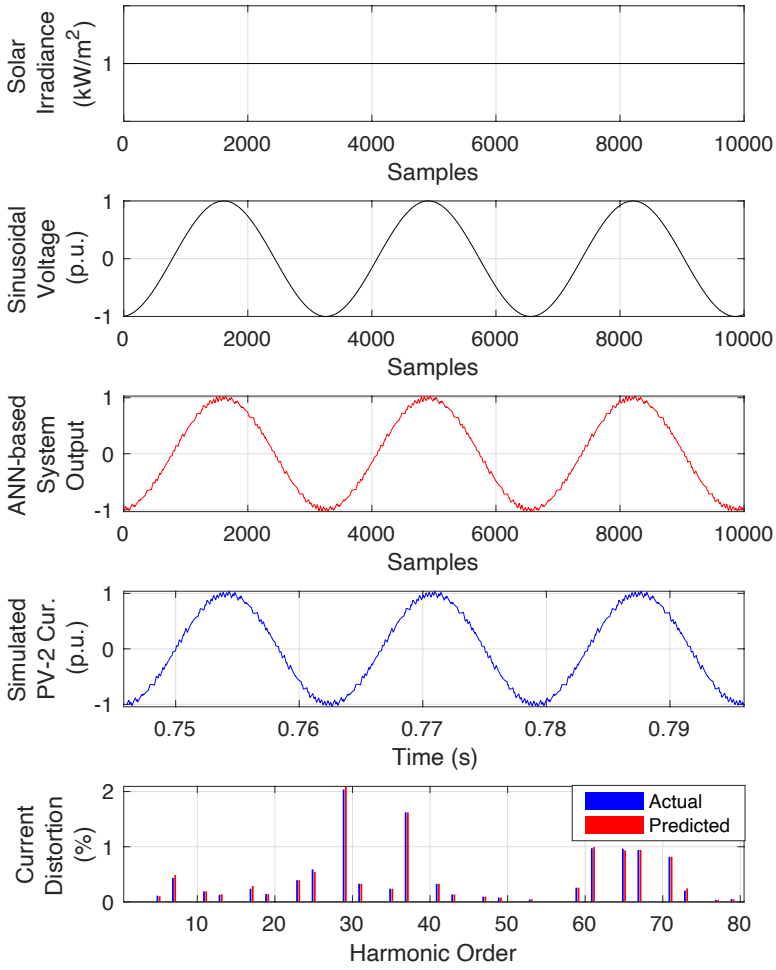

Figure 5-14 Proposed method performance at 1000 W/m^2.

Another important performance evaluating index of the ANN-based harmonic distortions estimator is the THD of the predicted signals. The results of the simple power system simulated was used as benchmark and reference to train and optimize the performance of the proposed estimator. The results predicted by the ANN harmonic distortion estimator are expected to closely match the results of the PV inverter harmonic performance when it is connected to a pure sinusoidal power source, which is the actual harmonic emissions. Table 5-3 shows the error of the THD of the actual and predicted signals, which is calculated as:

$$Error\ (\%) = \frac{|\ actual - predicted\ |}{actual} \times 100 \tag{5.4}$$

A relatively small error in the simulated and predicted THD can be observed. This is attributed to the uncharacteristic harmonic components in the predicted signals obtained from the proposed estimator and is related to the non-zero ANN performance error. The uncharacteristic harmonic components depend on the application and result mainly from dissymmetry imbalances in a power system [13].

An important factor that requires to be considered in the training and prediction stages is the computational effort of the ANN system with different numbers of neurons. For the given size of data, the more neurons in the hidden layer, the more computational time is required for convergence. For instance, the 270 neurons-based system requires roughly 250 and 40 seconds for the training and prediction process, respectively. This computational burden could be further reduced by computers with higher computational capability and larger memory size to process a large size data.

Table 5-3 THD comparison between simulated and predicted signals.

Solar Irradiance (W/m^2)	Simulated Current THD	ANN Predicted Current THD	Absolute Error
1000	3.60%	3.75%	4.17%
800	4.00%	4.18%	4.50%

5. 6. Validation of the Proposed ANN-based Estimator

To validate the proposed ANN-based harmonic distortions estimator, the IEEE 34-bus test feeder with the solar PV-2 system and different harmonic sources presented in [183] is modelled and simulated using Simulink/MATLAB. The feeder loading conditions were preserved following the specifications provided by the IEEE Power & Energy Society working group [184]. In this section, the IEEE 34-bus test feeder and the aspects on which the decision on the simulated system was based are

introduced. The harmonic sources simulated are also presented. Furthermore, the results obtained are analysed and discussed.

5. 6. 1. The IEEE 34-bus Test Feeder

Even though the IEEE 13-bus is the most used feeder for validating harmonic estimation and identification solutions, it only consists of six medium-voltage three-phase buses, which restricts the connection of different harmonic sources. The IEEE 34-bus test feeder depicted in Figure 5-15 was utilised in this fashion because of its length and light loading condition, making it appropriate for connecting the harmonic sources adopted in this work. There are 23 three-phase buses in the IEEE 34-bus. However, the solar PV-2 system and the different harmonic sources adopted will be connected to the green-highlighted nodes. Each harmonic source will be connected to a separate bus for each run, while the solar PV-2 system will remain connected to bus-860.

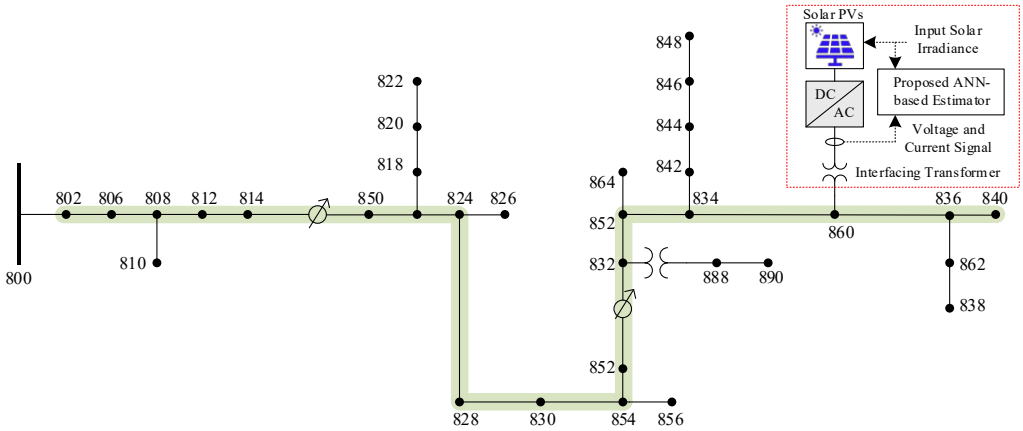

Figure 5-15 The IEEE 34-bus test feeder single-line diagram including the proposed ANN-based harmonic distortions estimator.

5. 6. 2. Harmonic Sources

Since the purpose of this research focuses on the harmonic distortions estimation of a PE-based application, the solar PV-2 system, different harmonic sources: Six-pulse and Twelve-pulse power rectifiers, Static Frequency Converter (SFC), Thyristor Controlled Reactors (TCR), and DC motor are simulated. These harmonic sources are modelled by harmonic current sources following the field

measurements provided in [183]. The phase angle of the current components of the harmonic sources is assumed to be aligned with the fundamental current components. Table 5-4 presents the characteristics of each harmonic source adopted in this work.

Table 5-4 Harmonic sources characteristics [183]

Harmonic Current	Magnitude (p.u.)				
	6-pulse	**12-pulse**	**SFC**	**DC motor**	**TCR**
3rd	0.015	0.002	-	0.138	0.012
5th	0.220	0.006	0.170	0.051	0.336
7th	0.150	0.003	0.101	0.026	0.016
9th	-	-	-	0.016	-
11th	0.102	0.062	0.061	0.011	0.087
13th	0.084	0.045	0.044	0.008	0.012
15th	-	-	-	0.006	-
17th	0.043	0.001	0.038	0.004	0.045
19th	0.034	0.002	0.032	0.004	0.013
21st	-	-	-	0.003	-
23rd	0.006	0.005	0.026	0.003	0.028
25th	-	-	0.023	0.002	-

5. 6. 3. Proposed Estimator Performance Analysis

The results were yielded by systematically allocating the different harmonic sources in the 18 feasible three-phase nodes within the green highlighted buses. Based on the two solar irradiance points (800 and 1000 W/m^2) and the five harmonic sources given in Table 5-4, a total of 180 tests were conducted. The simulated voltage and current signals of each run were stored and processed by the proposed ANN-based harmonic distortions estimator to predict the harmonic distortions of the solar PV-2 system. The predicted signals obtained from the proposed ANN-based estimator are compared to the harmonic current components shown in Table 5-5, and the error of each corresponding component for each test conducted is calculated as per Equation (5.4). For computational effort reduction, voltage and current signals of phase A were processed to the proposed estimator. The variations at the network level were neglected due to the absence of PFC capacitors and the loading conditions that were maintained unchanged over the simulation time. The harmonic current components of the established harmonic sources were simulated with the base values shown in Appendix 2. In addition, the sampling setting for the simulated

signals was set as discussed in Subsection 5.5.1 and the harmonic distortions were calculated using the FFT function developed in MATLAB.

Table 5-5 Solar PV-2 actual harmonic current components used as a reference for the validation.

Harmonic Order	**Magnitude (p.u.)**	
	800 W/m^2	1000 W/m^2
5th	0.0077	0.0011
7th	0.0049	0.0044
11th	0.0014	0.0019
13th	0.0004	0.0013
17th	0.0031	0.0024
19th	0.0012	0.0014
23rd	0.0038	0.0039
25th	0.0059	0.0059
29th	0.0228	0.0204
31st	0.0033	0.0033
35th	0.0029	0.0024
37th	0.0180	0.0162
41st	0.0035	0.0033
43rd	0.0021	0.0013
47th	0.0009	0.0010
49th	0.0006	0.0008

The error plots of each current harmonic component of the solar PV-2 system, obtained from the tests conducted are shown in Figure 5-16. The harmonic components within the range up to 50th were considered since they are significant in the solar PV-2 current spectra. The errors were computed considering the harmonic currents presented in Table 5-5 as a reference. The use of the Box plots can help visualise differences among different samples and provide more statistical information about the performance of such an estimator. These error results would also help demonstrate whether the proposed estimator can be applied for a quite larger power network including a variety of power harmonic sources. Figure 5-16(a) and Figure 5-16(b) are for the two solar irradiance points, 800 and 1000 W/m^2, respectively.

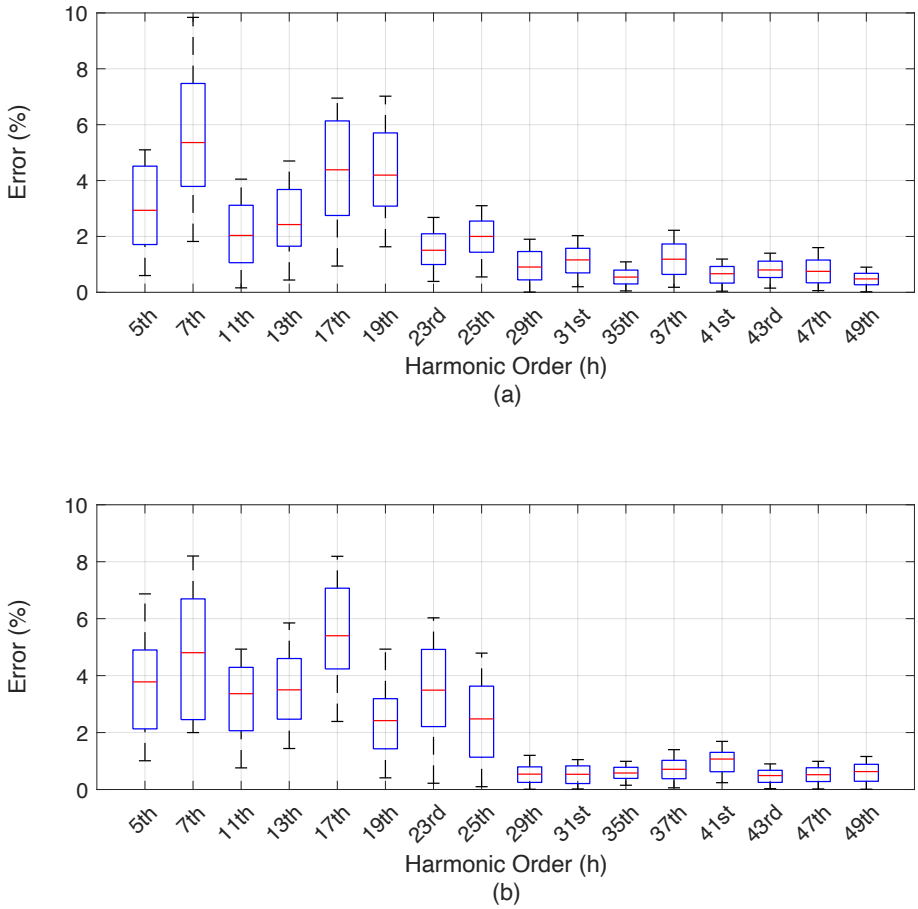

Figure 5-16 Errors obtained to estimate the harmonic distortion of the solar PV-2 system using the proposed ANN-based estimator in the IEEE 34-bus test feeder, (a) for 800 W/m^2 and (b) for 1000 W/m^2.

When analysing the error plots, it is observed that the greatest errors occur for the harmonic components from 5th to 25th. This is mainly because of the harmonic sources that have relatively higher harmonic currents within this range of frequencies. When an in-depth analysis is carried out, it is noticed that the greatest errors occur when the harmonic sources are placed electrically close to the bus to which the solar PV-2 system is connected, bus-860. However, for high order harmonics (i.e., higher than 25th), where the effects of the harmonic sources are absent, relatively smaller errors can be observed.

From Figure 5-16(a), the maximum error of the estimation of the low-order harmonic distortions is less than 10% with the highest median of a 5.36% for the lower solar irradiance, while the greatest error for the case of the higher solar irradiance is about 8.2% with a median of 5.4% as shown in Figure 5-16(b). For the high-order harmonic components, the proposed ANN-based estimator can perform with relatively higher accuracy. The maximum error in the two plots of 2.22% occurs at the 37th with a median of 1.2%. These resultant errors demonstrate the feasibility and accuracy of the proposed harmonic distortion estimator for a quite large power system with multiple harmonic sources and different operating conditions.

5. 7. Summary

In this chapter, a review of the previous work and an overview of the ANN-based system were presented. A method based on an ANN system utilising location-specific data was developed to capture the actual harmonic distortions of a harmonic source. The proposed method helps model the admittance of the harmonic source under the estimation, captures its harmonic performance over different operating conditions, and provides accurate harmonic distortions estimations. A simple power system was modelled and simulated, and the harmonic performance of a solar PV system for different cases was used to train the ANN system and improve its prediction with a relatively small performance error. The expert ANN-based harmonic distortion estimator was validated in the IEEE 34-bus test feeder with different established harmonic sources, and the results obtained from the proposed estimator were discussed. The proposed method has estimated the individual harmonic components with a maximum error of less than 10% and a maximum median of 5.4%.

Chapter 6. Conclusion and Future Work Recommendations

In this chapter, conclusions drawn from this research work and potential directions for future work are provided as follows:

6. 1. MVDC Converter Modelling for Harmonic Analysis Studies

Conclusion:

The introduction of the MVDC converters to the power distribution networks will help increase the networks' hosting capacity for more DER-based power sources and meet future growing energy consumption without triggering stability and thermal issues. An overview of the different configurations of the MVDC systems and a comparative analysis of the multilevel power converter topologies for such applications were presented. Furthermore, the detailed model of an MVDC converter with a suitable control system was developed to accurately capture the harmonic performance of such an application, which will further enable harmonic propagations analysis studies in the distribution network. An interleaved SPWM scheme was proposed to improve the MVDC converter harmonic performance, mitigate a wide range of the harmonic components, and validated using the Simulink/MATLAB simulation environment. The tuning of the PI controller's parameters was addressed using the Loop-shaping technique. The MVDC system performance at the fundamental and harmonic frequencies for different operating conditions was analysed, and the effectiveness of the control system and the harmonic reduction method were discussed. The key finding is that the interleaved SPWM technique has a significantly reduced THD of 2% at the rated system capacity with no significant even-order harmonic components.

Future Directions:

Apart from this work, an extensive analysis study is required for addressing the limitations associated with the MVDC converter topology in terms of circulating currents, DC voltage balancing, and fault isolation. Stability and sensitivity analysis of the proposed control system of MVDC converter with respect to the inevitable delay due to the digital control implementation and signal processing should also

be investigated with consideration of abnormalities at the power network level. Besides, harmonic instability studies have recently received considerable attention and, thus, the development of the harmonic state-space model of the MVDC converter is required. Comprehensive investigations of the impact of advanced control systems such as adaptive and model predictive control systems on the harmonic performance of such new MVDC technologies are required. The use of advanced controllers such as Proportional-Resonance for the low-order harmonic compensations should also be investigated for such an application. Additionally, since power distribution networks are subject to operation abnormalities like voltage unbalance and fault events, further investigations of the control performance for power harmonics improvements during these conditions are essential. Also, the effects of active control systems compensating the variations in the power loads and other power sources on harmonic performance should be addressed.

6. 2. MVDC Converter Harmonic Analysis in Distribution Networks

Conclusion:

The proposed MVDC system for the Albaha power network has shown its capability to improve the system's voltage profile and power losses. It would also improve the power network's hosting capacity for more renewable systems being under planning. However, the concern related to the MVDC harmonic performance in power systems was addressed. The Albaha power network was modelled for power harmonics analysis study. Different harmonic modelling techniques reported in the literature were compared. The frequency domain method was performed on the Albaha power network modelled based on real data and considering the MVDC converter as a harmonic source using the power system simulation package, IPSA. The MVDC harmonic propagations were analysed and evaluated against local harmonic standard limits. The results implied that the voltage THDs at different voltage levels comply with the locally defined standard limits. This work helps identify potential risky resonant points and the headroom of the THD limits for future installations with the presence of the MVDC system.

Future Directions:

Apart from this work, a probabilistic framework investigating the impact of the different harmonic modelling techniques proposed in the literature for the power system components with variations in power systems loading conditions and including switched PF correction capacitors in distribution networks is required. The use of probabilistic analysis methods can be considered to help investigate the impact of the power harmonics on power system components' loading capacity with different power harmonics profiles of multiple harmonic sources in the power system. Furthermore, comprehensive investigations of the EMC and interferences of the individual harmonic components should be considered to ensure the safe operation of the nearby sensitive electronic loads.

6. 3. Passive Power Filter Design and Harmonic Performance Analysis

Conclusion:

Power harmonics would unfavourably affect the operation of distribution network components and constrain the future connection of renewable systems. PPFs are anticipated to be widely used to reduce harmonic distortions, comply with the standard limits, improve system components' performance, and maximise the network's capacity. However, the design of such a PPF must meet the given power system requirements. Therefore, parameters of a 2nd-order, high-pass PPF were designed using the recently developed MRFO algorithm, and an analytical method based on the MCS was proposed to evaluate the harmonic performance of an optimally designed PPF, with variations in the power network.

For the superiority verification, the MRFO algorithm was compared with the most recently proposed optimization algorithms, namely GEO, RFO, and CSA, which have similar inspirations and behaviours. The optimization problem was formulated using the DHPF approach, and the newly developed MRFO algorithm was shown to result in the lowest network power losses, voltage distortions, and cost, with the best PoC voltage profile and PF correction. However, the MRFO has a better solution but requires relatively higher computational effort. It can be emphasised

that the main advantage of the MRFO algorithm is the variety of searching strategies that were incorporated to investigate more potential solutions within the search space. The computational complexity of the MRFO algorithm depends only on the number of iterations and variables, and the randomization-based and auto-tuned coefficients of the MRFO could offer a significant advantage over other algorithms that may rely on user-defined control parameters, affecting their overall performance. This work helped provide insight into the performance of the recently developed algorithms and investigate their performance for the PPF applications.

A thorough harmonic performance analysis study of the designed PPF was conducted using the developed MCS-based approach to include the variations in the linear loads, changes in background harmonics, and different harmonic source emissions. The stochastic method-based results of the harmonic performance analysis were discussed and the designed PPF showed superior performance in attenuating the high-order harmonics to alleviate the potential risk to the sensitive nearby loads and increase the system's hosting capacity for more renewable systems. The results imply that the optimally designed PPF can effectively attenuate the high-order harmonics for different operating conditions to reduce their impacts on power system components and increase the hosting capacity for more renewables. The proposed MCS method showed that the optimally designed PPF reduced the voltage THD and current TDD by roughly 54% and 30%, respectively, for the worst-case scenario, and improved the system performance parameters over different operating conditions to continually comply with the standard limits. An improvement in the network's hosting capacity of about 10% was also noticed.

Future Directions:

Apart from this work, insights into the performance of the new physics-based and human-based optimization algorithms for different PPF configurations, as a multi-objective optimization problem including the proposed MSC-based method, are being considered for future work. Modifications and improvements in the recently developed algorithm modelling, such as adaptive and optimised coefficients, are required to improve the performance of such new optimization methods. The impact of the switched PF correction capacitor banks on the harmonic performance

of different PPF topologies must also be addressed using the proposed MCS-based approach. Moreover, an appropriate investigating framework to accurately evaluate the improvements in the power network's hosting capacity for more renewable systems is required for today's power distribution systems.

6. 4. Harmonic Distortions Estimation using Artificial Neural Networks

Conclusion:

Renewable resources-based power sources are predicted to cause significant harmonic distortions in today's power networks due to the utilisation of power conversion systems, which are widely recognized as harmonic sources. When harmonic standard limits are violated, effective measures must be taken by the system operator and users to reduce their technical and financial effects. However, identifying the actual contribution of the offending harmonic source can be a challenging task with multiple harmonic sources connected, changes in the system's characteristic impedance, and the intermittent nature of renewable resources.

A method based on an ANN system utilising location-specific data was developed to capture the actual harmonic distortions of a harmonic source. The proposed method helped model the admittance of the harmonic source under the estimation, captured its harmonic performance over different operating conditions, and provided accurate harmonic distortions estimations. A simple power system was modelled and simulated, and the harmonic performance of a solar PV system for different cases was used to train the ANN system and improve its prediction with a relatively small performance error. The simple implementation and accurate prediction of the proposed system for the given size of data can compromise its relatively high computational burden. Additionally, the expert ANN-based harmonic distortion estimator was validated in the IEEE 34-bus test feeder with different harmonic sources' current components from a test field. The proposed system estimated the individual harmonic components with a maximum error of less than 10% and a maximum median of 5.4%.

Future Directions:

Apart from this work, insights into data synchronization complexity and implementation challenges for experimental validation with real data using a digital data acquisition system are under the consideration for future work. Renewable resources-based power sources such as solar PV systems are associated with inevitable uncertainties originating from partial/full shading and faulty cells/panels that must be addressed for reliable estimation. Besides, the fault tolerance of such an ANN-based estimator should be investigated to ensure reliable and robust estimating performance. It is also worth mentioning that advances in neural networks such as deep neural networks could also be a potential for such an application with large sizes of data to process.

References

[1] S. Bouckaert *et al.*, "Net Zero by 2050-A Roadmap for the Global Energy Sector," 2021. Accessed: Sep. 03, 2021. [Online]. Available: https://iea.blob.core.windows.net/assets/beceb956-0dcf-4d73-89fe-1310e3046d68/NetZeroby2050-ARoadmapfortheGlobalEnergySector_CORR.pdf

[2] C. Waite, "2019 UK Greenhouse Gas Emissions, Final Figures," 2021.

[3] "The UK Renewable Energy Strategy," 2009.

[4] "Energy trends," 2022. Accessed: Oct. 19, 2022. [Online]. Available: https://assets.publishing.service.gov.uk/government/uploads/system/uploads/attachment_data/file/1107502/Energy_Trends_September_2022.pdf

[5] "CLIMATE TRANSPARENCY REPORT 2020, Saudi Arabia," 2020.

[6] "REmap 2030: A Renewable Energy Roadmap, Summary of Findings," Abu Dhabi, 2014.

[7] "ELECTRICITY SYSTEM DEVELOPMENT: A FOCUS ON SMART GRIDS OVERVIEW OF ACTIVITIES AND PLAYERS IN SMART GRIDS," 2015.

[8] "A Strategy for Smart Meters and Smart Grids in the Kingdom of Saudi Arabia," 2012.

[9] S. M. Halpin and A. Card, "Power Quality," in *Power Electronics Handbook*, Elsevier, 2011. doi: 10.1016/B978-0-12-382036-5.00040-9.

[10] M. H. J. Bollen *et al.*, "Power Quality Concerns in Implementing Smart Distribution-Grid Applications," *IEEE Trans Smart Grid*, vol. 8, no. 1, Jan. 2017, doi: 10.1109/TSG.2016.2596788.

[11] M. Rezkallah, A. Chandra, A. Hamadi, H. Ibrahim, and M. Ghandour, "Power Quality in Smart Grids," in *Pathways to a Smarter Power System*, Elsevier, 2019. doi: 10.1016/B978-0-08-102592-5.00008-9.

[12] M. H. J. Bollen, *Understanding Power Quality Problems: Voltage Sags and Interruptions*. Wiley-IEEE Press, 1999.

[13] J. Arrillaga, B. C. Smith, N. R. Watson, and A. R. Wood, *Power System Harmonic Analysis*. West Sussex, England: John Wiley & Sons, Ltd,., 1997. doi: 10.1002/9781118878316.

[14] D. W. Hart, *Power Electronics*. Tata McGraw-Hill, 2010.

[15] Y. Wang, A. Aksoz, T. Geury, S. B. Ozturk, O. C. Kivanc, and O. Hegazy, "A Review of Modular Multilevel Converters for Stationary Applications," *Applied Sciences*, vol. 10, no. 21, p. 7719, Oct. 2020, doi: 10.3390/app10217719.

[16] A. F. Zobaa, *Power System Harmonics - Analysis, Effects and Mitigation Solutions for Power Quality Improvement*. InTech, 2018. doi: 10.5772/intechopen.68674.

[17] J. C. Das, *Power System Analysis: Short-Circuit Load Flow and Harmonics*, 2nd ed. CRC Press, 2017.

[18] H. W. Dommel, A. Yan, and S. Wei, "Harmonics from Transformer Saturation," *IEEE Transactions on Power Delivery*, vol. 1, no. 2, 1986, doi: 10.1109/TPWRD.1986.4307952.

[19] T. J. JR. APRILLE, “TWO COMPUTER ALGORITHMS FOR OBTAINING THE PERIODIC RESPONSE OF NONLINEAR CIRCUITS,” 1972.
[20] S. Hay and A. Ferguson, “A Review of Power System Modelling Platforms and Capabilities,” *IET*, 2015.
[21] M. Bajaj, N. K. Sharma, M. Pushkarna, H. Malik, M. A. Alotaibi, and A. Almutairi, “Optimal Design of Passive Power Filter Using Multi-Objective Pareto-Based Firefly Algorithm and Analysis Under Background and Load-Side’s Nonlinearity,” *IEEE Access*, vol. 9, 2021, doi: 10.1109/ACCESS.2021.3055774.
[22] R. Carbone, “A review of probabilistic methods for the analysis of low frequency power system harmonic distortion,” in *9th International Conference on Electromagnetic Compatibility*, 1994. doi: 10.1049/cp:19940690.
[23] S. Rios M. and R. Castaneda P., “Newton-Raphson probabilistic harmonic power flow through Monte Carlo simulation,” in *38th Midwest Symposium on Circuits and Systems. Proceedings*. doi: 10.1109/MWSCAS.1995.510335.
[24] J. B. Kwon, X. Wang, F. Blaabjerg, C. L. Bak, A. R. Wood, and N. R. Watson, “Harmonic Instability Analysis of a Single-Phase Grid-Connected Converter Using a Harmonic State-Space Modeling Method,” *IEEE Trans Ind Appl*, vol. 52, no. 5, pp. 4188–4200, Sep. 2016, doi: 10.1109/TIA.2016.2581154.
[25] M. Madrigal, *Modelling of Power Electronics Controllers for Harmonic Analysis*. Lap Lambert Academic Publishing GmbH KG, 2012.
[26] J. Arrillaga and C. D. Callaghan, “Double-iterative algorithm for the analysis of power and harmonic flows at AC/DC convertor terminals,” *IEE Proceedings C Generation, Transmission and Distribution*, vol. 136, no. 6, 1989, doi: 10.1049/ip-c.1989.0044.
[27] B. C. Smith, N. R. Watson, A. R. Wood, and J. Arrillaga, “A Newton solution for the harmonic phasor analysis of AC/DC converters,” *IEEE Transactions on Power Delivery*, vol. 11, no. 2, Apr. 1996, doi: 10.1109/61.489358.
[28] J. M. Bloemink and T. C. Green, “Benefits of Distribution-Level Power Electronics for Supporting Distributed Generation Growth,” *IEEE Transactions on Power Delivery*, vol. 28, no. 2, Apr. 2013, doi: 10.1109/TPWRD.2012.2232313.
[29] “ANGLE-DC: 2015 Electricity Network Innovation Competition,” 2015.
[30] T. A. H. Alghamdi, F. Anayi, and M. Packianather, “Optimal Design of Passive Power Filters Using the MRFO Algorithm and a Practical Harmonic Analysis Approach including Uncertainties in Distribution Networks,” *Energies (Basel)*, vol. 15, no. 7, p. 2566, Apr. 2022, doi: 10.3390/en15072566.
[31] C.-Y. Tang, Y.-F. Chen, Y.-M. Chen, and Y.-R. Chang, “DC-Link Voltage Control Strategy for Three-Phase Back-to-Back Active Power Conditioners,” *IEEE Transactions on Industrial Electronics*, vol. 62, no. 10, Oct. 2015, doi: 10.1109/TIE.2015.2420671.

[32] E. Romero-Ramos, A. Gómez-Expósito, A. Marano-Marcolini, J. M. Maza-Ortega, and J. L. Martinez-Ramos, "Assessing the loadability of active distribution networks in the presence of DC controllable links," *IET Generation, Transmission & Distribution*, vol. 5, no. 11, 2011, doi: 10.1049/iet-gtd.2011.0080.

[33] M. Barragán-Villarejo, E. Romero-Ramos, A. Marano-Marcolini, J. M. Maza-Ortega, and A. Gómez-Expósito, "Voltage source converter-based topologies to further integrate renewable energy sources in distribution systems," *IET Renewable Power Generation*, vol. 6, no. 6, Nov. 2012, doi: 10.1049/iet-rpg.2011.0246.

[34] J. M. Bloemink and T. C. Green, "Increasing distributed generation penetration using soft normally-open points," in *IEEE PES General Meeting*, Jul. 2010. doi: 10.1109/PES.2010.5589629.

[35] W. Cao, J. Wu, N. Jenkins, C. Wang, and T. Green, "Operating principle of Soft Open Points for electrical distribution network operation," *Appl Energy*, vol. 164, Feb. 2016, doi: 10.1016/j.apenergy.2015.12.005.

[36] N. Okada, M. Takasaki, H. Sakai, and S. Katoh, "Development of a 6.6 kV - 1 MVA Transformerless Loop Balance Controller," in *2007 IEEE Power Electronics Specialists Conference*, 2007. doi: 10.1109/PESC.2007.4342144.

[37] Jieying. Song, Y. Zhang, Z. Gao, C. Cao, Z. Wang, and F. Xu, "Research on Topology and Control Technology of Soft Multi-State Open Point with Fault Isolation Capability," in *2018 China International Conference on Electricity Distribution (CICED)*, Sep. 2018. doi: 10.1109/CICED.2018.8592197.

[38] A. Aithal and J. Wu, "Operation and performance of a medium-voltage DC link," *CIRED - Open Access Proceedings Journal*, vol. 2017, no. 1, Oct. 2017, doi: 10.1049/oap-cired.2017.0946.

[39] J. Chen, W. Ming, C. E. Ugalde-Loo, S. Wang, and N. Jenkins, "Analysis and Mitigation of DC Voltage Imbalance for Medium-Voltage Cascaded Three-Level Neutral-Point-Clamped Converters," *IEEE Trans Power Electron*, vol. 37, no. 4, pp. 4320–4336, Apr. 2022, doi: 10.1109/TPEL.2021.3129877.

[40] R. A. A. Graaff, J. M. Myrzik, W. L. Kling, and J. H. R. Enslin, "Series Controllers in Distribution Systems - Facilitating Increased Loading and Higher DG Penetration," in *2006 IEEE PES Power Systems Conference and Exposition*, Oct. 2006. doi: 10.1109/PSCE.2006.296208.

[41] L. J. Thomas, A. Burchill, D. J. Rogers, M. Guest, and N. Jenkins, "Assessing distribution network hosting capacity with the addition of soft open points," in *5th IET International Conference on Renewable Power Generation (RPG) 2016*, 2016. doi: 10.1049/cp.2016.0553.

[42] R. A. A. Graaff, J. M. A. Myrzik, W. L. Kling, and J. H. R. Enslin, "Intelligent Nodes in Distribution Systems - Optimizing Steady State Settings," in *2007 IEEE Lausanne Power Tech*, Jul. 2007. doi: 10.1109/PCT.2007.4538349.

[43] P. Li, G. Song, H. Ji, J. Zhao, C. Wang, and J. Wu, "A supply restoration method of distribution system based on Soft Open Point," in *2016 IEEE*

Innovative Smart Grid Technologies - Asia (ISGT-Asia), Nov. 2016. doi: 10.1109/ISGT-Asia.2016.7796441.

[44] T. Joseph *et al.*, "Dynamic Average Converter Model for MVDC Link Harmonic Analysis," in *2019 IEEE Milan PowerTech*, Jun. 2019. doi: 10.1109/PTC.2019.8810551.

[45] T. Joseph *et al.*, "Analysis of harmonic transfer through an MVDC Link," in *15th IET International Conference on AC and DC Power Transmission (ACDC 2019)*, 2019. doi: 10.1049/cp.2019.0017.

[46] B. R. Andersen and S. L. Nilsson, *Flexible AC Transmission Systems*. Springer International Publishing, 2020.

[47] M. A. Abdelrahman, C. Long, J. Wu, and N. Jenkins, "Optimal Operation of Multi-Terminal Soft Open Point to Increase Hosting Capacity of Distributed Generation in Medium Voltage Networks," in *2018 53rd International Universities Power Engineering Conference (UPEC)*, Sep. 2018, pp. 1–6. doi: 10.1109/UPEC.2018.8541861.

[48] M. M. Haque, M. S. Ali, P. Wolfs, and F. Blaabjerg, "A UPFC for Voltage Regulation in LV Distribution Feeders With a DC-Link Ripple Voltage Suppression Technique," *IEEE Trans Ind Appl*, vol. 56, no. 6, pp. 6857–6870, Nov. 2020, doi: 10.1109/TIA.2020.3023068.

[49] E. Kabalci, *Multilevel Inverters: Introduction and Emergent Topologies*. Elsevier Science, 2021.

[50] S. A. Gonzalez, S. A. Verne, and M. I. Valla, *Multilevel Converters for Industrial Applications*. CRC Press, 2017.

[51] G. P. Adam and B. W. Williams, "New emerging voltage source converter for high-voltage application: hybrid multilevel converter with dc side H-bridge chain links," *IET Generation, Transmission & Distribution*, vol. 8, no. 4, pp. 765–773, Apr. 2014, doi: 10.1049/iet-gtd.2013.0076.

[52] M. Marchesoni, M. Mazzucchelli, and S. Tenconi, "A non conventional power converter for plasma stabilization," in *19th Annual IEEE Power Electronics Specialists Conference*, 1988. doi: 10.1109/PESC.1988.18125.

[53] A. Nabae, I. Takahashi, and H. Akagi, "A New Neutral-Point-Clamped PWM Inverter," *IEEE Trans Ind Appl*, vol. IA-17, no. 5, Sep. 1981, doi: 10.1109/TIA.1981.4503992.

[54] T. A. Meynard and H. Foch, "Multi-Level Choppers for High Voltage Applications," *EPE Journal*, vol. 2, no. 1, Jan. 1992, doi: 10.1080/09398368.1992.11463285.

[55] A. Poorfakhraei, M. Narimani, and A. Emadi, "A Review of Multilevel Inverter Topologies in Electric Vehicles: Current Status and Future Trends," *IEEE Open Journal of Power Electronics*, vol. 2, pp. 155–170, 2021, doi: 10.1109/OJPEL.2021.3063550.

[56] F. Renken, "Analytic calculation of the dc-link capacitor current for pulsed three phase inverters," 2004.

[57] L. Asiminoaei, E. Aeloiza, P. N. Enjeti, and F. Blaabjerg, "Shunt Active-Power-Filter Topology Based on Parallel Interleaved Inverters," *IEEE Transactions on Industrial Electronics*, vol. 55, no. 3, Mar. 2008, doi: 10.1109/TIE.2007.907671.

[58] J. Yu, K. Smith, M. Urizarbarrena, M. Bebbington, N. Macleod, and A. Moon, "Initial designs for ANGLE-DC project: challenges converting

existing AC cable and overhead line to DC operation," *CIRED - Open Access Proceedings Journal*, vol. 2017, no. 1, Oct. 2017, doi: 10.1049/oap-cired.2017.0974.
[59] G. P. Adam, *Voltage Source Converter: Modulation, Control and Applications in Power Systems*. Createspace Independent Pub, 2013.
[60] A. Yazdani and R. Iravani, *Voltage-Sourced Converters in Power Systems: Modeling, Control, and Applications*. Wiley, 2010.
[61] D. Zhou, Y. Song, and F. Blaabjerg, "Modeling and Control of Three-Phase AC/DC Converter Including Phase-Locked Loop," in *Control of Power Electronic Converters and Systems*, Elsevier, 2018. doi: 10.1016/B978-0-12-805245-7.00005-6.
[62] T. Suntio, T. Messo, and J. Puukko, *Power Electronic Converters: Dynamics and Control in Conventional and Renewable Energy Applications*. Wiley, 2017.
[63] G. Adam, O. Anaya-Lara, G. Burt, S. Finney, B. Williams, and J. Mcdonald, "Comparison between two VSC-HVDC transmission systems technologies: modular and neutral point clamped multilevel converter," 2009.
[64] G. K. Dubey, *Fundamentals of Electrical Drives*. CRC Press, 2002.
[65] S. M. Abu Sharkh and M. A. Abu-Sara, "Current Control of Utility-Connected Two-Level and Three-Level Pwm Inverters," *EPE Journal*, vol. 14, no. 4, Nov. 2004, doi: 10.1080/09398368.2004.11463568.
[66] M. Gerber, J. A. Ferreira, I. W. Hofsajer, and N. Seliger, "High Density Packaging of the Passive Components in an Automotive DC/DC Converter," *IEEE Trans Power Electron*, vol. 20, no. 2, Mar. 2005, doi: 10.1109/TPEL.2004.843020.
[67] B. Destraz, Y. Louvrier, and A. Rufer, "High Efficient Interleaved Multi-channel dc/dc Converter Dedicated to Mobile Applications," in *Conference Record of the 2006 IEEE Industry Applications Conference Forty-First IAS Annual Meeting*, Oct. 2006. doi: 10.1109/IAS.2006.256893.
[68] M. Pavlovsky, Yukinori Tsuruta, and Atsuo Kawamura, "Pursuing high power-density and high efficiency in DC-DC converters for automotive application," in *2008 IEEE Power Electronics Specialists Conference*, Jun. 2008. doi: 10.1109/PESC.2008.4592604.
[69] Wuhua Li and Xiangning He, "A Family of Isolated Interleaved Boost and Buck Converters With Winding-Cross-Coupled Inductors," *IEEE Trans Power Electron*, vol. 23, no. 6, Nov. 2008, doi: 10.1109/TPEL.2008.2004767.
[70] Bo Yang, Wuhua Li, Yi Zhao, and Xiangning He, "Design and Analysis of a Grid-Connected Photovoltaic Power System," *IEEE Trans Power Electron*, vol. 25, no. 4, Apr. 2010, doi: 10.1109/TPEL.2009.2036432.
[71] D.-Y. Jung, Y.-H. Ji, S.-H. Park, Y.-C. Jung, and C.-Y. Won, "Interleaved Soft-Switching Boost Converter for Photovoltaic Power-Generation System," *IEEE Trans Power Electron*, vol. 26, no. 4, Apr. 2011, doi: 10.1109/TPEL.2010.2090948.
[72] L. Asiminoaei, E. Aeloiza, P. N. Enjeti, and F. Blaabjerg, "Shunt Active-Power-Filter Topology Based on Parallel Interleaved Inverters," *IEEE*

Transactions on Industrial Electronics, vol. 55, no. 3, Mar. 2008, doi: 10.1109/TIE.2007.907671.

[73] di Zhang, F. Wang, R. Burgos, Rixin Lai, and D. Boroyevich, "Impact of Interleaving on AC Passive Components of Paralleled Three-Phase Voltage-Source Converters," *IEEE Trans Ind Appl*, vol. 46, no. 3, 2010, doi: 10.1109/TIA.2010.2045336.

[74] H.-S. Jung, "Interleaved Pulse Width Modulation Based on Modified Carrier in Parallel Operation," *IEEE Access*, vol. 9, pp. 109775–109784, 2021, doi: 10.1109/ACCESS.2021.3100579.

[75] B. N. Singh, G. Joos, and P. Jain, "A new topology of 3-phase PWM AC/DC interleaved converter for telecommunication supply systems," in *35th IAS Annual Meeting and World Conference on Industrial Applications of Electrical Energy*, 2000. doi: 10.1109/IAS.2000.883144.

[76] B. Tamyurek and D. A. Torrey, "A Three-Phase Unity Power Factor Single-Stage AC–DC Converter Based on an Interleaved Flyback Topology," *IEEE Trans Power Electron*, vol. 26, no. 1, Jan. 2011, doi: 10.1109/TPEL.2010.2060359.

[77] O. Garcia, P. Zumel, A. de Castro, and A. Cobos, "Automotive DC-DC bidirectional converter made with many interleaved buck stages," *IEEE Trans Power Electron*, vol. 21, no. 3, May 2006, doi: 10.1109/TPEL.2006.872379.

[78] M. Gerber, J. A. Ferreira, I. W. Hofsajer, and N. Seliger, "Interleaving optimization in synchronous rectified DC/DC converters," in *IEEE 35th Annual Power Electronics Specialists Conference*, 2004. doi: 10.1109/PESC.2004.1354823.

[79] J. A. Oliver, P. Zumel, O. Garcia, J. A. Cobos, and J. Uceda, "Passive component analysis in interleaved buck converters," in *19th Annual IEEE Applied Power Electronics Conference and Exposition*, 2004. doi: 10.1109/APEC.2004.1295871.

[80] T. Nussbaumer, K. Raggl, and J. W. Kolar, "Design Guidelines for Interleaved Single-Phase Boost PFC Circuits," *IEEE Transactions on Industrial Electronics*, vol. 56, no. 7, Jul. 2009, doi: 10.1109/TIE.2009.2020073.

[81] CIGRE WG 36-05, "Harmonics, characteristic parameters, methods of study, estimates of existing values in the network," 1981.

[82] "Modeling and simulation of the propagation of harmonics in electric power networks. I. Concepts, models, and simulation techniques," *IEEE Transactions on Power Delivery*, vol. 11, no. 1, 1996, doi: 10.1109/61.484130.

[83] W. H. Kersting, *Distribution System Modeling and Analysis*, 4th ed. CRC Press, 2018.

[84] CIGRE TB 531, "Cable systems electrical characteristics," 2013.

[85] L. H. Kocewiak and B. Gustavsen, "Impact of Cable Impedance Modelling Assumptions on Harmonic Losses in Offshore Wind Power Plants," 2018.

[86] C. Liu, L. Qi, X. Cui, and X. Wei, "Experimental Extraction of Parasitic Capacitances for High-Frequency Transformers," *IEEE Trans Power Electron*, vol. 32, no. 6, Jun. 2017, doi: 10.1109/TPEL.2016.2597498.

[87] CIGRE WG CC-02, “Guide for assessing the network harmonic impedance,” 1996.
[88] “IEEE Recommended Practice for Industrial and Commercial Power Systems Analysis,” 1998.
[89] CIGRE JTF, “AC System Modelling For AC Filter Design – An Overview of Impedance Modelling,” 1996.
[90] G. FUNK and T. HANTEL, “The frequency-dependent characteristics of three-phase power system equipment,” *VDE-Verlag*, vol. 9, no. 11, 1987.
[91] Jing Zhu, E. Bećirović, and J. V. Milanović, “The Effect of Network Modelling on Harmonic Propagation Studies in Power Electronics Rich Transmission Networks,” in *11th IET International Conference on Advances in Power System Control, Operation and Management (APSCOM 2018)*, 2018. doi: 10.1049/cp.2018.1772.
[92] “Saudi Vision 2030,” Sep. 01, 2021.
[93] “Indicators of Renewable Energy in Saudi Arabia 2018,” 2018.
[94] R. R. Obaid, “Seasonal-Water Dams: A Great Potential for Hydropower Generation in Saudi Arabia,” *International Journal of Sustainable Water and Environmental Systems*, vol. 07, no. 1, 2015, doi: 10.5383/swes.7.01.001.
[95] Saudi Press Agency, “GACA Contributes to Growth of Domestic Tourism in Southern Regions,” Aug. 22, 2020. https://www.spa.gov.sa/viewfullstory.php?lang=en&newsid=2124522 (accessed Aug. 22, 2020).
[96] Albaha University, “Faculty of Medicine,” 2020. https://bu.edu.sa/en/web/faculty-of-medicine (accessed Sep. 04, 2021).
[97] ECRA-SEC, “Laws and Regilations:Codes and Standards.” https://www.ecra.gov.sa/en-us/ECRARegulations/Codes/Pages/Codes.aspx (accessed Sep. 04, 2021).
[98] B. Hammer, C. Fuhr, J. Hanson, and U. Konigorski, “Differences of Power Flows in Transmission and Distribution Networks and Implications on Inverter Droop Control,” in *2019 International Conference on Clean Electrical Power (ICCEP)*, Jul. 2019. doi: 10.1109/ICCEP.2019.8890222.
[99] “IEEE Recommended Practice and Requirements for Harmonic Control in Electric Power Systems,” *IEEE Std 519-2014 (Revision of IEEE Std 519-1992)*, pp. 1–29, Jun. 2014.
[100] J. C. Das, “Harmonic Resonance,” in *Power System Harmonics and Passive Filter Designs*, Hoboken, NJ, USA: John Wiley & Sons, Inc, 2015. doi: 10.1002/9781118887059.ch9.
[101] T. Busatto, A. Larsson, S. K. Ronnberg, and M. H. J. Bollen, “Including Uncertainties From Customer Connections in Calculating Low-Voltage Harmonic Impedance,” *IEEE Transactions on Power Delivery*, vol. 34, no. 2, Apr. 2019, doi: 10.1109/TPWRD.2018.2881222.
[102] X. Wang, F. Blaabjerg, and W. Wu, “Modeling and Analysis of Harmonic Stability in an AC Power-Electronics-Based Power System,” *IEEE Trans Power Electron*, vol. 29, no. 12, Dec. 2014, doi: 10.1109/TPEL.2014.2306432.
[103] S. M. Ismael, S. H. E. Abdel Aleem, A. Y. Abdelaziz, and A. F. Zobaa, “State-of-the-art of hosting capacity in modern power systems with

distributed generation," *Renew Energy*, vol. 130, Jan. 2019, doi: 10.1016/j.renene.2018.07.008.
[104] M. Bajaj and A. K. Singh, "Optimal design of passive power filter for enhancing the harmonic-constrained hosting capacity of renewable DG systems," *Computers & Electrical Engineering*, vol. 97, Jan. 2022, doi: 10.1016/j.compeleceng.2021.107646.
[105] Y. Wang, P. Chen, J. Yong, W. Xu, S. Xu, and K. Liu, "A Comprehensive Investigation on the Selection of High-Pass Harmonic Filters," *IEEE Transactions on Power Delivery*, 2022, doi: 10.1109/TPWRD.2022.3147835.
[106] J. C. Das, "Design and application of a second order high pass damped filter for 8000-hp ID fan drives-a case study," in *Conference Record of 2014 Annual Pulp and Paper Industry Technical Conference*, Jun. 2014. doi: 10.1109/PPIC.2014.6871159.
[107] D. Melvold, "Pacific HVDC Intertie System AC Side Harmonic Studies," *IEEE Transactions on Power Apparatus and Systems*, vol. PAS-92, no. 2, pp. 690–701, Mar. 1973, doi: 10.1109/TPAS.1973.293774.
[108] H. Hu, Z. He, and S. Gao, "Passive Filter Design for China High-Speed Railway With Considering Harmonic Resonance and Characteristic Harmonics," *IEEE Transactions on Power Delivery*, vol. 30, no. 1, pp. 505–514, Feb. 2015, doi: 10.1109/TPWRD.2014.2359010.
[109] A. M. Sharaf and M. E. Fisher, "An optimization based technique for power system harmonic filter design," *Electric Power Systems Research*, vol. 30, no. 1, Jun. 1994, doi: 10.1016/0378-7796(94)90060-4.
[110] V. Verma and B. Singh, "Genetic-Algorithm-Based Design of Passive Filters for Offshore Applications," *IEEE Trans Ind Appl*, vol. 46, no. 4, Jul. 2010, doi: 10.1109/TIA.2010.2049629.
[111] G. W. Chang, S. Y. Chu, and H. L. Wang, "A New Method of Passive Harmonic Filter Planning for Controlling Voltage Distortion in a Power System," *IEEE Transactions on Power Delivery*, vol. 21, no. 1, pp. 305–312, Jan. 2006, doi: 10.1109/TPWRD.2005.852355.
[112] Z. Juan, G. Yi-nan, and Z. Shu-ying, "Optimal design of passive power filters of an asymmetrical system based on genetic algorithm," *Procedia Earth and Planetary Science*, vol. 1, no. 1, Sep. 2009, doi: 10.1016/j.proeps.2009.09.222.
[113] I. D. Melo, J. L. R. Pereira, A. M. Variz, and P. F. Ribeiro, "Allocation and sizing of single tuned passive filters in three-phase distribution systems for power quality improvement," *Electric Power Systems Research*, vol. 180, Mar. 2020, doi: 10.1016/j.epsr.2019.106128.
[114] J. C. Leite, I. P. Abril, M. E. de L. Tostes, and R. C. L. de Oliveira, "Multi-objective optimization of passive filters in industrial power systems," *Electrical Engineering*, vol. 99, no. 1, Mar. 2017, doi: 10.1007/s00202-016-0420-3.
[115] Y. Wang, K. Yin, H. Liu, and Y. Yuan, "A Method for Designing and Optimizing the Electrical Parameters of Dynamic Tuning Passive Filter," *Symmetry (Basel)*, vol. 13, no. 7, Jun. 2021, doi: 10.3390/sym13071115.
[116] M. Milovanović, J. Radosavljević, D. Klimenta, and B. Perović, "GA-based approach for optimal placement and sizing of passive power filters to

reduce harmonics in distorted radial distribution systems," *Electrical Engineering*, vol. 101, no. 3, Sep. 2019, doi: 10.1007/s00202-019-00805-w.

[117] I. F. Mohamed, S. H. E. Abdel Aleem, A. M. Ibrahim, and A. F. Zobaa, "Optimal Sizing of C-Type Passive Filters under Non-Sinusoidal Conditions," *Energy Technology & Policy*, vol. 1, no. 1, Jan. 2014, doi: 10.1080/23317000.2014.969453.

[118] S. H. E. Abdel Aleem, A. F. Zobaa, and M. M. Abdel Aziz, "Optimal C-Type Passive Filter Based on Minimization of the Voltage Harmonic Distortion for Nonlinear Loads," *IEEE Transactions on Industrial Electronics*, vol. 59, no. 1, Jan. 2012, doi: 10.1109/TIE.2011.2141099.

[119] S. H. E. Abdel Aleem, A. F. Zobaa, M. E. Balci, and S. M. Ismael, "Harmonic Overloading Minimization of Frequency-Dependent Components in Harmonics Polluted Distribution Systems Using Harris Hawks Optimization Algorithm," *IEEE Access*, vol. 7, 2019, doi: 10.1109/ACCESS.2019.2930831.

[120] S. H. E. Abdel Aleem, A. F. Zobaa, and M. E. Balci, "Optimal resonance-free third-order high-pass filters based on minimization of the total cost of the filters using Crow Search Algorithm," *Electric Power Systems Research*, vol. 151, Oct. 2017, doi: 10.1016/j.epsr.2017.06.009.

[121] N. M. Khattab *et al.*, "A novel design of fourth-order harmonic passive filters for total demand distortion minimization using crow spiral-based search algorithm," *Ain Shams Engineering Journal*, vol. 13, no. 3, May 2022, doi: 10.1016/j.asej.2021.11.001.

[122] H. H. Zeineldin and A. F. Zobaa, "Particle Swarm Optimization of Passive Filters for Industrial Plants in Distribution Networks," *Electric Power Components and Systems*, vol. 39, no. 16, Oct. 2011, doi: 10.1080/15325008.2011.615795.

[123] A. M. Sharaf and A. A. A. El-Gammal, "A novel discrete multi-objective Particle Swarm Optimization (MOPSO) of optimal shunt power filter," in *2009 IEEE/PES Power Systems Conference and Exposition*, Mar. 2009. doi: 10.1109/PSCE.2009.4839957.

[124] Y.-P. Chang and C.-N. Ko, "A PSO method with nonlinear time-varying evolution based on neural network for design of optimal harmonic filters," *Expert Syst Appl*, vol. 36, no. 3, Apr. 2009, doi: 10.1016/j.eswa.2008.08.007.

[125] Y.-P. Chang, C. Low, and C.-J. Wu, "Optimal Design of Discrete-Value Passive Harmonic Filters Using Sequential Neural-Network Approximation and Orthogonal Array," *IEEE Transactions on Power Delivery*, vol. 22, no. 3, Jul. 2007, doi: 10.1109/TPWRD.2007.899780.

[126] He Na, Huang Lina, Wu Jian, and Xu Dianguo, "Study on optimal design method for passive power filters set at high voltage bus considering many practical aspects," in *2008 Twenty-Third Annual IEEE Applied Power Electronics Conference and Exposition*, Feb. 2008. doi: 10.1109/APEC.2008.4522752.

[127] Na He, Dianguo Xu, and L. Huang, "The Application of Particle Swarm Optimization to Passive and Hybrid Active Power Filter Design," *IEEE*

Transactions on Industrial Electronics, vol. 56, no. 8, Aug. 2009, doi: 10.1109/TIE.2009.2020739.

[128] N. Yang and M. Le, "Multi-objective bat algorithm with time-varying inertia weights for optimal design of passive power filters set," *IET Generation, Transmission & Distribution*, vol. 9, no. 7, Apr. 2015, doi: 10.1049/iet-gtd.2014.0965.

[129] M. M. Ertay, S. Tosun, and A. Zengin, "Simulated annealing based passive power filter design for a medium voltage power system," in *2012 International Symposium on Innovations in Intelligent Systems and Applications*, Jul. 2012. doi: 10.1109/INISTA.2012.6247042.

[130] N.-C. Yang and D. Mehmood, "Multi-Objective Bee Swarm Optimization Algorithm with Minimum Manhattan Distance for Passive Power Filter Optimization Problems," *Mathematics*, vol. 10, no. 1, Jan. 2022, doi: 10.3390/math10010133.

[131] R. Dehini and S. Sefiane, "POWER QUALITY AND COST IMPROVEMENT BY PASSIVE POWER FILTERS SYNTHESIS USING ANT COLONY ALGORITHM.," 2011.

[132] N. H. B. Abdul Kahar and A. F. Zobaa, "Application of mixed integer distributed ant colony optimization to the design of undamped single-tuned passive filters based harmonics mitigation," *Swarm Evol Comput*, vol. 44, Feb. 2019, doi: 10.1016/j.swevo.2018.03.004.

[133] R. Sirjani and M. Kusaf, "Optimal design of passive harmonic filters using Bee Colony Optimization," in *2016 HONET-ICT*, Oct. 2016. doi: 10.1109/HONET.2016.7753426.

[134] A. Rosyadi, O. Penangsang, and A. Soeprijanto, "Optimal filter placement and sizing in radial distribution system using whale optimization algorithm," in *2017 International Seminar on Intelligent Technology and Its Applications (ISITIA)*, Aug. 2017. doi: 10.1109/ISITIA.2017.8124060.

[135] G. Hachemi, H. Abdelkader, and D. Rachid, "Optimal Sizing of Passive Filters for Typical Industrial Power Systems," *Applied Mechanics and Materials*, vol. 905, Feb. 2022, doi: 10.4028/p-u37f6q.

[136] M. Mohammadi, "Bacterial foraging optimization and adaptive version for economically optimum sitting, sizing and harmonic tuning orders setting of LC harmonic passive power filters in radial distribution systems with linear and nonlinear loads," *Appl Soft Comput*, vol. 29, Apr. 2015, doi: 10.1016/j.asoc.2015.01.021.

[137] S. Tosun, "An approach for designing passive power filters for industrial power systems by using gravitational search algorithm," *Tehnicki vjesnik - Technical Gazette*, vol. 22, no. 2, 2015, doi: 10.17559/TV-20130822153221.

[138] W. Zhao, Z. Zhang, and L. Wang, "Manta ray foraging optimization: An effective bio-inspired optimizer for engineering applications," *Eng Appl Artif Intell*, vol. 87, Jan. 2020, doi: 10.1016/j.engappai.2019.103300.

[139] F. A. Alturki, H. O. Omotoso, A. A. Al-Shamma'a, H. M. H. Farh, and K. Alsharabi, "Novel Manta Rays Foraging Optimization Algorithm Based Optimal Control for Grid-Connected PV Energy System," *IEEE Access*, vol. 8, 2020, doi: 10.1109/ACCESS.2020.3030874.

[140] E. E. Elattar, A. M. Shaheen, A. M. El-Sayed, R. A. El-Sehiemy, and A. R. Ginidi, "Optimal Operation of Automated Distribution Networks Based-MRFO Algorithm," *IEEE Access*, vol. 9, 2021, doi: 10.1109/ACCESS.2021.3053479.
[141] A. Mohammadi-Balani, M. Dehghan Nayeri, A. Azar, and M. Taghizadeh-Yazdi, "Golden eagle optimizer: A nature-inspired metaheuristic algorithm," *Comput Ind Eng*, vol. 152, Feb. 2021, doi: 10.1016/j.cie.2020.107050.
[142] D. Połap and M. Woźniak, "Red fox optimization algorithm," *Expert Syst Appl*, vol. 166, Mar. 2021, doi: 10.1016/j.eswa.2020.114107.
[143] M. S. Braik, "Chameleon Swarm Algorithm: A bio-inspired optimizer for solving engineering design problems," *Expert Syst Appl*, vol. 174, Jul. 2021, doi: 10.1016/j.eswa.2021.114685.
[144] E. F. Fuchs and M. A. S. Masoum, "Power System Modeling under Nonsinusoidal Operating Conditions," in *Power Quality in Power Systems and Electrical Machines*, Elsevier, 2008. doi: 10.1016/B978-012369536-9.50008-5.
[145] A. Chidurala, T. Kumar Saha, and N. Mithulananthan, "Harmonic impact of high penetration photovoltaic system on unbalanced distribution networks – learning from an urban photovoltaic network," *IET Renewable Power Generation*, vol. 10, no. 4, Apr. 2016, doi: 10.1049/iet-rpg.2015.0188.
[146] T. A. H. Alghamdi and F. J. Anayi, "Modelling and Control Development of an MVDC Converter Implemented for Albaha Power Network," in *2021 5th International Conference on Power and Energy Engineering (ICPEE)*, Dec. 2021. doi: 10.1109/ICPEE54380.2021.9662568.
[147] J. H. R. Enslin and P. J. M. Heskes, "Harmonic Interaction Between a Large Number of Distributed Power Inverters and the Distribution Network," *IEEE Trans Power Electron*, vol. 19, no. 6, Nov. 2004, doi: 10.1109/TPEL.2004.836615.
[148] Chih-Ju Chou, Chih-Wen Liu, June-Yown Lee, and Kune-Da Lee, "Optimal planning of large passive-harmonic-filters set at high voltage level," *IEEE Transactions on Power Systems*, vol. 15, no. 1, 2000, doi: 10.1109/59.852156.
[149] T. Green, J. Barria, A. J. Ferre, Y. Pipelzadeh, M. Merlin, and N. Bottrell, "Electrical models of new network technologies and devices including power electronics and supporting ICT infrastructures," *The Institution of Engineering and Technology*, 2015.
[150] J. Mazumdar, R. G. Harley, F. C. Lambert, G. K. Venayagamoorthy, and M. L. Page, "Intelligent Tool for Determining the True HarmonicCurrent Contribution of a Customer in a Power Distribution Network," *IEEE Trans Ind Appl*, vol. 44, no. 5, Sep. 2008, doi: 10.1109/TIA.2008.2002213.
[151] K. G. Khajeh, D. Solatialkaran, F. Zare, and N. Mithulananthan, "Harmonic Analysis of Multi-Parallel Grid- Connected Inverters in Distribution Networks: Emission and Immunity Issues in the Frequency Range of 0-150 kHz," *IEEE Access*, vol. 8, 2020, doi: 10.1109/ACCESS.2020.2982190.

[152] R. Langella, A. Testa, J. Meyer, F. Moller, R. Stiegler, and S. Z. Djokic, "Experimental-Based Evaluation of PV Inverter Harmonic and Interharmonic Distortion Due to Different Operating Conditions," *IEEE Trans Instrum Meas*, vol. 65, no. 10, Oct. 2016, doi: 10.1109/TIM.2016.2554378.
[153] R. N. Beres, X. Wang, M. Liserre, F. Blaabjerg, and C. L. Bak, "A Review of Passive Power Filters for Three-Phase Grid-Connected Voltage-Source Converters," *IEEE J Emerg Sel Top Power Electron*, vol. 4, no. 1, Mar. 2016, doi: 10.1109/JESTPE.2015.2507203.
[154] C. Larose, R. Gagnon, P. Prud'Homme, M. Fecteau, and M. Asmine, "Type-III Wind Power Plant Harmonic Emissions: Field Measurements and Aggregation Guidelines for Adequate Representation of Harmonics," *IEEE Trans Sustain Energy*, vol. 4, no. 3, Jul. 2013, doi: 10.1109/TSTE.2013.2252209.
[155] J. C. Hernández, M. J. Ortega, and A. Medina, "Statistical characterisation of harmonic current emission for large photovoltaic plants," *International Transactions on Electrical Energy Systems*, vol. 24, no. 8, pp. 1134–1150, Aug. 2014, doi: 10.1002/etep.1767.
[156] D. Gallo *et al.*, "Case studies on large PV plants: Harmonic distortion, unbalance and their effects," in *2013 IEEE Power & Energy Society General Meeting*, 2013, pp. 1–5. doi: 10.1109/PESMG.2013.6672271.
[157] B. Adineh, M. R. Habibi, A. N. Akpolat, and F. Blaabjerg, "Sensorless Voltage Estimation for Total Harmonic Distortion Calculation Using Artificial Neural Networks in Microgrids," *IEEE Transactions on Circuits and Systems II: Express Briefs*, vol. 68, no. 7, pp. 2583–2587, Jul. 2021, doi: 10.1109/TCSII.2021.3059410.
[158] Wilsun Xu and Yilu Liu, "A method for determining customer and utility harmonic contributions at the point of common coupling," *IEEE Transactions on Power Delivery*, vol. 15, no. 2, Apr. 2000, doi: 10.1109/61.853023.
[159] W.-M. Lin, T.-S. Zhan, and M.-T. Tsay, "Multiple-Frequency Three-Phase Load Flow for Harmonic Analysis," *IEEE Transactions on Power Systems*, vol. 19, no. 2, May 2004, doi: 10.1109/TPWRS.2004.825906.
[160] R. A. S. Fernandes, M. Oleskovicz, and I. N. da Silva, "Harmonic Source Location and Identification in Radial Distribution Feeders: An Approach Based on Particle Swarm Optimization Algorithm," *IEEE Trans Industr Inform*, vol. 18, no. 5, pp. 3171–3179, May 2022, doi: 10.1109/TII.2021.3108681.
[161] C. Li, W. Xu, and T. Tayjasanant, "A 'Critical Impedance'-Based Method for Identifying Harmonic Sources," *IEEE Transactions on Power Delivery*, vol. 19, no. 2, Apr. 2004, doi: 10.1109/TPWRD.2004.825302.
[162] F.-J. Ruiz-Rodriguez, J.-C. Hernandez, and F. Jurado, "Harmonic modelling of PV systems for probabilistic harmonic load flow studies," *International Journal of Circuit Theory and Applications*, vol. 43, no. 11, pp. 1541–1565, Nov. 2015, doi: 10.1002/cta.2021.
[163] F. J. Ruiz-Rodriguez, J. C. Hernandez, and F. Jurado, "Iterative harmonic load flow by using the point-estimate method and complex affine arithmetic for radial distribution systems with photovoltaic uncertainties,"

International Journal of Electrical Power & Energy Systems, vol. 118, p. 105765, Jun. 2020, doi: 10.1016/j.ijepes.2019.105765.
[164] J. C. Hernandez, F. J. Ruiz-Rodriguez, F. Jurado, and F. Sanchez-Sutil, "Tracing harmonic distortion and voltage unbalance in secondary radial distribution networks with photovoltaic uncertainties by an iterative multiphase harmonic load flow," *Electric Power Systems Research*, vol. 185, p. 106342, Aug. 2020, doi: 10.1016/j.epsr.2020.106342.
[165] A. F. Zobaa, "Voltage Harmonic Reduction for Randomly Time-Varying Source Characteristics and Voltage Harmonics," *IEEE Transactions on Power Delivery*, vol. 21, no. 2, Apr. 2006, doi: 10.1109/TPWRD.2005.864043.
[166] R. Cisneros-Magaña, A. Medina-Rios, C. R. Fuerte-Esquivel, and J. Segundo-Ramírez, "Harmonic state estimation based on discrete exponential expansion, singular value decomposition and a variable measurement model," *Energy*, vol. 249, p. 123712, Jun. 2022, doi: 10.1016/j.energy.2022.123712.
[167] R. J. Betancourt, E. Barocio, C. M. Rergis, J. M. González-López, and A. C. Sánchez, "A spatio-temporal processing Padé approach for visualizing harmonic distortion propagation on electrical networks," *Electric Power Systems Research*, vol. 203, p. 107643, Feb. 2022, doi: 10.1016/j.epsr.2021.107643.
[168] J. Liang, S. Zhang, Y. Ren, and Y. Cheng, "Harmonics Current Detection in Three-phase Circuit using Neural Network," *J Phys Conf Ser*, vol. 2242, no. 1, p. 012043, Apr. 2022, doi: 10.1088/1742-6596/2242/1/012043.
[169] T. G. Manjunath, A. C. Vikramathithan, and H. Girish, "Analysis of Total Harmonic Distortion and implementation of Inverter Fault Diagnosis using Artificial Neural Network," *J Phys Conf Ser*, vol. 2161, no. 1, p. 012060, Jan. 2022, doi: 10.1088/1742-6596/2161/1/012060.
[170] J. Zhao and B. K. Bose, "Neural-Network-Based Waveform Processing and Delayless Filtering in Power Electronics and AC Drives," *IEEE Transactions on Industrial Electronics*, vol. 51, no. 5, Oct. 2004, doi: 10.1109/TIE.2004.834949.
[171] J. Choudhary, D. K. Singh, S. N. Verma, and K. Ahmad, "Artificial Intelligence Based Control of a Shunt Active Power Filter," *Procedia Comput Sci*, vol. 92, 2016, doi: 10.1016/j.procs.2016.07.356.
[172] M. Iqbal *et al.*, "Neural Networks Based Shunt Hybrid Active Power Filter for Harmonic Elimination," *IEEE Access*, vol. 9, 2021, doi: 10.1109/ACCESS.2021.3077065.
[173] L. L. Lai, W. L. Chan, C. T. Tse, and A. T. P. So, "Real-time frequency and harmonic evaluation using artificial neural networks," *IEEE Transactions on Power Delivery*, vol. 14, no. 1, 1999, doi: 10.1109/61.736681.
[174] H. C. Lin, "Intelligent Neural Network-Based Fast Power System Harmonic Detection," *IEEE Transactions on Industrial Electronics*, vol. 54, no. 1, Feb. 2007, doi: 10.1109/TIE.2006.888685.
[175] J. Mazumdar and R. G. Harley, "Recurrent Neural Networks Trained With Backpropagation Through Time Algorithm to Estimate Nonlinear Load

Harmonic Currents," *IEEE Transactions on Industrial Electronics*, vol. 55, no. 9, Sep. 2008, doi: 10.1109/TIE.2008.925315.
[176] J. Mazumdar and R. G. Harley, "Utilization of Echo State Networks for Differentiating Source and Nonlinear Load Harmonics in the Utility Network," *IEEE Trans Power Electron*, vol. 23, no. 6, Nov. 2008, doi: 10.1109/TPEL.2008.2005097.
[177] C. F. Nascimento, A. A. Oliveira, A. Goedtel, and A. B. Dietrich, "Harmonic distortion monitoring for nonlinear loads using neural-network-method," *Appl Soft Comput*, vol. 13, no. 1, Jan. 2013, doi: 10.1016/j.asoc.2012.08.043.
[178] A. Y. Hatata and M. Eladawy, "Prediction of the true harmonic current contribution of nonlinear loads using NARX neural network," *Alexandria Engineering Journal*, vol. 57, no. 3, Sep. 2018, doi: 10.1016/j.aej.2017.03.050.
[179] S. K. Jain and S. N. Singh, "Fast Harmonic Estimation of Stationary and Time-Varying Signals Using EA-AWNN," *IEEE Trans Instrum Meas*, vol. 62, no. 2, Feb. 2013, doi: 10.1109/TIM.2012.2217637.
[180] M. Žnidarec, Z. Klaić, D. Šljivac, and B. Dumnić, "Harmonic Distortion Prediction Model of a Grid-Tie Photovoltaic Inverter Using an Artificial Neural Network," *Energies (Basel)*, vol. 12, no. 5, Feb. 2019, doi: 10.3390/en12050790.
[181] K. Warwick, A. Ekwue, and R. Aggarwal, Eds., *Artificial Intelligence Techniques in Power Systems*. The Institution of Engineering and Technology, Michael Faraday House, Six Hills Way, Stevenage SG1 2AY, UK: IET, 1997. doi: 10.1049/PBPO022E.
[182] D. Hunter, H. Yu, I. M. S. Pukish, J. Kolbusz, and B. M. Wilamowski, "Selection of Proper Neural Network Sizes and Architectures—A Comparative Study," *IEEE Trans Industr Inform*, vol. 8, no. 2, May 2012, doi: 10.1109/TII.2012.2187914.
[183] C.-H. Lin and C.-H. Wang, "Adaptive Wavelet Networks for Power-Quality Detection and Discrimination in a Power System," *IEEE Transactions on Power Delivery*, vol. 21, no. 3, pp. 1106–1113, Jul. 2006, doi: 10.1109/TPWRD.2006.874105.
[184] K. P. Schneider *et al.*, "Analytic Considerations and Design Basis for the IEEE Distribution Test Feeders," *IEEE Transactions on Power Systems*, vol. 33, no. 3, pp. 3181–3188, May 2018, doi: 10.1109/TPWRS.2017.2760011.

Appendices

Appendix 1

Collected Data of the Albaha Power System

Overhead Lines Data

Voltage Level	***From***	***To***	***Line Parameters***		
			Resistance (p.u.)	***Reactance (p.u.)***	***Susceptance (p.u.)***
132 kV	*BN132*	*BE132*	*0.013*	*0.040*	*0.009*
	BN132	*BE132*	*0.013*	*0.040*	*0.009*
	BN132	*BT132*	*0.017*	*0.070*	*0.014*
	BN132	*BT132*	*0.017*	*0.070*	*0.014*
33 kV	*ATWLA*	*BN33*	*0.200*	*0.408*	-
	ATWLA	*BN33*	*0.200*	*0.408*	-
	SAQRA	*BN33*	*0.204*	*0.438*	-
	SAQRA	*BN33*	*0.204*	*0.244*	-
	SAQRA	*MNDQ*	*0.230*	*0.236*	-
	JDLAN	*ATWLA*	*0.100*	*0.020*	-
	ATWLA	*NEMA*	*0.100*	*0.200*	-
	NEMA	*MNDQ*	*0.300*	*0.640*	-
	BAH-UNI	*BE33*	*0.247*	*0.457*	-
	BE33	*BAH-UNI*	*0.247*	*0.457*	-
	BE33	*AIR-PRT*	*0.310*	*0.430*	-
	BAH-UNI	*AIR-PRT*	*0.120*	*0.235*	-
	TEQ-CLG	*BE33*	*0.056*	*0.120*	-
	SPRT-CTY	*BE33*	*0.037*	*0.080*	-
	BT33	*ZFIR*	*0.230*	*0.500*	-
	BT33	*ZFIR*	*0.230*	*0.500*	-
13.8 kV	*BN13.8*	*K.F.HOS*	*0.200*	*0.410*	-
	BN13.8	*K.F.HOS*	*0.200*	*0.410*	-
	BALAL	*BN13.8*	*0.240*	*0.360*	-
	SHBRQ	*BN13.8*	*0.300*	*0.500*	-

Loads Data

Voltage Level	*Name*	*Real Power (MW)*	*Reactive Power (MVAr)*
33 kV	*SAQRA*	*13.53*	*8.380*
	ATWLA	*12.51*	*7.760*
	JDLAN	*6.400*	*3.970*
	NEMA	*5.930*	*3.680*
	MNDQ	*13.79*	*8.550*
	SPRT-CTY	*18.00*	*14.00*
	TEQ-CLG	*3.000*	*3.000*
	BAH-UNI	*Look at Table 6*	*Look at Table 6*
	AIR-PRT	*Look at Table 6*	*Look at Table 6*
	ZFIR	*11.52*	*7.340*
13.8 kV	*W3-13*	*1.000*	*0.500*
	MOSA	*9.300*	*2.700*
	RAHWA	*2.390*	*2.190*
	BANSR	*4.700*	*0.025*
	MSRK	*3.100*	*0.020*
	MSQR	*2.700*	*0.050*
	ATHM	*1.900*	*0.080*
	K.F.HOS	*3.000*	*1.200*
	BALAL	*5.200*	*2.100*
	SHBRQ	*3.400*	*3.500*
	F3-F4	*3.630*	*4.660*
	F6-F7	*5.660*	*3.270*
	F1-F13	*46.81*	*27.79*

Power Transformers Data

From	*To*	*Quantity*	*Voltage (kV)*	*Rating (MVA)*	*Impedance (%)*	*X/R ratio*
BT132	*BT33*	*2*	*132/33*	*50*	*16*	*30*
BT132	*BT13.8*	*2*	*132/13.8*	*100*	*12*	*55*
BT33	*BT13.8*	*2*	*33/13.8*	*15*	*10*	*13*
BN132	*BN33*	*2*	*132/33*	*50*	*16*	*30*
BN132	*BN13.8*	*3*	*132/13.8*	*30*	*17*	*25*
BE132	*BE33*	*2*	*132/33*	*50*	*16*	*30*
BE132	*BE13.8*	*2*	*132/13.8*	*30*	*17*	*45*

Appendix 2

Simulated System Specifications for the ANN-based Harmonic Distortions Estimator.

Power Grid Specifications		
	Parameter	***Value***
Power Grid	*Voltage (Vg)*	*13.8 kV*
	Configuration	*Three-phase*
	Fundamental Frequency	*60 Hz*
	Impedance (Zg)	*5+ j12 mΩ*
Background Harmonics	*5^{th} harmonic voltage*	*0.01 p.u.*
	7^{th} harmonic voltage	*0.005p.u.*
PFC Capacitor	*Size*	*4 MVAr*
Per Unit Bases	*Base MVA*	*100 MVA*
	Base Voltage	*13.8 kV*

Solar PV-1 Specifications		
Three-phase Power Inverter with an MPPT Algorithm	*Rated Power*	*0.25 MW*
	Topology	*Two-level VSC*
	Filter Configuration	*L-type filter*
	Switching Frequency	*1.26 kHz*
	DC Voltage	*650 V*
Transformer	*Voltage*	*0.4/13.8 kV*
	Connection	*Δ/ Y*
	Leakage Reactance	*0.06 p.u.*

Solar PV-2 Specifications		
Three-phase Power Inverter with an MPPT Algorithm	*Rated Power*	*0.5 MW*
	Topology	*Three-level NPC*
	Filter Configuration	*L-type filter*
	Switching Frequency	*1.62 kHz*
	DC Voltage	*650 V*
Transformer	*Voltage*	*0.4/13.8 kV*
	Connection	*Yg/ Y*
	Leakage Reactance	*0.03 p.u.*

Wind Turbine Specifications		
Wind Turbine	*Structure*	*DFIG*
	Rated Wind Speed	*14 m/s*
Three-phase Power Inverter with an MPPT Algorithm	*Rated Power*	*0.5 MW*
	Topology	*Three-level NPC*
	Filter Configuration	*L-type filter*
	Switching Frequency	*1.26 kHz*
	DC Link Voltage	*1200 V*
Transformer	*Voltage*	*0.69/13.8 kV*
	Connection	*Yg/ Y*
	Leakage Reactance	*0.08 p.u.*

Nonlinear Load Specifications		
DC Load	*Max. Power*	*1 MW*
Three-phase Power Converter	*Topology*	*Two-level VSC*
Linear Load Specifications		
AC Load	*Load Type*	*Industrial*
	Operating Voltage	*13.8 kV*
	Active Power	*3 MW*
	Reactive Power	*2 MVAr*
	Power Factor	*0.83 lagging*

IEEE 34 with Solar PV-2 Specifications		
Per Unit Bases	*Base MVA*	*100 MVA*
	Base Voltage	*24.9 kV*
Interfacing Transformer	*Voltage*	*0.4/24.9 kV*
	Connection	*Yg/Yg*
	Leakage Reactance	*0.04 p.u.*

Appendix 3

Scripts used in this work.

```
----------------- Simple Harmonic Analysis Example ----------------------
% Simple Harmonic Analysis Example (Analytical)

clear all
clc
format long

% Define system components
ZTrh='0.2i*h’;
ZLh='0.1i*h';
BL1h='0.01i*h';
BL2h='0.01i*h';

% Define the current harmonic current source
H=[5;7;11;13;17;19;...
    23;25;29;31;35;...
    37;41;43;47;49];
Ic=[1/5;1/7;1/11;1/13;1/17;1/19;...
    1/23;1/25;1/29;1/31;1/35;...
    1/37;1/41;1/43;1/47;1/49];

for n=1:16,1;
   h= H(n);
   Yh=[0,0;0,0];

   % Form system admittance
   Yh(1,1)=-(1/eval(ZTrh)+1/eval(ZLh)+eval(BL1h));
   Yh(1,2)=1/eval(ZLh);
   Yh(2,1)=Yh(1,2);
   Yh(2,2)=-(1/eval(ZLh)+eval(BL2h));

   % Calculate harmonic impedance matrix
   Zh= Yh^(-1);

   % Calculate harmonic voltage distortions
   V1h(n)= abs(Zh(2,1)*Ic(n));
   V2h(n)= abs(Zh(2,2)*Ic(n));
end;

Dh=0.5;
for n=1:100,1;
   Z11(n)=abs(Zh(2,1));
   Z12(n)=abs(Zh(2,2));

end;

-------------------------------------------------------------------------------
```

```
---------- Harmonic Models Analysis ----------------------
clear all
clc
format long

% Overhead lines models (Analytical)
        z_h = (sqrt(h)*R_l) + (h*X_l*1i);

% Transformers models (Analytical)
switch model
    case 1
        tan_phi = exp(0.69+(0.79*log(Sr))-
(0.04*(log(Sr))^2));
        Rs = X_t/tan_phi;
        Rp = 10*X_t*tan_phi;
        z_t = (Rs + ((h^2)*(X_t^2)*Rp)/((Rp^2) +
(h^2)*(X_t^2))) + ...
            (+1i)*((h*X_t*(Rp^2))/((Rp^2)+((h^2)*(X_t)^2)));
    case 2
        A = 0.1;
        B = 1.5;
        Rs = R_t*(1+(A*(h^B)));
        z_t = Rs + (1i)*h*X_t;
    case 3
        if Sr < 100
            a0 = 0.875;
            a1 = 0.065;
            a2 = 1-a1-a0;
        else
            a0 = 0.775;
            a1 = 0.115;
            a2 = 1-a1-a0;
        end
        b = 1.15;
        Rs = R_t*(a0 + a1*(h^b) + a2*(h^2));
        z_t = Rs + (1i)*(h*X_t);
    case 4
        A = 0.1;
        B = 1.5;
        Rs = R_t*(1+(A*(h^B)));
        z_t = sqrt(h)*Rs + (1i)*(h*X_t);
    case 5
        ;
    otherwise
        z_t = R_t + (1i)*h*X_t;
end

% Linear Loads models (Analytical)

S_base =100;
Zb = V^2/S_base;
    R_load = V^2/P;
    X_load = V^2/Q;
    z_load = R*(1i)*h*X_load/(R+(1i)*h*X_load);
```

```
------------------------------ MRFO Algorithm for PPF -------------------------

% Manta Ray Foraging Optimization Algorithm for PPF

clc;
clear;
MaxIteration=1000;
PopSize=1000;
[BestX,BestF,HisBestF]=MRFO(FunIndex,MaxIteration,PopSize);

% Boundary limits
function  X=SpaceBound(X,Up,Low)
    Dim=length(X);
    S=(X>Up)+(X<Low);
    X=(rand(1,Dim).*(Up-Low)+Low).*S+X.*(~S);
end

% MRFO modelling
function [BestX,BestF,HisBestFit]=MRFO(F_index,MaxIt,nPop)
          [Low,Up,Dim]=FunRange(F_index);

    for i=1:nPop
        PopPos(i,:)=rand(1,Dim).*(Up-Low)+Low;
        PopFit(i)=BenFunctions(PopPos(i,:),F_index,Dim);
    end
       BestF=inf;
       BestX=[];

    for i=1:nPop
        if PopFit(i)<=BestF
           BestF=PopFit(i);
           BestX=PopPos(i,:);
        end
    end

       HisBestFit=zeros(MaxIt,1);


for It=1:MaxIt
     Coef=It/MaxIt;

       if rand<0.5
          r1=rand;
          Beta=2*exp(r1*((MaxIt-
It+1)/MaxIt))*(sin(2*pi*r1));
          if  Coef>rand
              newPopPos(1,:)=BestX+rand(1,Dim).*(BestX-
PopPos(1,:))+Beta*(BestX-PopPos(1,:));
          else
              IndivRand=rand(1,Dim).*(Up-Low)+Low;

newPopPos(1,:)=IndivRand+rand(1,Dim).*(IndivRand-
PopPos(1,:))+Beta*(IndivRand-PopPos(1,:));
          end
```

```
       else
            Alpha=2*rand(1,Dim).*(-log(rand(1,Dim))).^0.5;
            newPopPos(1,:)=PopPos(1,:)+rand(1,Dim).*(BestX-
PopPos(1,:))+Alpha.*(BestX-PopPos(1,:));
       end

    for i=2:nPop
        if rand<0.5
           r1=rand;
           Beta=2*exp(r1*((MaxIt-
It+1)/MaxIt))*(sin(2*pi*r1));
            if  Coef>rand

newPopPos(i,:)=BestX+rand(1,Dim).*(PopPos(i-1,:)-
PopPos(i,:))+Beta*(BestX-PopPos(i,:));
            else
                IndivRand=rand(1,Dim).*(Up-Low)+Low;

newPopPos(i,:)=IndivRand+rand(1,Dim).*(PopPos(i-1,:)-
PopPos(i,:))+Beta*(IndivRand-PopPos(i,:));
            end
        else
            Alpha=2*rand(1,Dim).*(-log(rand(1,Dim))).^0.5;

newPopPos(i,:)=PopPos(i,:)+rand(1,Dim).*(PopPos(i-1,:)-
PopPos(i,:))+Alpha.*(BestX-PopPos(i,:));
       end
    end

          for i=1:nPop

newPopPos(i,:)=SpaceBound(newPopPos(i,:),Up,Low);

newPopFit(i)=BenFunctions(newPopPos(i,:),F_index,Dim);
              if newPopFit(i)<PopFit(i)
                 PopFit(i)=newPopFit(i);
                 PopPos(i,:)=newPopPos(i,:);
              end
          end

            S=2;
        for i=1:nPop
            newPopPos(i,:)=PopPos(i,:)+S*(rand*BestX-
rand*PopPos(i,:));
        end

     for i=1:nPop
         newPopPos(i,:)=SpaceBound(newPopPos(i,:),Up,Low);

newPopFit(i)=BenFunctions(newPopPos(i,:),F_index,Dim);
         if newPopFit(i)<PopFit(i)
            PopFit(i)=newPopFit(i);
            PopPos(i,:)=newPopPos(i,:);
         end
```

```
     end

     for i=1:nPop
        if PopFit(i)<BestF
           BestF=PopFit(i);
           BestX=PopPos(i,:);
        end
     end


     HisBestFit(It)=BestF;
end


% PPF problem modelling
format long
load(Harmonics_DATA.mat')

for h=1:100,1;
    ZLoad(h)=R_Load+(h*X_Load);
    Zf(h)=(((Rf)^-1+((h*X_Lf)^-1))^-1)+(X_Cf/h);
    ZL(h)=R_L+(h*(X_L));
    Zp(h)=(((1/ZLoad(h))+(1/Zf(h)))^-1);
    Ztot(h)=((1/ZLoad(h))+(1/Zf(h)))^-1;

    if h==1;
        I_L=(Vg)/(ZL(h)+Zp(h));
        Vr1=Vg-(I_L*(ZL(h)));
        Vr2=Zp(h)*Ih(h)*((ZL(h))/(Zp(h)+ZL(h)));
        Vr(h)=abs(Vr1+Vr2);
    else
        Vr(h)=abs(Zp(h)*Ih(h)*((ZL(h))/(Zp(h)+ZL(h))));
    end
    end
%Objective functions
V_THD=100*(sqrt(sum(Vr(1,2:end).^2)))/(Vr(1))

%Penalties for unpractical solutions
if (Vr(1)>((1.05+X)*Vg) || Vr(1)<((0.95+X)*Vg))

    P1=5000;

else

    P1=0;

end

 if (cos(angle(Zp(1)))>(1+Y) || cos(angle(Zp(1)))<(0.9+Y))

     P2=5000;

   else
```

```
     P2=0;

 end

y= V_THD+P1+P2;

end
```

---------- Monte Carlo Simulation (MCS) method ----------

```
% Monte Carlo Simulation (MCS) method
sizeOfTheNormVec = input('What is the number of samples in
the normal distribution: ');
R_mean = input('Please provide the mean of the resistance in
Ohm: ');
R_std = input('Please provide the standard deviation of the
resistance in Ohm: ');
L_mean = input('Please provide the mean of the inductance in
H: ');
L_std = input('Please provide the standard deviation of the
inductance in H: ');

%% DEFINITION OF THE NORMAL DISTRIBUTION OF R AND L

% Defining the column vector of 50 steps
h = linspace(1, 50, 50)';
R = R_std.*randn(sizeOfTheNormVec,1) + R_mean;
L = L_std.*randn(sizeOfTheNormVec,1) + L_mean;

%% CALCULATING AND PLOTTING THE MAGNITUDE OF THE IMPEDANCE,
Z

for a = 1:length(R)              %Iterating over the length
of the R vector
    for b = 1:length(L)          %Iterating over the length
of the L vector
        z = (R(a)*sqrt(h)) + (j*(2*pi*60)*h*L(b));
        plot(h, abs(z))
        hold on
    end
end
hold off
grid on
xlabel('h')
ylabel('|Z|, Ohm')
title('Plot of the magnitude of Z against h for different
values of R and L')
```

The end.